


Ultimate Rayleigh-Bénard turbulence

Detlef Lohse 

Physics of Fluids Department, J. M. Burgers Center for Fluid Dynamics and Max Planck Center Twente for Complex Fluid Dynamics, Faculty of Science and Technology, University of Twente, P.O. Box 217, 7500 AE Enschede, Netherlands and Max-Planck Institute for Dynamics and Self-Organization, Am Fassberg 17, 37077 Göttingen, Germany

Olga Shishkina 

Max-Planck Institute for Dynamics and Self-Organization, Am Fassberg 17, 37077 Göttingen, Germany

 (published 6 August 2024)

Thermally driven turbulent flows are omnipresent in nature and technology. A good understanding of the physical principles governing such flows is key for numerous problems in oceanography, climatology, geophysics, and astrophysics for problems involving energy conversion, heating and cooling of buildings and rooms, and process technology. In the physics community, the most popular system to study wall-bounded thermally driven turbulence has been Rayleigh-Bénard flow, i.e., the flow in a box heated from below and cooled from above. The dimensionless control parameters are the Rayleigh number Ra (the dimensionless heating strength), the Prandtl number Pr (the ratio of kinematic viscosity to thermal diffusivity), and the aspect ratio Γ of the container. The key response parameters are the Nusselt number Nu (the dimensionless heat flux from the bottom to the top) and the Reynolds number Re (the dimensionless strength of the turbulent flow). While there is good agreement and understanding of the dependences $Nu(Ra, Pr, \Gamma)$ up to $Ra \sim 10^{11}$ (the “classical regime”), for even larger Ra in the so-called ultimate regime of Rayleigh-Bénard convection the experimental results and their interpretations are more diverse. The transition of the flow to this ultimate regime, which is characterized by strongly enhanced heat transfer, is due to the transition of laminar-type flow in the boundary layers to turbulent-type flow. Understanding this transition is of the utmost importance for extrapolating the heat transfer to large or strongly thermally driven systems. Here the theoretical results on this transition to the ultimate regime are reviewed and an attempt is made to reconcile the various experimental and numerical results. The transition toward the ultimate regime is interpreted as a non-normal–nonlinear and thus subcritical transition. Experimental and numerical strategies are suggested that can help to further illuminate the transition to the ultimate regime and the ultimate regime itself, for which a modified model for the scaling laws in its various subregimes is proposed. Similar transitions in related wall-bounded turbulent flows such as turbulent convection with centrifugal buoyancy and Taylor-Couette turbulence are also discussed.

DOI: [10.1103/RevModPhys.96.035001](https://doi.org/10.1103/RevModPhys.96.035001)

CONTENTS

I. Introduction	2	IV. Upper Bounds for the Heat Transport in the Rayleigh-Bénard System	12
II. Governing Equations and Control and Response Parameters	7	A. Analytical upper bounds for the general case of finite Prandtl number and no-slip boundary conditions	12
A. Oberbeck-Boussinesq approximation and dimensionless control parameters	7	1. The relation $Nu \leq Pr Re_z$	12
B. Exact analytical relations for the total heat transport and viscous and thermal dissipation rates	8	2. The relation $Nu \lesssim Pr^{1/2} Re_\tau$	13
C. Wind of turbulence and the Reynolds number	8	3. The relation $Nu \lesssim Ra^{1/2}$	13
III. Classical Regime	9	B. Analytical upper bounds for infinite or very large Prandtl numbers	15
A. The unifying theory of Grossmann and Lohse for the classical regime	9	1. Case of $Pr = \infty$	15
B. Description of experimental and numerical data by the Grossmann-Lohse theory in the classical regime	10	2. Case of $Pr \gtrsim Ra^\xi$, $\xi \geq 1/3$	16
C. From laminar Prandtl-Blasius to turbulent Prandtl-von Kármán boundary layers: The transition from the classical to the ultimate regime	11	C. Analytical upper bounds for other cases	16
		D. Optimal wall-to-wall steady-state heat transport	16
		V. Theoretical Models for the Heat Transport at Large Rayleigh Numbers: A Historical Perspective	17
		A. Priestley (1954) model	18
		B. Spiegel (1971) model	18
		C. Herring, Stewartson, and Roberts (1966) model	18

D. Malkus (1954) model	19
E. Kraichnan (1962) model	19
1. Large Prandtl number case	19
2. Small Prandtl numbers and large Rayleigh numbers	20
3. Moderate Prandtl numbers and large Rayleigh numbers	20
F. Castaing <i>et al.</i> (1989) model and Shraiman and Siggia (1990) model	20
G. Chavanne <i>et al.</i> (1997) model	21
H. Grossmann and Lohse (2011) model	22
I. Proposed model for the ultimate regime	22
1. Turbulent flow along a plate	22
2. Prandtl number dependence of the ultimate regime	23
J. Comparison of the models	25
VI. Rayleigh-Bénard Convection under Realistic Conditions	25
A. The influence of the container's aspect ratio	26
B. From the idealized fluid to real fluids: Non-Oberbeck-Boussinesq effects	27
C. From the idealized container to real containers: Small roughness and finite conductivity of the plates and sidewalls of the container	30
D. Instrumentation in the container	31
VII. Large Rayleigh Number Experiments	31
A. Chicago group	31
B. Grenoble group	31
C. Oregon, Trieste, and Brno groups	33
D. Göttingen: Large Ra experiments with pressurized SF ₆	34
E. Lyon and Tokyo groups: Large Ra experiments with liquid mercury	35
F. Reconciling the experimental findings: Non-normal–nonlinear transition	35
G. Which experiments can verify and illuminate the subcritical nature of the transition to the ultimate regime?	38
VIII. Large Rayleigh Number Numerics	39
A. 3D Rayleigh-Bénard flow simulations in the classical regime	39
B. Basic resolution and convergence requirements for a direct numerical simulation	40
C. 2D Rayleigh-Bénard flow simulations at large Ra	42
D. Can numerical simulations verify and illuminate the subcritical nature of the transition to the ultimate regime?	43
IX. Ultimate Turbulence in Related Systems	43
A. Turbulent convection with centrifugal buoyancy	43
B. Ultimate Taylor-Couette turbulence	45
C. Rayleigh-Bénard turbulence with pronounced plate roughness	47
D. Homogeneous Rayleigh-Bénard convection	48
E. Other convective systems	49
X. Conclusions and Outlook	49
Acknowledgments	51
References	51

I. INTRODUCTION

In 1904, a new era in modern fluid dynamics began with Prandtl's seminal insight that viscous boundary layers are key for the drag of any object in a flow, which overcame the deadlock of the potential flow theory of the 19th century. The

example that Prandtl (1905) used was the flow along a flat plate. By coupling the viscous flow within the boundary layer at the plate with the potential flow outside, he was able to calculate the drag coefficient of the plate as a function of the Reynolds number. In so doing he developed what is now known as Prandtl-Blasius boundary-layer theory (Schlichting, 1979). It is applicable to laminar boundary layers. As Prandtl realized and explained in his seminal work, physically the coupling to the outer potential flow is through detachment of vortical structures from the boundary layers, implying momentum exchange and thus friction. Prandtl (1905) also gave the scaling of the thickness λ_u of the kinetic boundary layer, namely, $\lambda_u/L \sim \text{Re}^{-1/2}$, where L is the typical length scale of the problem and Re is the Reynolds number. Prandtl's doctoral student Blasius (1908) was able to calculate the full velocity profile at the plate. Later the Prandtl-Blasius boundary-layer (BL) theory was extended to include thermal effects (Pohlhausen, 1921); this extension often goes by the name Prandtl-Blasius-Pohlhausen theory (Schlichting, 1979). It also gives the temperature profile over a hot plate with laminar flow along it (assuming that the temperature is a passive scalar) and, in particular, the thermal boundary-layer thickness λ_θ and its dependence on Re and the Prandtl number Pr , namely, $\lambda_\theta/L \sim \text{Re}^{-1/2}\text{Pr}^{-1/2}$ for small $\text{Pr} < 1$ when the kinetic BL is nested in the thermal one, and $\lambda_\theta/L \sim \text{Re}^{-1/2}\text{Pr}^{-1/3}$ for a large $\text{Pr} > 1$ when the thermal BL is nested in the kinetic one.

It was also Prandtl (1925) and, independently, von Kármán (1923) who realized that for strong enough driving (i.e., a large enough Re) at some point the laminar boundary layer becomes unstable and turbulent. This turbulent BL with its typical logarithmic profile for the mean velocity is now known as the turbulent Prandtl–von Kármán boundary layer; a logarithmic profile then also applies to the mean temperature profile, again with a Pr dependence (Schlichting, 1979).

But when (i.e., at what Reynolds number and under what conditions?) does the transition from a laminar BL to a turbulent one occur? Almost the same time as Prandtl started the boundary-layer research, Orr (1907) and, independently, Sommerfeld (1909) derived an equation that describes the linear evolution of a normal mode flow disturbance in a wall-parallel viscous flow. This equation can be applied to different wall-bounded flows. It was also studied in Prandtl's group with the hope of finding a critical Reynolds number for the transition from a laminar to a turbulent boundary layer. Tollmien (1929), another of Prandtl's doctoral students, took the boundary-layer velocity profile [which had been calculated by Blasius (1908)] as an unperturbed flow, solved the Orr-Sommerfeld equation as an eigenvalue problem, and evaluated the neutral linear stability curve that separates the regions of linear stability and instability of a perturbation mode. Based on these calculations, Tollmien (1929) found that the Prandtl-Blasius laminar boundary layer can become linearly unstable with a single normal mode perturbation at a shear Reynolds number (based on the displacement thickness of the laminar boundary layer) of about $\text{Re}_s \approx 420$ ($\text{Re}_s \sim \text{Re}^{1/2}$ as $\lambda_u/L \sim \text{Re}^{-1/2}$). The value of $\text{Re}_s \approx 420$ as a typical estimate for the instability in shear flows was popularized by Landau and Lifshitz (1987).

Attempts to find critical Reynolds numbers for the onset of the instability in different shear flows by applying the same method, however, fail in the sense that the theoretical results usually do not match the measurements that normally find transition to turbulence at significantly smaller Reynolds numbers than predicted by the eigenvalue analysis. Some flows, like Poiseuille flow, are linearly stable at any Re , yet become turbulent for large enough driving. The reasons for the early transition to turbulence were unclear for a long time.

The nature of this transition was understood only much later, at the end of the 20th century (Boberg and Brosa, 1988; Farrell, 1988; Farrell and Ioannou, 1993; Reddy and Henningson, 1993; Reddy, Schmid, and Henningson, 1993; Trefethen *et al.*, 1993). For shear flows, the Orr-Sommerfeld operator of the linearized system is non-normal, implying that its eigenvectors are nonorthogonal. The consequence thereof is that, even if all eigenvalues are negative, distortions of the linearized system can transiently grow. In the linearized and linearly stable case such distortions ultimately exponentially decay, but, in the nonlinear case and when the transient growth is strong enough, nonlinearity can set in and prevent the decay of the distortions. It is thus the interplay between non-normality and the nonlinearity that leads to the subcritical instability of the shear flow (Boberg and Brosa, 1988; Farrell, 1988; Farrell and Ioannou, 1993; Reddy, Schmid, and Henningson, 1993; Trefethen *et al.*, 1993). The eigenvalues of the Orr-Sommerfeld operator are highly sensitive to perturbations, and their sensitivity increases dramatically with the Reynolds number; for a high Re the eigenfunctions become almost colinear (Boberg and Brosa, 1988; Reddy, Schmid, and Henningson, 1993; Gebhardt and Grossmann, 1994; Grossmann, 2000). Correspondingly, this type of transition is now called a non-normal–nonlinear transition to turbulence. It is characterized by the so-called double-threshold behavior: Both the strength of the initial distortion and the Reynolds number must be large enough for this transition to happen: Small initial distortions require a larger Reynolds number for this instability to set in than large initial distortions. The most famous example of this type of transition may be the study of the transition of Reynolds (1883) from laminar to turbulent flow in a pipe. Though pipe flow is linearly stable at any Reynolds number, Reynolds (1883) found the transition at a Reynolds number of around 1300. In contrast, 100 years later, in 1983, Johannesen and Lowe, in the same lab in Manchester and with the same setup, already found an onset of turbulence at Reynolds numbers between 700 and 800. The reason for this difference lies in the double-threshold behavior: In the 100 years from 1883 to 1983, the noise to which the pipe flow was subjected had considerably increased, with the appearance of cars, trucks, and trains passing by the lab building, so that in 1983 much smaller Reynolds numbers were sufficient to trigger the transition to turbulence. The physics and mathematics of the non-normal–nonlinear transition in pipe flow was reviewed by Eckhardt *et al.* (2007), Barkley (2016), and Manneville (2016) and, most recently, by Avila, Barkley, and Hof (2023). Further excellent reviews on the non-normal–nonlinear transition in various shear flows were given by Grossmann (2000), Schmid and Henningson (2001), Kerswell (2002), Schmid (2007), and

Wu (2019). The characteristics of this transition are its subcritical and hysteretic nature and that it has a double-threshold behavior with no sharp onset, sensitivity to noise, poor reproducibility in experiments, and dependence on the initial conditions.

Why do we start this review on turbulent Rayleigh-Bénard convection with the Prandtl-Blasius and Prandtl–von Kármán boundary-layer theories and the non-normal–nonlinear transition to turbulence in shear flow? The answer is that they are key to understanding ultimate Rayleigh-Bénard turbulence, the subject of this review.

Rayleigh-Bénard convection is the flow in a closed box that is homogeneously heated from below and cooled from above; see Fig. 1. It is driven by the density differences between the lighter (usually) hot fluid, which wants to rise, and the heavier (usually) cold fluid, which wants to sink. The strength of the thermal driving is characterized by Ra , which is the non-dimensionalized temperature difference between the warm bottom and the cold top plate. The most relevant question in Rayleigh-Bénard convection is: How does the heat transport (in dimensionless form, Nu) depend on the control parameters, particularly the thermal driving strength Ra , but also on Pr (the ratio of kinematic viscosity and thermal diffusivity) and the aspect ratio Γ (width divided by height) of the container? And how does the strength of the flow inside the container, as expressed by Re of the developing large-scale wind, depend on Ra and Pr ?

We note that the Rayleigh-Bénard model applies not only to heat transfer but also to mass transfer provided that it is driven

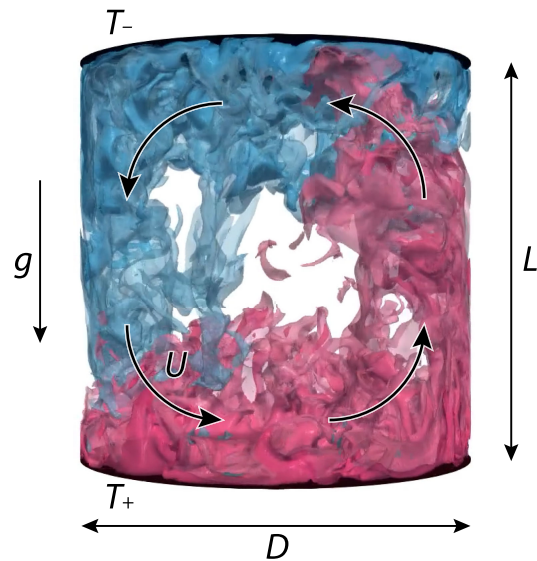


FIG. 1. The most standard geometry of a Rayleigh-Bénard convection setup: a cylindrical container, heated from below with a temperature T_+ and cooled from above with a temperature T_- , with a temperature difference $\Delta = T_+ - T_-$. The height of the cylinder is L and its diameter D . Buoyancy is upward against the gravitational acceleration g , and hot fluid (red, rising) moves upward and cold fluid (blue, descending) downward. Also shown is the developing large-scale “wind of turbulence” with a typical velocity U , which nondimensionally is expressed as $Re = UL/\nu$. The visualization is for $Ra = 10^9$, $Pr = 1$, and $\Gamma = D/L = 1$.

by density differences, for example, in a system with (heavy) salty water at the top and (lighter) fresh water at the bottom, as can occur in the ocean or the processing industry. For that case the corresponding Prandtl number (then called the Schmidt number $Sc = \nu/\mathcal{D}$, where \mathcal{D} is the mass diffusivity) is much larger than for thermal transport in gas or water, namely, $Sc \approx 700$, rather than $Pr \approx 0.7$ for gas under standard conditions or $4 \lesssim Pr \lesssim 10$ for water, depending on the temperature.

Rayleigh-Bénard (RB) convection has always been the most popular area for the development of new concepts in the physics of fluids, be it linear instabilities (Rayleigh, 1916; Jeffreys, 1928; Chandrasekhar, 1961; Busse, 1967; Drazin and Reid, 1981), nonlinear dynamics and chaos (Lorenz, 1963; Ahlers, 1974; Behringer, 1985; Strogatz, 1994), the emergence of spatiotemporal chaos and patterns (Cross and Hohenberg, 1993; Bodenschatz, Pesch, and Ahlers, 2000), where the systems has only a few degrees of freedom, or, when with increasing driving strength the system has gained many more degrees of freedom, classical Rayleigh-Bénard turbulence (Siggia, 1994; Kadanoff, 2001; Ahlers, Grossmann, and Lohse, 2009; Lohse and Xia, 2010; Chillà and Schumacher, 2012; Xia, 2013; Shishkina, 2021; Lohse and Shishkina, 2023), which is more precisely defined later. In this review, we employ the relatively new concept of the non-normal–nonlinear transition to turbulence to reconcile various experimental observations and theoretical concepts and models on the so-called ultimate Rayleigh-Bénard turbulence, for which the driving of the system is even stronger than for classical RB turbulence, i.e., Ra is even larger.

The ultimate RB regime is of particular interest for many geophysical and astrophysical applications, such as for thermally driven flow in the ocean, the atmosphere (Vallis, 2017), or the outer core of Earth, other planets, or stars, where naturally large Rayleigh numbers are achieved and where one wants to know the corresponding transport of heat (or mass). It is impossible to solve the governing equations analytically, and for this regime it is extremely difficult to study the flow in experiments and simulations. Therefore, to get an estimate for the transport at large Ra , one has to rely on extrapolations from lab experiments at a much smaller Ra (typically in the classical regime). Typically these extrapolations are scaling laws, but this makes sense only once there is no transition toward a different state of turbulence. If there is such a transition, the extrapolation with a simple scaling law becomes meaningless. But then, how can one upscale the RB system and understand and predict the heat and mass flux for a large Ra , as it occurs in geophysical and astrophysical applications? In this review we examine the present understanding of how to answer these questions.

Before we do so, we summarize the situation for Rayleigh numbers up to $Ra \sim 10^{11}$, which now is called the classical regime of RB turbulence (Sec. III); Sec. II contains the underlying dynamical equations and the control and response parameters. Meanwhile, in this classical regime there is good agreement between various experiments and numerical simulations and a good understanding of the flow physics [Grossmann-Lohse (GL) theory; see Grossmann and Lohse (2000, 2001, 2002), Ahlers, Grossmann, and Lohse (2009),

Stevens *et al.* (2013), and Lohse and Shishkina (2023)]. In a nutshell, GL theory makes use of two exact balance equations for the global energy dissipation rate and the global thermal dissipation rate, which follow from the underlying Boussinesq equations. As the local dissipation rates in the BLs and in the bulk reflect much different flow physics, the total dissipation rates are split into a BL part and a bulk part. In the BLs, for not too strong driving their scaling behavior directly follows from Prandtl-Blasius BL theory, whereas in the bulk with its fully developed turbulence the behavior follows from the Kolmogorov-Obukhov theory (Monin and Yaglom, 1975; Pope, 2000). With this, the GL theory gives the dependences $Nu(Ra, Pr)$ and $Re(Ra, Pr)$ (see Sec. III.A), thus describing the experimental and numerical data over at least 8 orders of magnitude in Ra and at least 6 orders of magnitude in Pr . In a sense, just as Prandtl (1905) coupled the laminar-type Prandtl-Blasius BLs to the outer potential Bernoulli flow in order to obtain the drag coefficient, for turbulent RB flow (or more generally for any wall-bounded turbulent flow) GL theory couples the Prandtl-Blasius BL to the turbulent, Kolmogorov-Obukhov-type bulk flow in order to obtain the Nusselt and Reynolds numbers.

But as explained, for large enough driving (i.e., a large enough Ra) the laminar-type Prandtl-Blasius BL must undergo a transition toward the turbulent-type Prandtl-von Kármán BL through the non-normal–nonlinear mechanism. GL theory even predicts in which Ra range this will happen, namely, when the shear Reynolds number Re_s becomes large enough, and as an indicative value it uses the Tollmien value $Re_s \approx 420$. This key idea of interpreting the transition to ultimate turbulence as a subcritical transition of non-normal–nonlinear type is discussed in Sec. III.C.

From the 1960s up to the 1980s, the fluid dynamics community was far from able to achieve the ultimate regime in any controlled experiments, not to mention any direct numerical simulations, which did not exist at the time. Therefore, one had to rely on theoretical models for the ultimate regime. The models must also obey the mathematically strict upper bounds for the heat transport, which follow from the underlying equations. We give these upper bounds in Sec. IV. In Sec. V we review the theoretical models with their strong points and shortcomings. In particular, we discuss the model assumptions, which often have not been spelled out explicitly. Section V also includes a comparison of the various models and a proposed modified model for the scaling laws in the various subregimes of the ultimate regime.

The modern era of highly turbulent RB convection research started in Chicago in the late 1980s and early 1990s. Albert Libchaber had the vision to employ cryogenic helium as a fluid since it has extremely low kinematic viscosity and thermal conductivity. With this, $Ra \sim 10^{14}$ could be achieved; see the influential paper by Castaing *et al.* (1989) and later work from the Chicago group for these high Ra results (Wu and Libchaber, 1991, 1992; Procaccia *et al.*, 1991). This line of research was continued in Grenoble, France, by Chavanne *et al.* (1997), who were the first to find a transition toward some type of steep effective scaling of Nu versus Ra , which was later confirmed and further analyzed by the Grenoble group (Chavanne *et al.*, 2001; Roche, Castaing, Chabaud, and

Hébral, 2001; Gauthier and Roche, 2008; Roche *et al.*, 2010; Roche, 2020). Roche (2020) also realized the subcritical nature of the transition to the ultimate regime; see Fig. 2 of his paper, in which he explicitly compared the transition toward the ultimate regime to the transition toward fully developed turbulence in pipe flow.

Russ Donnelly in Oregon took up Libchaber’s idea of employing cryogenic helium as a fluid but further enlarged the height of the RB container, achieving an even larger Ra of up to $\sim 10^{17}$ (Niemela, Skrbek, and Donnelly, 2000; Niemela, Skrbek, Sreenivasan, and Donnelly, 2000; Niemela, Skrbek, Swanson *et al.*, 2000; Niemela *et al.*, 2001; Niemela and Sreenivasan, 2003a). However, no transition to an ultimate regime with an enhanced effective Nu versus Ra scaling was identified in those experiments, nor was any transition identified in follow-up experiments partially carried out in Trieste, Italy, by members of that group (Niemela and Sreenivasan, 2006a, 2006b, 2008; Niemela, Babuin, and Sreenivasan, 2010), and partially in Brno, Czechia (Urban, Musilová, and Skrbek, 2011; Urban *et al.*, 2012, 2014, 2019; Skrbek and Urban, 2015). The increase in the Nu versus Ra relation observed in some of these experiments was interpreted as a non-Oberbeck-Boussinesq effect (i.e., as an effect of a strong variation of the fluid properties on temperature or pressure that is not represented within the standard Oberbeck-Boussinesq approximation).

Experiments with cryogenic helium have a complication in that, when Ra is increased over several orders of magnitude, in general Pr also increases, though in their helium experiments Roche *et al.* (2010) and Roche (2020) succeeded in keeping Pr constant for nearly 2 orders of

magnitude. In experiments with pressurized gas SF₆, the density ρ is large and, since $Ra \propto L^3/(\kappa\nu) \propto L^3\rho^2$, in large-scale containers it is possible to achieve a high Ra under almost Boussinesq conditions. Ahlers, Funfschilling, and Bodenschatz (2009), Ahlers *et al.* (2009), Ahlers, Bodenschatz *et al.* (2012), Ahlers, He *et al.* (2012), He, Funfschilling, Bodenschatz, and Ahlers (2012), He, Funfschilling, Nobach *et al.* (2012), Ahlers, Bodenschatz, and He (2014), He *et al.* (2014, 2015), and He, Bodenschatz, and Ahlers (2016, 2020) made use of this property and performed large Ra RB experiments with pressurized SF₆. They observed a transition to an ultimate RB regime, namely, at around $Ra \sim 10^{14}$ (with a slight dependence on the container aspect ratio), with a steeper Nu(Ra) dependence than in the classical regime, which can be described with an effective scaling law $Nu \sim Ra^{0.38}$.

The discrepancy between a typical Grenoble dataset, a typical Oregon dataset, and a typical Göttingen, Germany, dataset in the large Ra regime is illustrated in Fig. 2. More detailed data showing the differences between the various datasets are given in Fig. 3. Up to $Ra \sim 10^{11}$ the various datasets roughly agree, but they show the onset of the ultimate regime at different Ra.

What could be the origin of the differences in the various experiments? Any experiment has imperfections compared to the ideal case described in Sec. II: The underlying dynamical equations are not exactly of the Oberbeck-Boussinesq type, and the boundary conditions are not perfect. Indeed, as the results are discrepant, possible differences in the setups and in the material properties could be the origin and must be analyzed in detail. Thus, in Sec. VI we discuss

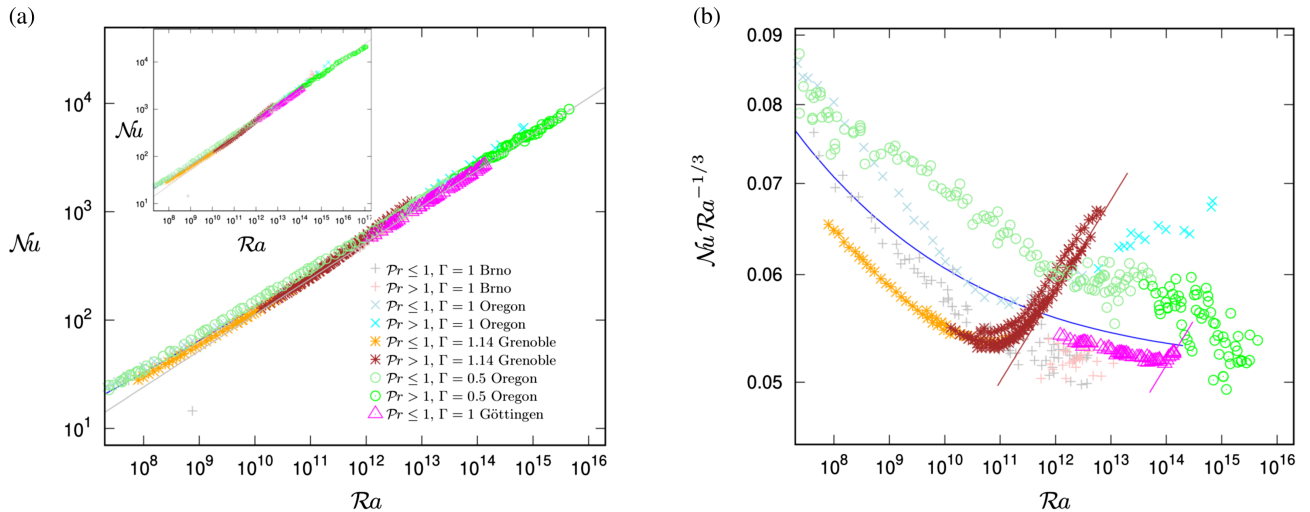


FIG. 2. Dependencies of (a) Nu and (b) compensated Nusselt number $NuRa^{-1/3}$ on Ra as measured in different Rayleigh-Bénard experiments in cylindrical containers with aspect ratios Γ close to 1 and 1/2. The blue curve shows the Grossmann-Lohse predictions for the classical regime: $Pr = 1$ and $\Gamma = 1$. The inset of (a) presents all available data, while (a) and (b) contain only those data that satisfy $\alpha\Delta < 15\%$ (one of the Oberbeck-Boussinesq requirements; see Sec. VI.B). Prandtl numbers are almost constant in the Grenoble and Göttingen experiments; in these experiments the transition to the ultimate regime (given as $Nu \sim Ra^{0.4}$, indicated with the inclined straight brown and magenta lines, respectively) was precisely identified at the highest Rayleigh numbers achieved in these experiments. The following datasets are considered here: Grenoble (Roche *et al.*, 2010; Roche, 2020), Oregon (Niemela, Skrbek, and Donnelly, 2000; Niemela, Skrbek, Sreenivasan, and Donnelly, 2000; Niemela, Skrbek, Swanson *et al.*, 2000; Niemela and Sreenivasan, 2003a), Göttingen (He, Funfschilling, Bodenschatz, and Ahlers, 2012; He, Funfschilling, Nobach *et al.*, 2012), and Brno (Urban *et al.*, 2014, 2019).

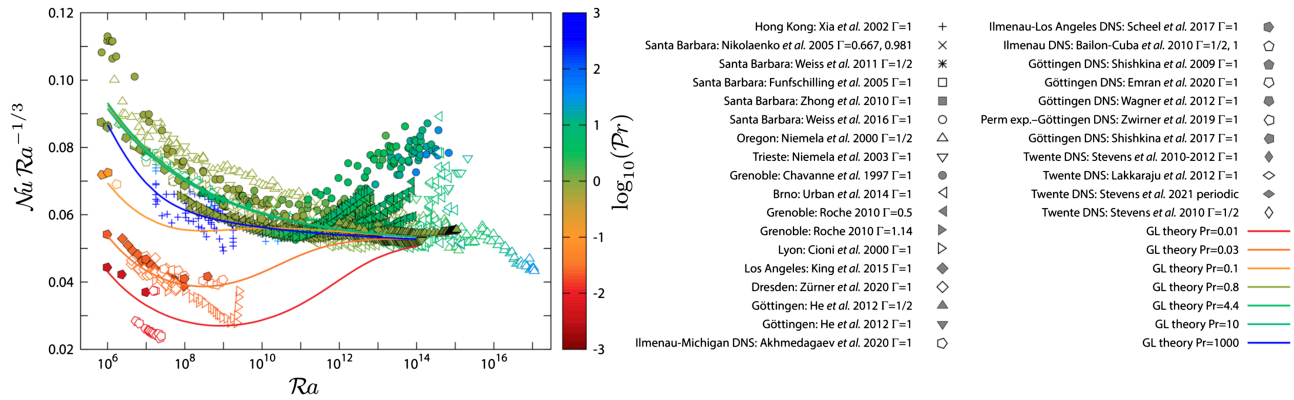


FIG. 3. Experimental and numerical data from various groups (see the legend) for the dependence of the heat transport (Nu) on the control parameters of the system, which are Ra and Pr . Shown is $Nu(Ra, Pr)$ compensated by $Ra^{1/3}$ vs Ra . The Pr dependence is visualized through the color code given on a logarithmic scale (see the legend); note that for some datasets Pr varies. The aspect ratio Γ ranges from $1/2$ to 1 (see the legend); in this aspect ratio range, the Γ dependence of Nu is weak. The solid lines are from GL theory for various Pr [from bottom to top: $Pr = 0.01$ (red line), 0.03 (orange line), 0.1 (yellow line), and 1000 (blue line) and $0.8 \leq Pr \leq 10$ (green, almost indistinguishable line)]. Adapted from Lohse and Shishkina, 2023.

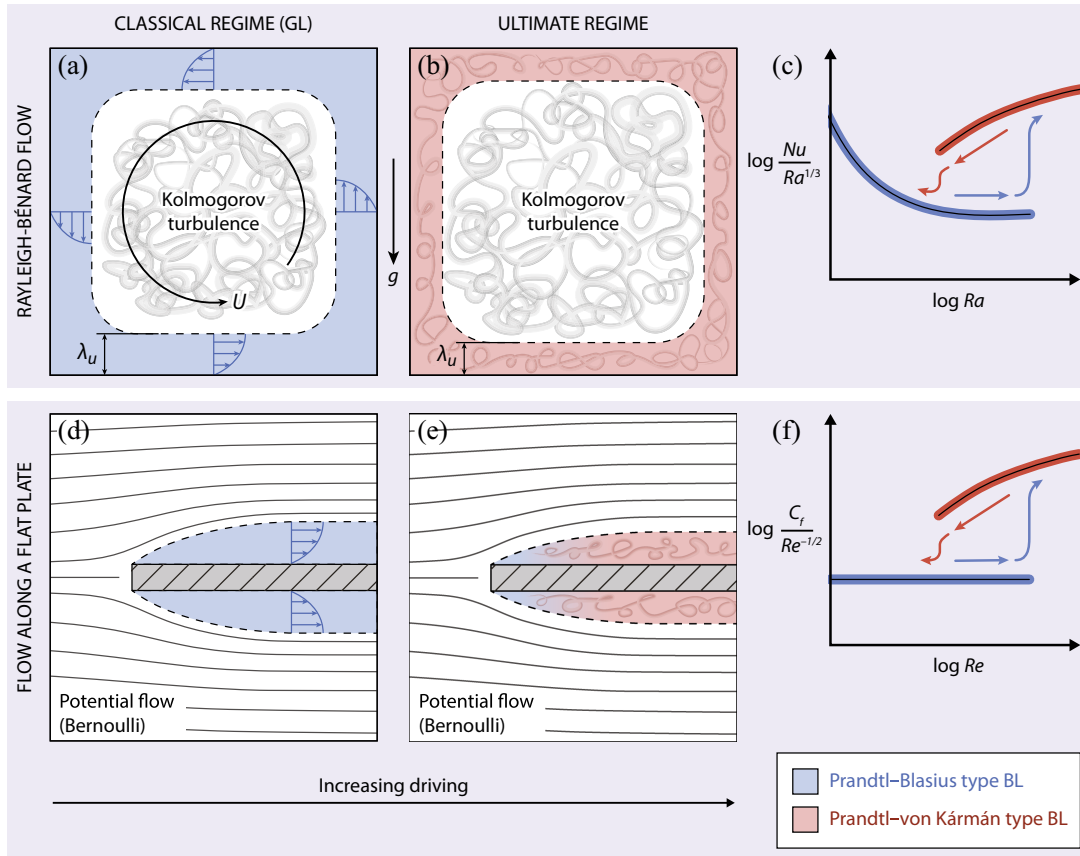


FIG. 4. Analogy between (a)–(c) Rayleigh-Bénard flow and (d)–(f) parallel flow along a flat plate. (a), (b) In turbulent Rayleigh-Bénard convection, the core part of the flow is always turbulent. With increasing thermal driving strength (i.e., increasing Ra), the kinetic boundary layers (BLs) change from a laminar Prandtl-Blasius-type boundary layer [(a), blue area] to a turbulent Prandtl-von Kármán-type boundary layer [(b), red area]. These two different cases correspond to two distinct dependences of the heat transport (Nu) vs the thermal driving strength (Ra) illustrated in (c) with the blue and red lines, respectively. Analogously to Rayleigh-Bénard flow, parallel flow (d)–(f) along a flat plate undergoes a transition between (d) laminar and (e) turbulent boundary layers that have different dependences of the skin friction coefficient C_f on Re , which are shown in (f) as blue and red lines, respectively. There is a similar analogy between Rayleigh-Bénard flow and Taylor-Couette flow [cf. Figs. 21(d)–21(f)], and also between RB flow and pipe and channel flows, which we discuss in Sec. IX. A comparison with the transition to turbulence in pipe flow was worked out by Roche (2020); see Fig. 2 of that paper. Adapted from Lohse and Shishkina, 2023.

large Ra RB convection under realistic conditions, namely, the lateral confinement of the flow, possible non-Oberbeck-Boussinesq effects and effects originating from nonideal plates and sidewalls, which are not described by the ideal boundary conditions in Sec. II. The large Ra experiments of Chicago, Grenoble, Oregon (and later Trieste and Brno), Göttingen, Lyon, and Tokyo (the last two for liquid mercury: $\text{Pr} \approx 0.02$) are described in Sec. VII, with focuses on possible differences and the dependences $\text{Nu}(\text{Ra}, \text{Pr}, \Gamma)$. At the end of Sec. VII we return to the ideas formulated in Sec. III.C and try to reconcile the various observations, realizing that they can simply be interpreted as a consequence of the non-normal–nonlinear nature of the transition to the ultimate regime (Roche, 2020; Lohse and Shishkina, 2023), as this transition is simply the transition between a laminar-type Prandtl–Blasius BL to a turbulent-type Prandtl–von Kármán BL.

In Sec. VIII, we discuss large Ra direct numerical simulations in both two and three dimensions. These simulations have the advantage that both the underlying equations and the boundary conditions are exactly known, but the disadvantage that the computational effort to reach the ultimate regime is enormous. In fact, in 3D simulations of RB convection, the ultimate regime has not yet been reached.

Sections VII and VIII both end with suggestions for future experiments and numerical simulations to confirm (or falsify) the hypothesis that the seemingly contradicting observations on the ultimate regime simply reflect the non-normal–nonlinear nature of the transition from a sheared laminar-type Prandtl–Blasius BL to a turbulent Prandtl–von Kármán BL.

Section IX discusses analogous transitions toward analogous ultimate regimes in various related systems, such as the Taylor–Couette system (Grossmann, Lohse, and Sun, 2016), where due to the much more efficient mechanical driving the transition toward the ultimate regime is much easier to achieve, a system with centrifugal buoyancy (Jiang *et al.*, 2020, 2022; Rouhi *et al.*, 2021; Wang *et al.*, 2022, 2023; Zhong, Wang, and Sun, 2023), and homogeneous RB convection. The review ends in Sec. X with conclusions and an outlook on the interesting and ever-changing times that lie ahead in the research on wall-bounded turbulence.

II. GOVERNING EQUATIONS AND CONTROL AND RESPONSE PARAMETERS

In this section we give the governing equations with their boundary conditions. They hold within the RB container, which for the cylindrical case is sketched in Fig. 1, where we also define the geometrical dimensional control parameters. In this section we also give the dimensionless control parameters of the system and its main response parameters and show how they are related by exact analytical relations that follow from the governing equations and their boundary conditions.

A. Oberbeck-Boussinesq approximation and dimensionless control parameters

The simplest approximation to describe thermally driven flows, with buoyancy taken into account, is the Oberbeck-Boussinesq (OB) approximation (Oberbeck, 1879;

Boussinesq, 1903). It assumes that the flow is incompressible and, moreover, that (i) all fluid properties are constant except the density in the buoyancy force term in the momentum equation, which is taken as linearly dependent on the temperature, and that (ii) the pressure work and the viscous dissipation terms in the heat equation are negligible. The governing equations for the velocity field $\mathbf{u}(\mathbf{x}, t)$ (with u_j the velocity components in spatial directions x_j), the temperature field $T(\mathbf{x}, t)$, and the hydrodynamic pressure $p(\mathbf{x}, t)$ in this OB approximation are then the continuity equation

$$\nabla \cdot \mathbf{u} = 0 \quad (1)$$

following from mass conservation for incompressible fluid, the momentum equation

$$\partial_t \mathbf{u} + (\mathbf{u} \cdot \nabla) \mathbf{u} + \nabla p / \rho = \nu \nabla^2 \mathbf{u} + \alpha(T - T_0) g \mathbf{e}_z \quad (2)$$

following from momentum conservation, and the heat equation

$$\partial_t T + (\mathbf{u} \cdot \nabla) T = \kappa \nabla^2 T \quad (3)$$

following from energy conservation (Landau and Lifshitz, 1987). In Eqs. (2) and (3) g is the acceleration due to gravity, ρ is the density at a reference temperature T_0 and pressure P_0 , $\nu \equiv \mu/\rho$ is the kinematic viscosity, and $\kappa \equiv k/(\rho c_p)$ is the thermal diffusivity, with μ the dynamic viscosity, k the thermal conductivity, and c_p the specific heat at constant pressure. Further notations here are ∂_t the partial derivative with respect to time t , and \mathbf{e}_z the unit vector pointing upward.

The system of the partial differential equations (1)–(3) needs to be supplemented by the boundary conditions for the velocity and temperature fields. These boundary conditions are no slip for the velocity ($\mathbf{u} = 0$) at all boundaries of the domain (i.e., at all walls of the container), adiabatic for the temperature at the sidewalls ($\partial T / \partial \mathbf{n} = 0$, where \mathbf{n} is the surface normal), and isothermal at the bottom ($T = T_+$) and top ($T = T_-$) plates, with the temperature difference $\Delta \equiv T_+ - T_-$ between the hot bottom plate and the cold top plate, which are separated by a distance L ; see Fig. 1.

Equations (1)–(3) can be made dimensionless in different ways. For example, taking as the reference quantities Δ for the temperature, L for the length, $u_{\text{ff}} \equiv \sqrt{\alpha g L \Delta}$ for the velocity (the so-called free-fall velocity), L/u_{ff} for the time, and ρu_{ff}^2 for the pressure, one obtains dimensionless governing equations that look similar to Eqs. (1)–(3) but with the following substitutions for the viscosity $\nu \rightarrow \sqrt{\text{Pr}/\text{Ra}}$, the thermal diffusivity $\kappa \rightarrow 1/\sqrt{\text{PrRa}}$, the pressure term $\nabla p / \rho \rightarrow \nabla p$, and the gravitational buoyancy term $\alpha(T - T_0)g \rightarrow T$. Thus, we obtain the dimensionless equations with two control parameters, which are the Rayleigh number

$$\text{Ra} \equiv \frac{\alpha g \Delta L^3}{\nu \kappa} \quad (4)$$

and the Prandtl number

$$\text{Pr} \equiv \nu / \kappa. \quad (5)$$

Regardless of the choice of reference quantity, these control parameters or their combinations always appear in the resulting dimensionless equations.

The aspect ratio Γ of the typical horizontal-to-vertical extensions of the domain is the third independent control parameter. For a cylinder, one lateral length scale suffices, i.e., the diameter D of the cylinder, thus implying an aspect ratio

$$\Gamma \equiv D/L. \quad (6)$$

If the two horizontal extensions of the domain differ, then one must consider the aspect ratios for each lateral direction. For a rectangular box, one then has two relevant aspect ratios $\Gamma_x \equiv D_x/L$ and $\Gamma_y \equiv D_y/L$, one for each lateral direction.

B. Exact analytical relations for the total heat transport and viscous and thermal dissipation rates

In the theories of heat transfer discussed later in the review, two exact analytical relations are key, namely, one for the mean kinetic energy dissipation rate ϵ_u following from the momentum equation, and one for the mean thermal dissipation rate ϵ_θ following from the heat transfer equation. We recall them here and also derive an exact relation for the total heat flux.

We now consider the OB governing equations for the velocity \mathbf{u} and the reduced temperature $\theta \equiv T - T_0$, which is defined with the mean temperature $T_0 \equiv (T_+ + T_-)/2$,

$$\partial_t \mathbf{u} + (\mathbf{u} \cdot \nabla) \mathbf{u} + \nabla p / \rho = \nu \nabla^2 \mathbf{u} + \alpha \theta \mathbf{g}_z, \quad (7)$$

$$\partial_t \theta + (\mathbf{u} \cdot \nabla) \theta = \kappa \nabla^2 \theta. \quad (8)$$

The boundary conditions are no slip for the velocity ($\mathbf{u} = 0$) at all boundaries, adiabatic for the temperature at the sidewalls ($\partial\theta/\partial\mathbf{n} = 0$), and isothermal at the bottom ($\theta = \Delta/2$) and top ($\theta = -\Delta/2$). Averaging the heat equation (8) in time $\langle \cdot \rangle_t$ and using the continuity equation $\nabla \cdot \mathbf{u} = 0$, one obtains that the local heat flux vector (nondimensionalized with $\kappa\Delta/L$)

$$\mathbf{F}(\mathbf{x}, t) \equiv \frac{\theta \mathbf{u}(\mathbf{x}, t) - \kappa \nabla \theta(\mathbf{x}, t)}{\kappa \Delta / L} \quad (9)$$

is divergence free if time averaged, that is,

$$\nabla \cdot \langle \mathbf{F} \rangle_t = 0. \quad (10)$$

Integrating Eq. (10) over the lower part of the container from the bottom to any height z ($z \in [0, L]$) and taking into account the adiabatic sidewall boundary conditions, one concludes that the vertical component of the heat flux F_z is constant if it is averaged in time and over any horizontal cross section S_z . This constant is the Nusselt number

$$\text{Nu} \equiv \langle F_z \rangle_{t, S_z}, \quad (11)$$

i.e., the dimensionless heat transfer, which is the first main response parameter of the system. Integration of Eq. (10) over all $z \in [0, L]$ with the respective top- and bottom-temperature

boundary conditions gives the following formula for the time- and volume-averaged convective heat flux $\langle u_z \theta \rangle$:

$$\text{Nu} - 1 = \frac{L}{\kappa \Delta} \langle u_z \theta \rangle. \quad (12)$$

With this, the mean (i.e., time- and volume-averaged) scalar product of the velocity field and the momentum equation $\langle \mathbf{u} \cdot \nabla p / \rho \rangle$ [Eq. (7)] leads to the following relation for the mean kinetic energy dissipation rate (i.e., the mean viscous dissipation rate) ϵ_u :

$$\epsilon_u \equiv \nu \langle (\nabla \mathbf{u})^2 \rangle = \alpha g \langle u_z \theta \rangle = \frac{\nu^3}{L^4} \text{RaPr}^{-2} (\text{Nu} - 1). \quad (13)$$

Equation (13) is the first desired relation.

Next the product of the temperature with the heat equation $\langle \theta \nabla^2 \theta \rangle$ [Eq. (8)] yields the relation for the mean thermal dissipation rate ϵ_θ ,

$$\epsilon_\theta \equiv \kappa \langle (\nabla \theta)^2 \rangle = \frac{\kappa \Delta^2}{L^2} \text{Nu}. \quad (14)$$

Equations (13) and (14) have been well known since at least the works of Malkus (1954) and Sorokin (1954); see also Spiegel (1971), Shraiman and Siggia (1990), and Siggia (1994). These integral relations are important since they are used as main constraints considered in the variational analysis to obtain the upper bounds to the heat transport in the turbulent regime (Howard, 1963, 1972; Busse, 1969; Doering and Constantin, 1996), and they serve as a starting point in GL theory (Grossmann and Lohse, 2000, 2001) for the classical regime in RB convection as well as in the models for the ultimate regime in turbulent RB convection (Kraichnan, 1962; Chavanne *et al.*, 1997; Grossmann and Lohse, 2011).

C. Wind of turbulence and the Reynolds number

Next to Nu, the second main response parameter of the system is Re, which is the nondimensionalized velocity U of the large-scale wind of turbulence $\text{Re} \equiv UL/\nu$. This is also called the wind Reynolds number. The central role of this wind of turbulence for the flow organization was first realized by Castaing *et al.* (1989) and later illustrated by Kadanoff (2001). We sketch this wind of turbulence in Fig. 1.

The key objective in the research on RB turbulence can thus be summarized as follows: Given the control parameters Ra, Pr, and Γ , how large are the response parameters

$$\text{Nu}(\text{Ra}, \text{Pr}, \Gamma), \quad \text{Re}(\text{Ra}, \text{Pr}, \Gamma)? \quad (15)$$

We note that there are various ways how to exactly define the Reynolds number or typical velocity in RB flow, for example, with the mean modulus of the velocity, with the mean upward velocity, or with the mean velocity at a fixed position in the flow, which usually scale in the same way. One can also define additional Reynolds numbers with the velocity *fluctuations* at various positions or averaged over the entire domain. These fluctuational velocities can scale differently than the wind velocities. These differences were discussed by

Grossmann and Lohse (2004) and later reviewed by Ahlers, Grossmann, and Lohse (2009) and thus are not the subject of this review.

III. CLASSICAL REGIME

In this section we discuss the classical regime of a Rayleigh-Bénard system with a Rayleigh number up to $Ra \sim 10^{11}$ (for $Pr \sim 1$ and smaller or larger Ra for smaller or larger Pr , respectively), where there is a good understanding of the flow physics.

A. The unifying theory of Grossmann and Lohse for the classical regime

The first key idea of the unifying theory for thermal convection proposed by Grossmann and Lohse (2000, 2001, 2002, 2004) was that for wall-bounded thermally driven turbulent flows there are always BLs and a bulk, and that the physics in the BLs and the bulk is different; cf. Fig. 5. In this sense the spirit of GL theory is the same as that of Prandtl's seminal paper (Prandtl, 1905) in which Prandtl realized the existence of a BL around an object in a flow and the implications thereof. Though Grossmann and Lohse originally suggested this theory for Rayleigh-Bénard convection, the idea of the theory could later be extended to various other wall-bounded thermally driven flows, such as horizontal convection, vertical convection, centrifugal buoyancy-driven

thermal convection and double-diffusive convection, and even mechanically driven wall-bounded turbulent flow like Taylor-Couette flow, pipe flow, or channel flow.

For the kinetic BL and later also for the thermal BL, Prandtl (1905), Blasius (1908), and Pohlhausen (1921) developed what is now called the Prandtl-Blasius-Pohlhausen BL theory, or Prandtl-Blasius BL theory (Schlichting, 1979; Landau and Lifshitz, 1987; Pope, 2000), which couples the BL flow to the potential flow around the object outside the BL. GL followed this idea but realized that, for turbulent flow outside the BL, potential flow is inappropriate and must be replaced by the Kolmogorov-Obukhov picture (Kolmogorov, 1941; Obukhov, 1959; Monin and Yaglom, 1975) of a turbulent cascade in the bulk of the flow. The key idea of GL theory is that the total kinetic energy dissipation rate ϵ_u (averaged over time and space) inside the confined flow is the sum of the kinetic energy dissipation rate in the BL (weighed with the relative BL thickness $2\lambda_u/L$) and in the bulk [weighed with the relative thickness of the bulk $(L - 2\lambda_u)/L$],

$$\epsilon_u = \epsilon_{u,BL} + \epsilon_{u,bulk}, \quad (16)$$

and a similar approach is taken for the thermal dissipation rate ϵ_θ (averaged over time and space),

$$\epsilon_\theta = \epsilon_{\theta,BL} + \epsilon_{\theta,bulk}. \quad (17)$$

The flow geometry in general terms is sketched in Figs. 5(a) and 5(b), with a typical kinetic BL thickness λ_u and a typical thermal BL thickness λ_θ , which can be either smaller (for large Pr) or larger (for small Pr) than λ_u , and with a large-scale velocity U characterizing the flow intensity of the bulk and an outer temperature scale Δ characterizing the strength of the thermal driving set by the temperature difference between the plates. Note again that the flow physics in the BL and in the bulk is different, which must be reflected by different scaling relations in these two domains. The kinetic BL exists both at the plates and at the sidewalls due to the no-slip boundary conditions, whereas the thermal BL exists only at the upper and lower plates.

For the BL thicknesses, GL assumed the Prandtl-Blasius scaling

$$\lambda_u/L \sim Re^{-1/2} \quad (18)$$

and

$$\lambda_\theta/L \sim Re^{-1/2} Pr^{-1/2} \quad \text{or} \quad \sim Re^{-1/2} Pr^{-1/3} \quad (19)$$

for small Pr or large Pr , respectively, depending on whether the kinetic BL is nested in the thermal one (small Pr), or vice versa (large Pr). This picture also includes that for small Reynolds numbers λ_u does not diverge but must be cut off by a length scale of the order of the height L of the container. The Prandtl-Blasius picture implies that

$$\epsilon_{u,BL} \sim \nu \frac{U^2 \lambda_u}{\lambda_u^2 L} \quad (20)$$

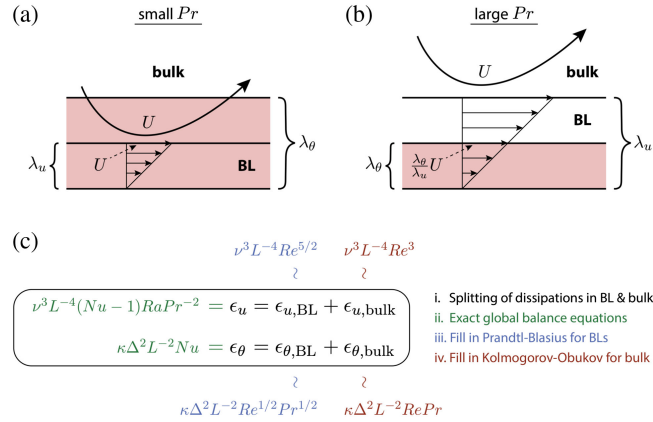


FIG. 5. Sketch of the first idea of GL theory for thermal convection: boundary-layer nesting for (a) small Pr where $\lambda_u < \lambda_\theta$ and the kinetic BL is nested in the thermal one and (b) large Pr where $\lambda_\theta < \lambda_u$ and the thermal BL is nested in the kinetic one. (a),(b) Adapted from Grossmann and Lohse, 2000. (c) GL theory, which consists of four steps: (i) The total energy dissipation rate and the total thermal dissipation rate are split into a BL part and a bulk part. (ii) The exact relations for the total energy dissipation rate and the total thermal dissipation rate, which directly follow from the underlying Boussinesq equations, are used. (iii) The Prandtl-Blasius BL theory is used to estimate the dissipation rates in the BLs. The Pr scaling of the thermal BL thickness depends on whether the thermal BL is nested in the kinetic one (for large Pr), or vice versa (for small Pr). For simplicity, we included the exponents only of the small Pr case, i.e., for $\lambda_u < \lambda_\theta$. (iv) The Kolmogorov-Obukhov theory is used to estimate the dissipation rates in the bulk.

and

$$\epsilon_{\theta, \text{BL}} \sim \kappa \frac{\Delta^2 \lambda_\theta}{\lambda_\theta^2 L}. \quad (21)$$

Note that for weak thermal driving of the flow (which will turn out to be over a considerable range) the Prandtl-Blasius-type scaling is unavoidable. For strong driving this type of scaling may break down because the BLs become turbulent, but the theory itself gives information on when this will happen, as it predicts the shear Reynolds number of the BL. Note also that GL theory does not claim Prandtl-Blasius profiles: it refers only to the scaling of the BL thicknesses.

For the bulk, GL assumed the Kolmogorov-Obukov picture of fully developed turbulence, implying that

$$\epsilon_{u, \text{bulk}} \sim U^3/L \quad (22)$$

and

$$\epsilon_{\theta, \text{bulk}} \sim U \Delta^2/L. \quad (23)$$

The second key ingredient of GL theory is to employ the previously derived exact global balance relations for the time- and space-averaged energy and thermal dissipation rates, Eqs. (13) and (14), respectively. Inserting Eqs. (16) and (17) with the four scaling relations (20)–(23) into the exact Eqs. (13) and (14) results in two implicit equations for Nu and Re as functions of Ra and Pr. Solving these implicit equations gives the desired relations Nu(Ra, Pr) and Re(Ra, Pr). The key ideas of GL theory are visually summarized in Fig. 5(c).

For completeness and self-containedness, we reproduce here the full GL equations from [Stevens *et al.* \(2013\)](#) or, identically, from the earlier papers by [Grossmann and Lohse \(2001\)](#) and [Ahlers, Grossmann, and Lohse \(2009\)](#), namely,

$$(\text{Nu} - 1)\text{RaPr}^{-2} = c_1 \frac{\text{Re}^2}{g(\sqrt{\text{Re}_L/\text{Re}})} + c_2 \text{Re}^3, \quad (24)$$

$$\begin{aligned} \text{Nu} - 1 &= c_3 \text{Re}^{1/2} \text{Pr}^{1/2} \left\{ f \left[\text{Nu} g \left(\sqrt{\frac{\text{Re}_L}{\text{Re}}} \right) \right] \right\}^{1/2} \\ &+ c_4 \text{Pr} \text{Re} f \left[\text{Nu} g \left(\sqrt{\frac{\text{Re}_L}{\text{Re}}} \right) \right]. \end{aligned} \quad (25)$$

The crossover functions f and g model the crossover from the thermal BL nested in the kinetic one toward the inverse situation and that for which $\lambda_u \sim L/\text{Re}^{1/2}$ extends to container half height $\sim L/2$ and cannot increase further with decreasing Re but must be replaced by $\lambda_u \sim L$ when Re reaches a smaller enough Reynolds number Re_L ; for further details, including the definitions of the crossover functions f and g , see [Grossmann and Lohse \(2001\)](#).

B. Description of experimental and numerical data by the Grossmann-Lohse theory in the classical regime

As described by [Grossmann and Lohse \(2000, 2001, 2002\)](#), [Ahlers, Grossmann, and Lohse \(2009\)](#), and [Stevens *et al.* \(2013\)](#), the four prefactors c_i , where $i = 1, 2, 3, 4$, and Re_L of

Eqs. (24) and (25) have to be determined from reliable experimental or numerical data, namely, from four values $\text{Nu}_i(\text{Ra}_i, \text{Pr}_i)$, where $i = 1, 2, 3, 4$, for the Nusselt number and one value for the Reynolds number at one data point $\text{Re}_5(\text{Ra}_5, \text{Pr}_5)$. Note that the four prefactors c_i , where $i = 1, 2, 3, 4$, correspond to the unknown prefactors in the four scaling relations (20)–(23). [Stevens *et al.* \(2013\)](#) picked five appropriate experimental data points $\text{Nu}_i(\text{Ra}_i, \text{Pr}_i)$, where $i = 1, 2, 3, 4$, and $\text{Re}_5(\text{Ra}_5, \text{Pr}_5)$ for experiments with an aspect ratio $\Gamma = 1$ and obtained the following five GL parameters: $c_1 = 8.05$, $c_2 = 1.38$, $c_3 = 0.487$, $c_4 = 0.0252$, and $a = 0.922$. For $\Gamma = 1/2$ they proceeded correspondingly. In principle, these prefactors depend on the aspect ratio Γ , as discussed by [Stevens *et al.* \(2013\)](#), reflecting that the geometric volume ratio between sidewall BLs, plate BLs, and bulk also depends on Γ . Whereas this dependence seems to be weak for $\Gamma \gtrsim 1/2$, for small Γ this will be no longer the case, as for small Γ the sidewalls stabilize the flow and the kinetic BL at the sidewall become more and more prominent with decreasing Γ . We discuss the dependence on Γ in more detail in Sec. VI.

The resulting full two-dimensional dependences Nu(Ra, Pr) and Re(Ra, Pr) are reproduced in Figs. 6(a) and 6(b), respectively (for $\Gamma = 1$). Both Nu and Re axes have been rescaled to allow for a proper visualization. Nu(Ra, Pr) does not follow one pure scaling law only, which would correspond to a straight plane in this visualization, but the dependences are more complicated since in different regions of the parameter space different terms dominated, as previously explained. The same holds for Re(Ra, Pr). We note that the shown region covers 8 orders of magnitude in Ra and 7 orders of magnitude in Pr. We also note that the theory has strong predictive power; the experimental input were only the five data points. Indeed, GL theory has facilitated various predictions of certain dependences Nu(Ra, Pr) and Re(Ra, Pr) in certain regimes of

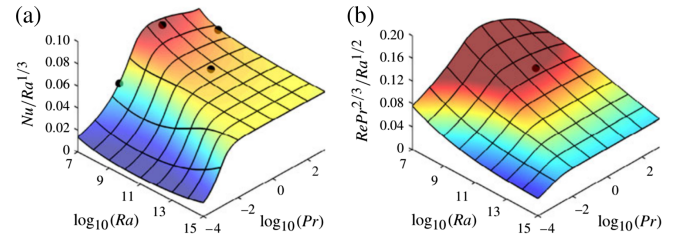


FIG. 6. Compensated 3D visualization of (a) Nu(Ra, Pr) and (b) Re(Ra, Pr) for $\Gamma = 1$. The four Nu(Ra, Pr) points and the Re(Ra, Pr) point, which are used to fit the parameters c_i , where $i = 1, 2, 3, 4$, and Re_L in GL theory for Rayleigh-Bénard convection, are indicated as black dots. The references in the legend refer to [Castaing *et al.* \(1989\)](#), [Chavanne *et al.* \(1997\)](#), [Cioni, Ciliberto, and Sommeria \(1997\)](#), [Glazier *et al.* \(1999\)](#), [Niemela, Skrbek, Sreenivasan, and Donnelly \(2000\)](#), [Ahlers and Xu *et al.* \(2001\)](#), [Chaumat, Castaing, and Chillà \(2002\)](#), [Fleischer and Goldstein \(2002\)](#), [Xia, Lam, and Zhou \(2002\)](#), [Niemela and Sreenivasan \(2003a\)](#), [Funfschilling *et al.* \(2005\)](#), [Sun and Zia \(2005\)](#), [Sun *et al.* \(2005\)](#), [Ahlers, Grossmann, and Lohse \(2009\)](#), [Burnishev, Segre, and Steinberg \(2010\)](#), [Roche *et al.* \(2010\)](#), [Stevens, Clercx, and Lohse \(2010b\)](#), [Stevens, Verzicco, and Lohse \(2010\)](#), [Urban, Musilová, Skrbek \(2011\)](#), [Emran and Schumacher \(2012\)](#), and [He, Funfschilling, Nobach *et al.*, 2012](#). Adapted from [Stevens *et al.*, 2013](#).

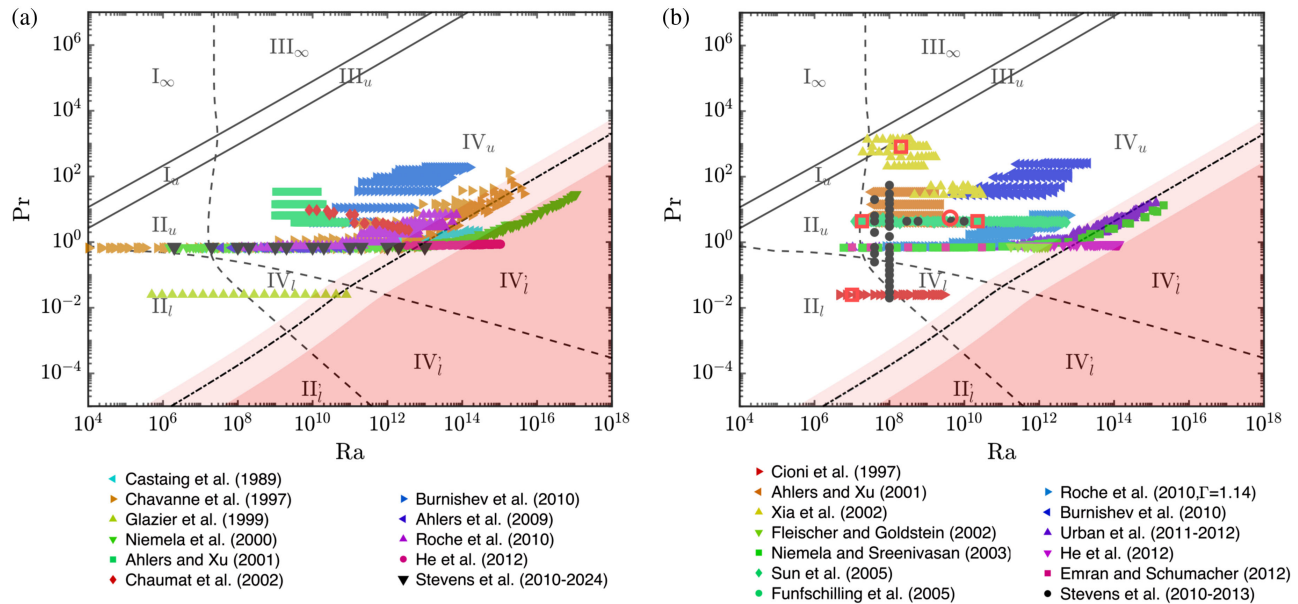


FIG. 7. Phase diagrams along the Ra - Pr plane for RB convection according to GL theory (Grossmann and Lohse, 2000, 2001, 2002, 2004) in (a) a $\Gamma = 0.5$ container and (b) a $\Gamma = 1$ container with no-slip boundary conditions. The upper solid line indicates that $Re = Re_L$, the lower, nearly parallel solid line corresponds to $\epsilon_{u,BL} = \epsilon_{u,bulk}$, the partially vertical dashed line corresponds to $\epsilon_{\theta,BL} = \epsilon_{\theta,bulk}$, and along the partially horizontal dashed line it is $\lambda_u = \lambda_\theta$. The light red region indicates where the laminar kinetic BL is expected to become turbulent (at the onset of the ultimate regime) based on a critical shear Reynolds number Re_s of the kinetic BL between $Re_s^* = 300$ (the left edge of the light red region) and $Re_s^* = 800$ (the right edge of the light red region). The Tollmien value $Re_s = 420$ is given as the dash-dotted line. In the darker red region $Re_s > 800$ one is even further into the ultimate regime. The four large red open squares indicate the locations of the four $Nu(Ra, Pr)$ points and the large red open circle represents the $Re(Ra, Pr)$ points that were used for the GL fit. Adapted from Stevens *et al.*, 2013.

parameter space, which are later confirmed by experiments or numerical simulations. Examples were given by Ahlers, Grossmann, and Lohse (2009) and Stevens *et al.* (2013), who also presented various cross sections of parameter space, including experimental and numerical data, namely, $Nu(Ra)$ for fixed Pr numbers, $Nu(Pr)$ for fixed Ra numbers, $Re(Ra)$ for fixed Pr numbers, and $Re(Pr)$ for fixed Ra numbers, which are all reasonably well described by the theory.

A complementary way to represent the results of GL theory is to display the phase diagram in Ra - Pr parameter space; see Fig. 7, which was adapted from Stevens *et al.* (2013). The lines are explained in the caption. The names of the regimes refer to the names used in the original papers (Grossmann and Lohse, 2000, 2001, 2002), i.e., IV_u means dominance of the bulk contributions in Eqs. (16) and (17) and $\lambda_\theta < \lambda_u$, etc. Figure 7 also contains various experimental and numerical data that were available to Stevens *et al.* (2013). Many more exist. To the left of the dash-dotted thick line (as explained in Sec. III.C), i.e., in the classical regime, all data are reasonably well described via the GL theory.

One may wonder why the GL theory is so successful and robust, although for RB turbulence in real containers the velocity and temperature profiles deviate from the Prandtl-Blasius predictions (van Reeuwijk, Jonker, and Hanjalić, 2008; Shishkina and Thess, 2009; Scheel, Kim, and White, 2012; Shi, Emran, and Schumacher, 2012), even when a local rescaling procedure is applied (Zhou and Xia, 2010; Zhou *et al.*, 2010, 2011; Stevens *et al.*, 2012) or the pressure gradient along the plate is taken into account (Shishkina, Horn, and Wagner, 2013; Shishkina, Wagner, and Horn, 2014). The answer is that GL

theory requires only that the scaling of the thicknesses of the boundary layers follows the Prandtl-Blasius-type scaling [Eqs. (18) and (19)], as previously stated. Indeed, from a closed set of BL equations for turbulent Rayleigh-Bénard convection (Shishkina *et al.*, 2015; Shishkina, Horn *et al.*, 2017; Ching *et al.*, 2019) that also takes the turbulent fluctuations within the BL equations into account, one can analytically derive the dependence of the heat flux (Nu) on the Reynolds and Prandtl numbers and two parameters that measure fluctuations. These theoretical results show that $Nu \propto Re^{1/2}Pr^{1/3}$ in the high- Pr limit and $Nu \propto Re^{1/2}Pr^{1/2}$ in the low- Pr limit, all subject to a weak dependence on the eddy viscosity (Tai *et al.*, 2021). This reveals a close resemblance of the scaling dependencies of the heat transport in steady forced convection (with Prandtl-Blasius-Pohlhausen BLs) and classical Rayleigh-Bénard convection. The BL theory for RB convection (Shishkina *et al.*, 2015; Ching *et al.*, 2019) can also predict the temperature profiles for large Pr (Shishkina *et al.*, 2015) and small Pr (Shishkina, Horn *et al.*, 2017) and can potentially also predict the velocity profiles provided that the full system of the fluctuating BL equations is considered (Ching, Dung, and Shishkina, 2017; Tai *et al.*, 2021).

C. From laminar Prandtl-Blasius to turbulent Prandtl-von Kármán boundary layers: The transition from the classical to the ultimate regime

As stated in the Introduction, for increasing driving strength the laminar-type Prandtl-Blasius BL at some point must break down and give rise to a turbulent-type Prandtl-von Kármán

BL. As an indication of when this would happen, Grossmann and Lohse (2000, 2001) assumed a transition shear Reynolds number of $Re_s \approx 420$ that was based on the value given by Tollmien (1929) and Landau and Lifshitz (1987). As the shear Reynolds number in the Prandtl-Blasius BL is related to the Reynolds number as $Re_s = aRe^{1/2}$ and GL theory predicts $Re(Ra, Pr)$, it thus also predicts when the laminar-type Prandtl-Blasius BL gives rise to a turbulent Prandtl-von Kármán BL, i.e., when the classical regime comes to an end and gives rise to the ultimate regime with enhanced heat transport. The line $Re_s = 420$ is shown as the dash-dotted line in the Ra - Pr parameter space in Fig. 7. To visualize that the transition is of subcritical, non-normal–nonlinear nature and can happen in a certain range and not at a fixed shear Reynolds number, we have shaded the entire range between $Re_s = 300$ and 800 in light red, whereas the range with $Re_s > 800$ is shaded in darker red.

It was Roche (2020) who first discussed the implications of the subcritical, non-normal–nonlinear nature of the transition from the classical regime to the ultimate regime of RB turbulence, and we recently elaborated on this (Lohse and Shishkina, 2023). As discussed in the Introduction, the characteristics of such a non-normal–nonlinear transition are that there is no sharp onset, that it is hysteretic, that multiple states are possible for the same control parameters, that it is sensitive to small distortions, and, connected to this, that it displays the so-called double-threshold behavior (Trefethen *et al.*, 1993), meaning that both the shear Reynolds number and the initial noise must be large enough for the transition to happen. It is typical for shear flows and cannot be predicted from the linear instability of single modes but emerges from the non-normal nature of the operator in the linearized Navier-Stokes equation. The non-normal operators have nonorthogonal eigenvectors allowing for transient growth of initial distortions; in fact, the stronger the distortions, the stronger the shear is (Boberg and Brosa, 1988; Gebhardt and Grossmann, 1994; Grossmann, 2000). For the linearized case the distortions would eventually decay in the linearly stable region, but for the full nonlinear equations for large enough transient growth nonlinearity will eventually take over and lead to an instability, in spite of the linear stability of the equations (Farrell, 1988; Farrell and Ioannou, 1993; Reddy and Henningson, 1993; Trefethen *et al.*, 1993; Schmid and Henningson, 2001; Kerswell, 2002; Eckhardt, Grossmann, and Lohse, 2007c; Schmid, 2007; Barkley, 2016; Manneville, 2016; Wu, 2019; Avila, Barkley, and Hof, 2023).

We emphasize that such a transition scenario is applicable for the transition from the classical regime to the ultimate regime in RB flow, as this is a transition of the laminar-type Prandtl-Blasius BL, which is a typical shear flow, at least locally at the plate or at the sidewalls. In contrast, the transition from the purely conductive state of RB flow to a convective state at $Ra \approx 1708$ (for a large aspect ratio $\Gamma \gg 1$ and for all Pr) is a linear instability.

As we see in Sec. VII.E, the features of the subcritical non-normal–nonlinear transition can reconcile the various experimental observations on the transition to the ultimate regime made in the past three decades. Further evidence to confirm (or falsify) the hypothesis that the transition from the classical regime to the ultimate regime is of a non-normal–nonlinear

nature will be welcome. At the end of Secs. VII and VIII we suggest experiments and numerical simulations that could provide clarity.

IV. UPPER BOUNDS FOR THE HEAT TRANSPORT IN THE RAYLEIGH-BÉNARD SYSTEM

When dealing with the ultimate regime, it is relevant to be aware of mathematically rigorous upper bounds for Nu in the large Ra limit. In this section we first give simple proofs that Nu in Rayleigh-Bénard convection asymptotically cannot grow faster than $Ra^{1/2}$, $Pr Re_z$, or $Pr^{1/2} Re_\tau$ (without focusing on the optimal prefactors). Here Re_z is the Reynolds number based on the mean vertical velocity $\langle u_z^2 \rangle^{1/2}$ and $Re_\tau \equiv u_\tau L/\nu$ is the shear Reynolds number, which is based on the friction velocity

$$u_\tau \equiv \sqrt{\tau_w/\rho}, \quad (26)$$

where τ_w is the mean wall shear stress. It is given by the vertical derivatives of the horizontal components of the velocity (u_x and u_y) at the plate ($z = 0$),

$$u_\tau^2 = \nu \langle (\partial_z u_x)^2 + (\partial_z u_y)^2 \rangle_{t,z|_{z=0}}. \quad (27)$$

Later in this section we review the best-known asymptotic upper bounds for the Nusselt number in Rayleigh-Bénard convection, sought as a power law of the Rayleigh number, when $Ra \rightarrow \infty$.

A. Analytical upper bounds for the general case of finite Prandtl number and no-slip boundary conditions

1. The relation $Nu \leq Pr Re_z$

Define the Reynolds number Re_z based on the mean vertical velocity as

$$Re_z \equiv \langle u_z^2 \rangle^{1/2} L/\nu. \quad (28)$$

The relation $Nu \lesssim Pr Re_z$ then follows immediately from the Cauchy-Schwarz inequality (12) and the standard assumption that the maximum principle on the temperature always holds,

$$|\theta| \leq \Delta. \quad (29)$$

Indeed,

$$Nu - 1 \leq \frac{L}{\kappa \Delta} \langle u_z^2 \rangle^{1/2} \langle \theta^2 \rangle^{1/2} \leq Pr Re_z. \quad (30)$$

Obviously, Re_z does not exceed Re ,

$$Re \equiv \langle \mathbf{u} \cdot \mathbf{u} \rangle^{1/2} L/\nu, \quad (31)$$

which is based on the total velocity, and therefore

$$Nu - 1 \leq Pr Re. \quad (32)$$

When combining Eqs. (13) and (30), we find that

$$\epsilon_u \leq \frac{\nu^3}{L^4} Re_z Re_{\text{ff}}^2 = \alpha \Delta g \langle u_z^2 \rangle^{1/2} = \frac{\nu^3}{L^4} \frac{Ra Re_z}{Pr}, \quad (33)$$

where the free-fall Reynolds number

$$\text{Re}_{\text{ff}} \equiv u_{\text{ff}}L/\nu = \sqrt{\text{Ra}/\text{Pr}} \quad (34)$$

is based on the free-fall velocity $u_{\text{ff}} \equiv \sqrt{\alpha\Delta gL}$.

2. The relation $\text{Nu} \lesssim \text{Pr}^{1/2}\text{Re}_\tau$

To derive this relation we need the following two direct consequences from the continuity equation (1): First,

$$\begin{aligned} (\nabla\mathbf{u})^2 &\equiv \sum_i (\nabla u_i)^2 \geq \sum_i (\partial_i u_i)^2 \\ &\geq (\partial_z u_z)^2 + \frac{1}{2}(\partial_x u_x + \partial_y u_y)^2 = \frac{3}{2}(\partial_z u_z)^2, \end{aligned} \quad (35)$$

which holds in the entire domain. Second,

$$\begin{aligned} (\nabla\mathbf{u})^2|_{z=0} &= \sum_i (\partial_z u_i)^2|_{z=0} \\ &= (\partial_z u_x)^2|_{z=0} + (\partial_z u_y)^2|_{z=0} \end{aligned} \quad (36)$$

(since $\partial_z u_z|_{z=0} = -\partial_x u_x|_{z=0} - \partial_y u_y|_{z=0} = 0$), which holds at the plate $z = 0$. In addition, we use the Poincaré inequality

$$\int_0^\delta u_z^2 dz \leq \frac{4\delta^2}{\pi^2} \int_0^\delta (\partial_z u_z)^2 dz, \quad (37)$$

which holds for any u_z that vanishes at the plate $z = 0$ and for any small distance δ from the plate; see Appendix A of Seis (2015).

We now consider the convective heat flux $u_z\theta$ in a small layer of width δ next to the boundary at $z = 0$. Applying the Cauchy-Schwarz inequality, the maximum principle (29), the Poincaré inequality (37), and inequality (35), we obtain

$$\begin{aligned} \left(\int_0^\delta u_z\theta dz \right)^2 &\leq \int_0^\delta u_z^2 dz \int_0^\delta \theta^2 dz \\ &\leq \Delta^2 \delta \int_0^\delta u_z^2 dz \\ &\leq \frac{4\Delta^2 \delta^3}{\pi^2} \int_0^\delta (\partial_z u_z)^2 dz \\ &\leq c^4 \Delta^2 \delta^3 \int_0^\delta (\nabla\mathbf{u})^2 dz, \end{aligned} \quad (38)$$

with

$$c = (8/3)^{1/4} \pi^{-1/2}. \quad (39)$$

Integrating the local vertical heat flux

$$F_z \equiv \frac{u_z\theta - \kappa\partial_z\theta}{\kappa\Delta/L} \quad (40)$$

in $z \in [0, \delta]$ and using relation (38), we obtain

$$\delta^{-1} \int_0^\delta F_z dz \leq \frac{c^2 \sqrt{\delta} L}{\kappa} \left(\int_0^\delta (\nabla\mathbf{u})^2 dz \right)^{1/2} + \frac{L}{\delta}. \quad (41)$$

Assuming that the time- and area-averaged kinetic energy dissipation rate at any distance from the plate cannot be larger than at the plate¹ and applying Eqs. (36) and (27), we obtain

$$\begin{aligned} \left\langle \left(\int_0^\delta (\nabla\mathbf{u})^2 dz \right)^{1/2} \right\rangle_{t,S_z} &\leq \left\langle \int_0^\delta (\nabla\mathbf{u})^2 dz \right\rangle_{t,S_z}^{1/2} \\ &\leq \delta^{1/2} \langle (\nabla\mathbf{u})^2 \rangle_{t,S_z}^{1/2} \Big|_{z=0} \\ &= \delta^{1/2} \langle (\partial_z u_x)^2 + (\partial_z u_y)^2 \rangle_{t,S_z}^{1/2} \Big|_{z=0} \\ &= \delta^{1/2} u_\tau^2 / \nu. \end{aligned} \quad (42)$$

Averaging inequality (41) in the horizontal directions and in time, making use of the fact that the Nusselt number is constant at any distance from the plate [see Eq. (11)], and applying inequality (43), we obtain

$$\text{Nu} \leq \frac{c^2 \delta L u_\tau^2}{\nu \kappa} + \frac{L}{\delta} = c^2 \text{Pr} \text{Re}_\tau^2 \frac{\delta}{L} + \frac{L}{\delta}. \quad (44)$$

The minimal value of the right-hand side of Eq. (44) is achieved at

$$\delta/L = c^{-1} \text{Pr}^{-1/2} \text{Re}_\tau^{-1}, \quad (45)$$

which leads to the following upper bound:

$$\text{Nu} \leq 2c \text{Pr}^{1/2} \text{Re}_\tau. \quad (46)$$

Note that physically the layer thickness δ is smaller than the container height L , i.e., $\delta/L < 1$ in Eq. (45). This implies that the estimate (46) is relevant only for a not too small Pr that satisfies $\text{Pr} \geq c^{-2} \text{Re}_\tau^{-2}$; cf. Eq. (45). When Pr is extremely small ($\text{Pr} < c^{-2} \text{Re}_\tau^{-2}$), inequality (44) is reduced to $\text{Nu} \leq \delta/L + L/\delta$, meaning that in this small Pr limit the upper bound (46) is reduced to $\text{Nu} \leq 2$, reflecting that the heat transport is driven mainly by conduction in that limit.

3. The relation $\text{Nu} \lesssim \text{Ra}^{1/2}$

To see that the upper bound for the scaling exponent γ does not exceed 1/2 for highly turbulent Rayleigh-Bénard flows (i.e., large Ra, the ultimate regime), we again use the fact that the vertical heat flux is constant at any distance from the plate [see Eq. (11)] and proceed similarly to Seis (2015). Averaging relation (41) in the horizontal plane and, in time, applying the top-bottom symmetry of the mean kinetic energy dissipation rate and the integral balance (13) together with inequality (42)

¹This assumption is justified because the time- and area-averaged kinetic energy dissipation rate at the plates is equal to u_τ^4/ν , which in a turbulent flow is $\gtrsim (\nu^3/L^4)\text{Re}^3$, while for the time- and volume-averaged ϵ_u it holds that $\epsilon_u \lesssim (\nu^3/L^4)\text{Re}^3$. Note also that the time- and area-averaged thermal dissipation rate at the plates is at least Nu times larger than the time- and volume-averaged thermal dissipation rate for all Prandtl and Rayleigh numbers (Shishkina and Wagner, 2006).

and

$$\left\langle \int_0^\delta (\nabla \mathbf{u})^2 dz \right\rangle_{t, S_z} \leq \frac{L \epsilon_u}{2 \nu} \quad (47)$$

for $\delta \leq L/2$, we obtain

$$\text{Nu} \leq \frac{c^2}{\sqrt{2}} \text{Ra}^{1/2} (\text{Nu} - 1)^{1/2} \left(\frac{\delta}{L} \right)^{1/2} + \frac{L}{\delta}. \quad (48)$$

Minimizing the right-hand side of the upper bound (48) by taking

$$\frac{\delta}{L} = \frac{2}{c^{4/3} \text{Ra}^{1/3} (\text{Nu} - 1)^{1/3}} \quad (49)$$

(a thin layer δ), from relations (48) and (39) we finally derive

$$\text{Nu} - 1 \leq A \text{Ra}^{1/2} \quad (50)$$

with a prefactor

$$A = 3/\pi \approx 0.955.$$

This prefactor A here is relatively large compared to what is possible to derive, and in the following we discuss how it can be reduced. However, the general result (50), i.e., that $\text{Nu} \lesssim \text{Ra}^{1/2}$, is fundamental.

Variational methods, which lead to more accurate estimates of A in the upper bound (50), always use the energy integral equations (13) and (14). To simplify further explanations, we decompose the temperature field θ into a linear function $\theta_\ell(z)$ that satisfies the boundary conditions at the plates and the residual function θ' that vanishes at the plates,

$$\theta \equiv \theta_\ell + \theta', \quad (51)$$

$$\theta_\ell(z) \equiv \Delta(1/2 - z/L). \quad (52)$$

From continuity it follows that the vertical velocity, when averaged in time and over any horizontal cross section at a distance z from the bottom plate, vanishes, i.e., $\langle u_z \rangle_{t, S_z} = 0$ for any z . From this and with Eqs. (12) and (52), we obtain

$$\text{Nu} - 1 = \frac{L}{\kappa \Delta} \langle u_z (\theta_\ell + \theta') \rangle = \frac{L}{\kappa \Delta} \langle u_z \theta' \rangle. \quad (53)$$

As θ' vanishes at the plates, it also holds that $\langle (\nabla \theta')^2 \rangle = \langle (\nabla \theta)^2 \rangle + \Delta^2/L^2$. Combining this with Eq. (14), we derive $\langle (\nabla \theta')^2 \rangle = (\Delta^2/L^2)(\text{Nu} - 1)$, which together with Eqs. (13) and (53) yields

$$\frac{L}{\kappa \Delta} \langle u_z \theta' \rangle = \frac{L^2}{\Delta^2} \langle (\nabla \theta')^2 \rangle = \frac{L^4}{\kappa^2 \text{Ra}} \langle (\nabla \mathbf{u})^2 \rangle. \quad (54)$$

Equation (54) is simply a reformulation of the energy integral equations (13) and (14).

To obtain an upper bound for $\text{Nu} - 1$ in terms of the control parameters, one can look for an upper bound of the right-hand

side of Eq. (53) among all smooth functions u_z and θ' that vanish at $z = 0$ and L and satisfy the energy equalities (54). With a free choice of the functions u_z and θ' under only these constraints, the maximum value of the right-hand side of Eq. (53) grows no slower than $\sqrt{\text{Ra}}/2$ as Ra tends to infinity. For example, for Ra growing as $\text{Ra} = (\pi k/2)^4$, with an integer k , $k \rightarrow \infty$, and the functions θ' and \mathbf{u} defined as $\theta' = \Delta \sin(\text{Ra}^{1/4} z/L)$ and $\mathbf{u} = u_z \mathbf{e}_z$, $u_z = (\kappa/L) \sqrt{\text{Ra}} \sin(\text{Ra}^{1/4} z/L)$, respectively, the restrictions (54) are fully satisfied and each term in Eq. (54) equals $\sqrt{\text{Ra}}/2$, leading to $\text{Nu} - 1 = \sqrt{\text{Ra}}/2$ as $\text{Ra} \rightarrow \infty$; cf. Eq. (53). This means that the consideration of the constraints from Eq. (54) alone would lead to an upper bound for $\text{Nu} - 1$ not smaller than $\sqrt{\text{Ra}}/2$. However, the just considered functions u and θ' satisfy neither the continuity equation $\nabla \cdot \mathbf{u} = 0$ nor the governing equations (7) and (8) nor even $\langle u_z \rangle_{t, S_z} = 0$. It is rightfully expected that imposing additional constraints apart from Eq. (54) would reduce the upper bound for $\text{Nu} - 1$ sought in the form of $A \text{Ra}^{1/2}$.

Historically the first rigorous result on the upper bound for heat transport was proved by Howard (1963), who was also the first who formulated the challenge of finding upper bounds for Nu as a variational problem. In derivations of the upper bounds, he assumed that the flows are statistically steady in time and statistically homogeneous in the horizontal cross sections for any distance from the bottom plate z . This means, respectively, that the horizontal averages of the various flow components and of their products are time independent and that the horizontal averages of the horizontal components of the velocity vanish (meaning that the horizontal average of the vertical velocity component vanishes as well, $\langle u_z \rangle_{t, S_z} = 0$, due to the continuity equation). Under the assumptions of such homogeneity in space and time, maximal heat transport is sought among all flow functions that satisfy the boundary conditions and some integral relations that are consequences of the governing Navier-Stokes and energy equations. However, this maximal heat transport can be realized with flow functions that do not necessarily satisfy the governing Navier-Stokes and energy equations themselves. Therefore, this approach leads to estimates of the maximal heat transport that may or may not be feasible in real flows but still provide mathematically rigorous upper bounds for the heat transport in Rayleigh-Bénard systems.

By maximizing the heat flux [Eq. (12)] for statistically steady (in time) and statistically homogeneous (in the horizontal plane) flows subject to the two energy integral constraints [Eqs. (13) and (14)], Howard (1963) derived that the Nusselt number cannot exceed a certain value, which for large Ra scales according to the upper bound (50), with a prefactor

$$A = \sqrt{3}/8 \approx 0.217.$$

In his derivations, Howard (1963) considered a decomposition of the temperature field into a background function that depends on z only and satisfies the boundary conditions and the rest (fluctuations). The temperature background function in Howard's case was the mean horizontal average profile of the temperature. Later, using a more complicated

z -dependent background temperature profile, [Doering and Constantin \(1996\)](#) derived an asymptotic bound (i.e., one valid for $Ra \rightarrow \infty$), which is similar to the estimate (50) but with a smaller value of A , namely,

$$A = 1/6 \approx 0.167.$$

For a review on the background method, see [Fantuzzi, Arslan, and Wynn \(2022\)](#).

What upper bounds can be obtained if the continuity equation $\nabla \cdot \mathbf{u} = 0$ is also included in the list of the constraints? In a previously discussed paper, [Howard \(1963\)](#) derived that with the continuity equation included as an additional constraint and under an additional assumption that there is only a *single* horizontal wave number that determines the temperature and velocity field, the upper bound is significantly smaller,

$$Nu - 1 \leq (Ra/248)^{3/8}, \quad (55)$$

with an upper-bound scaling exponent $\gamma = 3/8 = 0.375$. This result was important at the time of its publication and is still sometimes mentioned as a possible alternative to the upper bound ($\gamma = 1/2$) for heat transport in a general case of high- Ra Rayleigh-Bénard convection. However, since the seminal work by [Busse \(1969\)](#) it has been known that for sufficiently large Ra the assumption that the maximal heat transport can be realized by a single-horizontal-wave-number flow is incorrect, and Busse's result was also appreciated by [Howard \(1972\)](#) himself. Turbulence cannot be described via a single mode, and, by introducing the so-called multiple-boundary-layer structure of the flow and using further physical arguments, [Busse \(1969\)](#) showed that the asymptotic upper-bound exponent γ grows with the inclusion of more and more wave numbers (n) as

$$\gamma = (1 - 4^{-n})/2,$$

leading to an overall upper bound (50) with

$$A = 1/\sqrt{1035} \approx 0.031. \quad (56)$$

Much later, [Plasting and Kerswell \(2003\)](#) proved that Busse's estimate is an accurate upper bound for the heat transport [Eq. (12)] in statistically steady Rayleigh-Bénard flows, subject to the continuity equation and the two energy integral constraints [Eqs. (13) and (14)]. Under these constraints, they numerically calculated the minimal value of A in the upper bound (50), which was found to be

$$A \approx 0.02634 \quad (57)$$

as $Ra \rightarrow \infty$, i.e., very close to the estimate (56) by [Busse \(1969\)](#). This numerical value of A cannot be further improved using only a one-dimensional (z -dependent) background temperature field and without including additional constraints in the problem.

The upper bound (50) with the constant A from Eq. (57) remains the best-known estimate of the Nusselt number

upper bound for a general case of no-slip walls for all Prandtl numbers.

Note that all existing experimentally measured or numerically obtained heat transport data are far below the upper bounds for the Nusselt number scaling relations discussed in the review. Nonetheless, the exact mathematical result that the scaling exponent γ in the scaling relation $Nu - 1 \sim Ra^\gamma$ cannot exceed $1/2$ is important. It holds for three-dimensional Oberbeck-Boussinesq Rayleigh-Bénard convection in containers with no-slip plates for a fluid with a finite Prandtl number.

B. Analytical upper bounds for infinite or very large Prandtl numbers

In this section we report results for large Prandtl numbers where the upper-bound scaling exponent can be smaller than $1/2$.

1. Case of $Pr = \infty$

For infinite Prandtl numbers the rate of change of the velocity (its material derivative) can be assumed to vanish and therefore put to zero [$\partial_t \mathbf{u} + (\mathbf{u} \cdot \nabla) \mathbf{u} \equiv 0$]. Thus, in this case the governing equations are simplified and (in contrast to the full Oberbeck-Boussinesq set of equations) it is possible to show the global existence and uniqueness of their smooth solutions. This makes it possible to estimate, in particular, the bounds for higher derivatives of the temperature and vertical velocity. With these maximal regularity estimates, [Constantin and Doering \(1999\)](#) proved the following upper bound for the heat transport in the case of no-slip walls:

$$Nu - 1 \lesssim Ra^{1/3} (\log Ra)^{2/3}, \quad Pr = \infty. \quad (58)$$

Using a logarithmic background temperature profile, [Doering, Otto, and Reznikoff \(2006\)](#) improved this estimate to

$$Nu - 1 \leq 0.644 Ra^{1/3} (\log Ra)^{1/3}, \quad Pr = \infty. \quad (59)$$

Later [Otto and Seis \(2011\)](#), using an advanced background field method, further improved the estimate (59), namely, to

$$Nu - 1 \lesssim Ra^{1/3} (\log Ra)^{1/15}, \quad Pr = \infty. \quad (60)$$

Moreover, combining the maximal regularity and the background field methods, [Otto and Seis \(2011\)](#) derived

$$Nu - 1 \lesssim Ra^{1/3} (\log \log Ra)^{1/3}, \quad Pr = \infty, \quad (61)$$

which has only a double logarithm correction to $\lesssim Ra^{1/3}$. It basically indicates that, for infinite Pr , the scaling exponent in the ultimate regime is similar to that in the classical large Pr regime with $\gamma = 1/3$. For the infinite Prandtl number case, estimate (61) by [Otto and Seis \(2011\)](#) is the best available upper bound for the Nusselt number.

However, the case of $Pr = \infty$ treated in this section is unrealistic from a physics point of view. What upper bounds can be derived for large but finite Prandtl numbers?

2. Case of $\text{Pr} \gtrsim \text{Ra}^\xi$, $\xi \geq 1/3$

Wang (2004, 2007) made the next important contribution in the derivations of the upper bounds by showing that the global attractors of the infinite Prandtl number case and the large Prandtl number case remain close, which allowed the full Oberbeck-Boussinesq system of the governing equations to be considered for large but finite Prandtl numbers as a small perturbation of the simplified system for infinite Prandtl number. With this knowledge, Wang (2008) extended the result of Constantin and Doering (1999) for infinite Prandtl numbers to a more general case of finite but extremely large Prandtl numbers as follows:

$$\text{Nu} - 1 \lesssim \text{Ra}^{1/3}(\log \text{Ra})^{2/3}, \quad \text{Pr} \gtrsim \text{Ra}. \quad (62)$$

The estimate (62) by Wang (2008) was further improved by Choffrut, Nobili, and Otto (2016), who showed that the following holds for large Pr:

$$\text{Nu} - 1 \lesssim (\text{Ra} \log \text{Ra})^{1/3} + \text{Pr}^{-1/2}(\text{Ra} \log \text{Ra})^{1/2}.$$

This implies that for finite but large Prandtl numbers that grow faster than $\text{Ra}^{1/3}$, the Nusselt number is bounded by

$$\text{Nu} - 1 \lesssim (\text{Ra} \log \text{Ra})^{1/3}, \quad \text{Pr} \gtrsim (\text{Ra} \log \text{Ra})^{1/3}, \quad (63)$$

while below the borderline $\text{Pr} \sim (\text{Ra} \ln \text{Ra})^{1/3}$ the valid upper bound is

$$\text{Nu} - 1 \lesssim \left(\frac{\text{Ra}}{\text{Pr}} \log \text{Ra} \right)^{1/2}, \quad \text{Pr} \lesssim (\text{Ra} \log \text{Ra})^{1/3}. \quad (64)$$

For finite but large Prandtl numbers that grow with Ra, the estimates (63) and (64) by Choffrut, Nobili, and Otto (2016) are the best available upper bounds for the Nusselt number.

We now summarize the best-known upper bounds for the heat transport in three-dimensional as well as two-dimensional Oberbeck-Boussinesq Rayleigh-Bénard convection for no-slip boundary conditions (Plasting and Kerswell, 2003; Choffrut, Nobili, and Otto, 2016),

$$\text{Nu} \lesssim \begin{cases} (\text{Ra} \log \text{Ra})^{1/3} & \text{for } \text{Pr} \gtrsim (\text{Ra} \log \text{Ra})^{1/3}, \\ \left(\frac{\text{Ra}}{\text{Pr}} \log \text{Ra} \right)^{1/2} & \text{for } \text{Pr} \lesssim (\text{Ra} \log \text{Ra})^{1/3}, \\ 0.02634 \text{Ra}^{1/2} & \text{for all Pr.} \end{cases} \quad (65)$$

C. Analytical upper bounds for other cases

For completeness, we mention here some further mathematical results on the upper bounds on the heat transport in the limit $\text{Ra} \rightarrow \infty$ for specific instances. For a case of free-slip boundary conditions (BCs) at the heated or cooled surfaces, the upper-bound scaling exponent was proven to be only $\gamma = 5/12$ (Whitehead and Doering, 2011) if the flow is two dimensional or the Prandtl number is infinite ($\text{Pr} = \infty$). In those cases the Nusselt number for large Ra is bounded according to

$$\text{Nu} - 1 \leq 0.2295 \text{Ra}^{5/12} \quad \text{for free-slip BCs,} \\ \text{if } \text{Pr} = \infty \text{ or 2D flow.} \quad (66)$$

Wittenberg (2010) studied upper bounds for the heat transport, taking into account imperfectly conducting plates in Rayleigh-Bénard convection. The derived upper-bound scaling exponent is $\gamma = 1/2$, but the prefactor A in the $\text{Nu} \leq A \text{Ra}^\gamma$ relation was found to increase for not perfectly conducting plates.

Another result with respect to convection between no-slip rough plates was obtained by Goluskin and Doering (2016), who applied a modified background field method. For a roughness of the no-slip heated and cooled plates in a Rayleigh-Bénard container, which is described by continuous and piecewise differentiable (with square-integrable gradients) functions of the horizontal coordinates, the upper-bound scaling exponent is $\gamma = 1/2$; i.e., it is the same as in the case of smooth plates.

D. Optimal wall-to-wall steady-state heat transport

Finally, we discuss the optimal wall-to-wall heat transport method (Hassanzadeh, Chini, and Doering, 2014; Tobiasco and Doering, 2017; Motoki, Kawahara, and Shimizu, 2018; Doering and Tobiasco, 2019; Souza, Tobiasco, and Doering, 2020), which can also be formulated as a variational problem and which is another way to estimate the maximal possible heat transport in turbulent Rayleigh-Bénard convection through the maximal possible heat transport of a steady-state flow between heated lower and cooled upper surfaces of a fluid layer. We explicitly note that a steady-state flow (on which it is assumed that the flow has reached equilibrium for given control parameters of the system that remain unchanged as time goes on) generally differs from a turbulent Rayleigh-Bénard flow.

In the optimal wall-to-wall method, one traditionally considers a constraint of a constant total enstrophy in the system (that is, the averaged squared vorticity) and seeks a divergence-free, time-independent velocity field that maximizes the heat transport; these velocity flow fields are then called optimal states. More precisely one considers a constant Péclet number

$$\text{Pe} \equiv \langle (\nabla \mathbf{u})^2 \rangle^{1/2} L^2 / \kappa \quad (67)$$

and looks for a stationary velocity field \mathbf{u} that maximizes the total convective heat transport $\text{Nu} - 1 = \langle u_z \theta \rangle / (\kappa \Delta / L)$. Thus, one obtains a dependence $\text{Nu} - 1 \lesssim \text{Pe}^\eta$ for a certain η . In Rayleigh-Bénard convection, according to the integral balance (13) we have

$$\text{Pe}^2 = \text{Ra}(\text{Nu} - 1), \quad (68)$$

and therefore an estimate $\text{Nu} - 1 \lesssim \text{Pe}^\eta$ is equivalent to $\text{Nu} - 1 \lesssim \text{Ra}^\gamma$, with $\gamma = \eta / (2 - \eta)$.

Hassanzadeh, Chini, and Doering (2014) formulated and studied such a variational problem in a two-dimensional domain for free-slip boundary conditions at the plates. They found that the heat transport in the optimal states scales

as $Nu \sim Ra^{5/12}$, which was in full agreement with the rigid upper bound previously derived by [Whitehead and Doering \(2011\)](#) for this case.

[Tobasco and Doering \(2017\)](#) considered a two-dimensional case with no-slip boundary conditions. For a given enstrophy (or given Pe^2) they constructed a set of steady flows that provide

$$Nu \sim Pe^{2/3}/(\log Pe)^{4/3} \quad (69)$$

when $Pe \rightarrow \infty$. In combination with Eq. (68), this implies

$$Nu \sim Ra^{1/2}/(\log Ra)^2, \quad (70)$$

which resembles the scaling relation for the Nusselt number in the ultimate regime according to the model by [Grossmann and Lohse \(2011\)](#) and according to an extension of this model to a general Prandtl number case, which we discuss in Sec. V.

[Motoki, Kawahara, and Shimizu \(2018\)](#) applied the method to three-dimensional flows between no-slip boundaries. They numerically found the scaling relation for the Nusselt number

$$Nu - 1 \approx 0.082Pe^{2/3} \quad (71)$$

for large Pe or, in other words, $Nu - 1 \approx 0.023Ra^{1/2}$, which is close to the upper bound found by [Plasting and Kerswell](#)

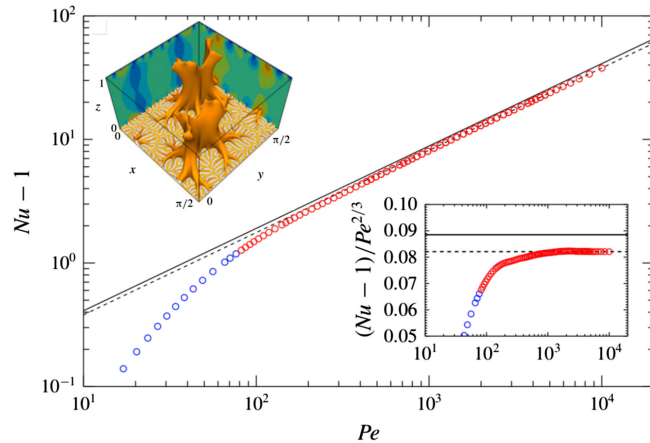


FIG. 8. Estimates for steady-state flows: Dimensionless convective heat flux $Nu - 1$ as a function of Pe in the optimal wall-to-wall heat transport steady states, calculated by [Motoki, Kawahara, and Shimizu \(2018\)](#). The blue symbols (smaller Pe) and red symbols (larger Pe) correspond to two-dimensional and three-dimensional optimal states for these stationary flows, respectively. The dashed line shows the fit $Nu - 1 = 0.0821Pe^{2/3}$ of the data for large Pe . The solid line shows the scaling $Nu - 1 = 0.0885Pe^{2/3}$, which corresponds to the rigorous upper bound $Nu - 1 = 0.02634Ra^{1/2}$ given by [Plasting and Kerswell \(2003\)](#) if the exact relation $Pe^2 = Ra(Nu - 1)$ is applied. Lower inset: the compensated Nusselt number. Upper inset: isosurfaces of the temperature gradient (dark orange) and of the second invariant of the velocity gradient tensor $\partial_j u_i \partial_i u_j$ (light gray) in the optimal three-dimensional steady state for $Pe = 1.6 \times 10^8$ (only the lower half of the domain is shown). Adapted from [Motoki, Kawahara, and Shimizu, 2018](#).

(2003); see Fig. 8. The obtained optimal three-dimensional states have a much more complicated structure than simple rolls. In the inset of Fig. 8 one can see an example of temperature isosurfaces for a specific value of Pe . [Motoki, Kawahara, and Shimizu \(2018\)](#) showed that at large Pe the optimal velocity field exhibits hierarchical self-similarity, and near the walls the self-similar vortical structures locally enhance the heat transport and build logarithmic mean temperature profiles. We note that such hierarchical structures at the wall resemble the attached eddy hypothesis for wall-bounded shear flows ([Marusic and Monty, 2019](#)).

To summarize, the optimal wall-to-wall heat transport method is capable of delivering the structures of the optimal steady flows that transport maximal heat for a given enstrophy value. The corresponding heat transport estimates are similar to the upper bounds for the heat transport in the previously discussed general case of Rayleigh-Bénard convection. However, these steady-state flows differ from real Rayleigh-Bénard flows.

V. THEORETICAL MODELS FOR THE HEAT TRANSPORT AT LARGE RAYLEIGH NUMBERS: A HISTORICAL PERSPECTIVE

To date no general analytical solutions of the system of Eqs. (1)–(3) could be derived; i.e., it hitherto has not been possible to solve (or even to prove or refute the existence and uniqueness of the solution of) the Navier-Stokes equation. The extreme difficulty of the problem was recognized by The Clay Mathematics Institute, which identified the problem as one of the seven unsolved Millennium Prize Problems ([Fefferman, 2006](#)). Asymptotic solutions of the governing equations (1)–(3) for $Ra \rightarrow \infty$ could not be derived either, nor even could asymptotic expressions for integral quantities like Re or Nu as functions of the control parameters Ra and Pr . All of these tasks still seem to be infeasible. Therefore, any scaling theory for the heat and momentum transport has to use heuristic arguments with different levels of rigor.

In this section we take a digression into the history of theoretical investigations and models of the heat transport scaling relations in turbulent Rayleigh-Bénard convection at extremely large Rayleigh numbers, i.e., in the ultimate regime, so that current developments can be put into context. In particular, we extract and contrast the assumptions, which are made to derive each considered model for the ultimate regime in Rayleigh-Bénard convection, and discuss the outcomes of the models that follow from the chosen assumptions. The overview starts with the most heuristic models, which are based on more speculative and less rigorous argumentation.

We now make two remarks: First, while describing the assumptions made to derive this or that particular model, we do not always follow the descriptions given in the original articles step by step. The reason for this is that sometimes in those articles a chain of separate assumptions are made that are neither used separately anywhere nor verified, and, *de facto*, only a consequence of this chain of assumptions is used to derive the model, which instead can be formulated as one key assumption. In such a case, in our discussion we replace the entire chain of the assumptions made in the original article

simply with this single key assumption. Second, we discuss here only the leading terms in the scaling relations and ignore the lower-order terms in order to make the description of the models for the ultimate regime more focused. We also do not discuss the values of the appearing constants and prefactors.

A. Priestley (1954) model

Priestley (1954) put forward a purely heuristic argument: He proposed that at high Ra, the efficient convective heat transport in the bulk of the fluid layer should not be affected by the separation of the plates, and that the total heat transport should be fully controlled by the thermal boundary layers adjacent to the top and bottom plates (“thermal shortcut” in the bulk). Thus, the total heat flux q can depend on any flow system parameter but not on the depth of the fluid layer L . Assuming that the Nusselt number $\text{Nu} \equiv q/(\kappa\Delta/L)$ scales as the Rayleigh number $\text{Ra} \equiv \alpha g\Delta L^3/\kappa\nu$ taken to a certain power γ , $\text{Nu} \sim \text{Ra}^\gamma$, one has

$$q \equiv \frac{\kappa\Delta}{L}\text{Nu} \sim \frac{\kappa\Delta}{L}\text{Ra}^\gamma \propto L^{3\gamma-1}. \quad (72)$$

With Priestley’s assumption that q is independent of L , one immediately obtains that the scaling exponent equals $\gamma = 1/3$ (these two statements are equivalent).² The outcome of the Priestley model ($\gamma = 1/3$) is similar to that of the model of Malkus (1954), which we later discuss. The scaling (72) coincides with the scaling of regime IV_u of GL theory (Grossmann and Lohse, 2000, 2001), but Eq. (72) does not generally hold, as we elaborated in Sec. III, though Priestley had originally suggested it for a much larger range in parameter space.

In the remainder of this section we also mention some other assumptions that are equivalent to that suggested by Priestley. These assumptions were put forward in other publications long after Priestley (1954), with the claim that they would be new models that would propose the universality of the $\gamma = 1/3$ scaling. However, those “new” models are nothing more than a paraphrase of Priestley’s model. In particular, we note that the following four assumptions are completely equivalent:

- (a) The exponent γ in the relation $\text{Nu} \sim \text{Ra}^\gamma$ is equal to $\gamma = 1/3$.
- (b) The global heat flux $q \equiv (\kappa\Delta/L)\text{Nu}$ is independent of the depth of the fluid layer L .
- (c) The thickness of the thermal boundary layer $\lambda_\theta \equiv L/2\text{Nu}$ is independent of L .
- (d) The thickness of the thermal boundary layer λ_θ scales asymptotically as the Batchelor scale

$$\eta_B \equiv (\nu\kappa^2/\epsilon_u)^{1/4}. \quad (73)$$

The equivalence of (a) and (b) follows from relation (72), and the equivalence of (b) and (c) follows from $\lambda_\theta = \kappa\Delta/2q$. The equivalence of (d) and (a) [and hence to the other assumptions

(b) and (c)] follows from the definition of the Batchelor scale (73), the integral relation (13) for the kinetic energy dissipation rate ϵ_u , and $\text{Nu} \approx \text{Nu} - 1$ for large Ra. In other words, once any of the assumptions (b)–(d) is taken,³ one thus unavoidably and immediately has (a): $\text{Nu} \sim \text{Ra}^{1/3}$.

The kinetic energy dissipation rate ϵ_u varies scalingwise between $\epsilon_u \sim (\nu^3/L^4)\text{Re}^2$ (laminar flow) and $\epsilon_u \sim (\nu^3/L^4)\text{Re}^3$ (fully developed turbulent flow). When $\text{Nu} \sim \text{Ra}^{1/3}$ and $\epsilon_u \sim (\nu^3/L^4)\text{Re}^2$, from Eq. (13) one derives $\text{Re} \sim \text{Pr}^{-1}\text{Ra}^{2/3}$ (regime III_∞ in GL theory), and when $\epsilon_u \sim (\nu^3/L^4)\text{Re}^3$ one derives $\text{Re} \sim \text{Pr}^{-2/3}\text{Ra}^{4/9}$ (regime IV_u in GL theory). This means that Priestley’s model (and models equivalent to it) cannot offer explanations of the heat and momentum transport outside the classical regime.

B. Spiegel (1971) model

Another heuristic argument was proposed by Spiegel (1971), who assumed that in large astrophysical and geophysical systems with extremely large Ra, the total heat flux q should be diffusion free; that is, it should be independent of the viscosity ν and the thermal diffusivity κ . Assuming that $\text{Nu} \sim \text{Pr}^\zeta\text{Ra}^\gamma$ for certain values of ζ and γ , one obtains

$$q \equiv \frac{\kappa\Delta}{L}\text{Nu} \sim \frac{\kappa\Delta}{L}\text{Pr}^\zeta\text{Ra}^\gamma \propto \kappa^{1-\zeta-\gamma}\nu^{\zeta-\gamma}. \quad (74)$$

The independence of q from κ and ν implies that $\gamma = 1/2$ and $\zeta = 1/2$. Thus, under Spiegel’s assumption one obtains that the nondimensional heat transport should scale as

$$\text{Nu} \sim \text{Pr}^{1/2}\text{Ra}^{1/2}. \quad (75)$$

This idealized relation cannot be realized other than asymptotically, since the Rayleigh-Bénard system, where all of the heat comes into the system and leaves it through the rigid top and bottom plates, cannot be completely free from the processes within the thermal boundary layers, where the viscosity and thermal diffusivity always play a role.

C. Herring, Stewartson, and Roberts (1966) model

At the beginning of the computational fluid mechanics era, when computers were far less powerful than they are today, it was impossible to numerically solve the full set of the governing equations for thermal convection, even for relatively small values of Ra. Therefore, one of the first ideas (Herring, 1963) was to numerically solve reduced equations for the steady state, where almost all nonlinear terms are neglected, apart from those that originate from the interactions of the velocity or temperature fluctuations with the horizontally averaged temperature field. To further simplify the problem, Herring (1963, 1964) considered these equations for the case when the horizontal temperature and velocity fluctuations are described by a *single* horizontal wave number. Later, his simulations for $\text{Ra} \leq 10^6$ were found to be in

²The heat flux is often also defined as $\rho c_p q$, i.e., as the heat flux q as defined here, multiplied by the density ρ and the specific heat at constant pressure c_p ; however, this does not affect the derivations.

³For example, Lindborg (2023) assumed (d), which immediately gives (a).

agreement with the asymptotic relation $\text{Nu} \sim (\text{Ra}^{3/2} \ln \text{Ra})^{1/5}$ derived by [Roberts \(1966\)](#) and [Stewartson \(1966\)](#) from Herring's reduced equation and under the additional assumption that only one considered wave number ($\sim \text{Ra}^{1/4}$) maximizes the Nusselt number as $\text{Ra} \rightarrow \infty$. However, this Stewartson-Roberts formula cannot describe the heat transport in real Rayleigh-Bénard systems, due to the single-wave-number constraint in their theoretical consideration. Indeed, already in 1971 [Chan \(1971\)](#) had derived for the infinite Prandtl number limit that the maximum Nusselt number is realized only asymptotically on the solutions that involve an *infinite* number of horizontal wave numbers, and that a steeper scaling relation than in the aforementioned Stewartson-Roberts formula then holds, namely, $\text{Nu} \sim \text{Ra}^{1/3}$. For a finite Prandtl number, the broad horizontal wave number spectrum plays an even more crucial role. This is also connected to the previously discussed result by [Busse \(1969\)](#), who showed that for a finite Prandtl number the upper bound for the Nusselt number is realized only asymptotically on the solutions that involve an infinite number of horizontal wave numbers, and that the bounding scaling exponent in this case is $1/2$, i.e., $\text{Nu} \lesssim \text{Ra}^{1/2}$. Based on the previously discussed results, we emphasize that any approach to exploring the ultimate regime in turbulent thermal convection that ignores (though partly) the nonlinear terms in the governing equations or assumes that the highly turbulent flow can be well represented by a single-wave-number mode does not hold much promise.

D. Malkus (1954) model

Almost simultaneously with Priestley, [Malkus \(1954\)](#) published his famous article. (Priestley's paper was received by the journal on October 29, 1953, and Malkus's paper was received on November 26, 1953.) The linear stability analysis of [Pellew and Southwell \(1940\)](#), which originally was used to derive the onset of convection, was extended by Malkus to the turbulent case, for which he considered turbulent fluctuation on top of the mean flow. With this Malkus showed that if the velocity, the temperature (with a subtracted mean vertical profile), and their time-averaged product can be described by only n_0 first Fourier modes, then the upper limit for the mean convective heat flux ($\text{Nu} - 1$) scales as $\sim n_0$. Malkus further showed that the Rayleigh number (called λ_{n_0} in his paper) for the onset of the instability of the next mode (i.e., the mode number $n_0 + 1$) scales as $\sim n_0^3$. Combining $\text{Nu} - 1 \sim n_0$ with $\text{Ra} \equiv \lambda_{n_0} \sim n_0^3$, one obtains the Malkus scaling relation

$$\text{Nu} - 1 \sim \text{Ra}^{1/3}. \quad (76)$$

Note that in Malkus's analysis, the contributions of the nonlinear terms in the equations were ignored.

Malkus's name is firmly connected with the "1/3" relation (76). However, in his paper ([Malkus, 1954](#)), Malkus further wrote: "Unfortunately, a large second-order term due to $\mathbf{u} \cdot \mathbf{u}$ is also present. If the approximate spectrum for $\mathbf{u} \cdot \mathbf{u} \dots$ is used, this term dominates all others and determines that, for large n_0 , λ_{n_0} will vary as $(\nu/\kappa)n_0^2$." This implies then that in the strongly nonlinear case the expected scaling relation should be $\text{Nu} \sim \text{Ra}^{1/2}$. However, note that Malkus did not predict this

1/2 regime, motivated by the fact that in his experiment "neither the appearance of the Prandtl number, ν/κ , nor n_0^2 agrees with the data."

E. Kraichnan (1962) model

The seminal work of [Kraichnan \(1962\)](#) was the first to propose that for extremely large Ra and moderate Pr the Nusselt number can scale as steeply as $\sim \text{Ra}^{1/2}$, subject to logarithmic corrections. Kraichnan acknowledged that the increasing shear in turbulent Rayleigh-Bénard convection, along with the formation of turbulent boundary layers, leads to a fundamental transition in the scaling laws that govern the heat and momentum transport. Because of the relevance of the paper and as it is somewhat difficult to comprehend, we discuss it further here.

For different Pr regimes, Kraichnan considered different assumptions and obtained different scaling relations for Nu and Re , which we later discuss. For all cases, however, it is assumed that, in the core part of a turbulent Rayleigh-Bénard container (at $z \approx L/2$), there is a balance between the non-linear convective term and the buoyancy term in the momentum Navier-Stokes equation,

$$\frac{u_{\text{rms}}^2}{z} \sim \alpha g \theta_{\text{rms}} \quad \text{at } z \approx L/2, \quad (77)$$

and that the dimensionless heat flux scales as

$$\text{Nu} \sim \frac{u_{\text{rms}} \theta_{\text{rms}}}{\kappa \Delta / L} \quad \text{at } z \approx L/2, \quad (78)$$

where u_{rms} and θ_{rms} are the rms values of the vertical velocity and the temperature, respectively. As the mean flow at $z \approx L/2$ vanishes, the velocity of the wind of turbulence is assumed to be well represented by u_{rms} , i.e., $U \sim u_{\text{rms}}$. Combining this with relations (77) and (78), one obtains $\text{Re} \sim u_{\text{rms}} L / \nu$ at $z \approx L/2$ and

$$\text{Re}^3 \sim \text{Ra} \text{Pr}^{-2} \text{Nu}. \quad (79)$$

Kraichnan used the scaling relation (79) as one of his key assumptions to derive his scaling relations for the different Pr cases, which we consider in Secs. [V.E.1–V.E.3](#).

1. Large Prandtl number case

For large $\text{Pr} \gtrsim 1$, like the previous researchers [Kraichnan \(1962\)](#) concluded that the heat transport should scale as $\text{Nu} \sim \text{Ra}^{1/3}$. More precisely, for large Pr , in addition to Eq. (79), [Kraichnan \(1962\)](#) assumed that close to the plate there would be a balance between the diffusive term and the buoyancy term in the Navier-Stokes equation,

$$\nu u_{\text{rms}} / z^2 \sim \alpha g \theta_{\text{rms}}, \quad (80)$$

which he used to estimate

$$\nu u_{\text{rms}} / \lambda_\theta^2 \sim \alpha g \Delta \quad \text{at } z \sim \lambda_\theta \equiv L / (2\text{Nu}). \quad (81)$$

Kraichnan's third, empirically motivated assumption for large Pr is that the Peclet number Pe_{rms} ,

$$Pe_{rms} \equiv u_{rms}z/\kappa = \text{const} \quad \text{at } z \sim \lambda_\theta \equiv L/(2Nu), \quad (82)$$

is constant at $z \sim \lambda_\theta$ (independent of Ra and Pr). Combining the assumptions (81) and (82), one obtains the proposed scaling relation

$$Nu \sim Pr^0 Ra^{1/3}, \quad (83)$$

which if combined with the assumption (79) gives $Re \sim Pr^{-2/3} Ra^{4/9}$ (as in the GL regime IV_u).

However, for extremely large Ra and not large Pr, Kraichnan proposed a qualitative change in the boundary-layer structure, which should affect the global heat and momentum transport in the system.

2. Small Prandtl numbers and large Rayleigh numbers

Kraichnan realized that when Ra tends to infinity and Pr is not too large the boundary layers must become turbulent, with a typical logarithmic profile of the mean horizontal velocity $\langle u(z) \rangle$,

$$\frac{\langle u \rangle}{u_\tau} \sim \log \frac{u_\tau z}{\nu}, \quad (84)$$

where z is the distance from the isothermally heated or cooled plate. [For simplicity, in Eq. (84) and in the following relations we skip all prefactors and additive constants and keep only the leading terms.] In other words, for extremely large Ra in this case, Kraichnan's second assumption [in addition to Eq. (79)] is

$$Re \sim Re_\tau \log(Re_\tau), \quad (85)$$

where Re and $Re_\tau \equiv u_\tau L/\nu$ are the Reynolds numbers based on the wind velocity in the core part of the domain and the friction velocity u_τ , respectively.

The third, heuristic assumption in Kraichnan's model for small Pr and large Ra is similar to Eq. (82) but with u_τ taken instead of u_{rms} . That is, that the following Pe_τ is independent of Ra and Pr,

$$Pe_\tau \equiv u_\tau z/\kappa = \text{const} \quad \text{at } z \sim \lambda_\theta \equiv L/(2Nu), \quad (86)$$

or, in other words, that

$$Nu \sim Pr Re_\tau. \quad (87)$$

Combining the three assumptions (79), (85), and (87), one derives the following Kraichnan relations:

$$Nu \sim \frac{Pr^{1/2} Ra^{1/2}}{(\log Ra)^{3/2}}, \quad (88)$$

$$Re \sim \frac{Pr^{-1/2} Ra^{1/2}}{(\log Ra)^{1/2}}, \quad (89)$$

which he proposed to hold for large Rayleigh numbers and small Prandtl numbers ($Pr \leq 0.15$, where the estimate of the transitional Pr was indicated to be of low confidence.)

3. Moderate Prandtl numbers and large Rayleigh numbers

For intermediate values of Prandtl numbers ($0.15 < Pr \lesssim 1$), instead of Eq. (87) Kraichnan took another heuristic assumption

$$Nu \sim Pr^{1/2} Re_\tau, \quad (90)$$

which can be interpreted as a modification of assumption (86), where the velocity u_τ (at the edge of the viscous sublayer $z_\tau \equiv \nu/u_\tau$) is linearly extrapolated to the edge of the thermal BL as $(\lambda_\theta/z_\tau)u_\tau$.

From the three assumptions (79), (85), and (90), Kraichnan then obtained scaling relations that are slightly different from Eqs. (88) and (89) with respect to the Pr dependences, namely,

$$Nu \sim \frac{Pr^{-1/4} Ra^{1/2}}{(\log Ra)^{3/2}}, \quad (91)$$

$$Re \sim \frac{Pr^{-3/4} Ra^{1/2}}{(\log Ra)^{1/2}}. \quad (92)$$

Note that Kraichnan's first assumption (79) for large Nu (where $Nu - 1 \sim Nu$) is equivalent to the proposition that the mean kinetic energy dissipation rate scales as in homogeneous isotropic turbulent flows,

$$\epsilon_u \sim \frac{\nu^3}{L^4} Re^3 \quad (93)$$

[compare Eq. (93) to Eq. (13)], which seems to be too optimistic for any wall-bounded flow, including Rayleigh-Bénard convection. The assumptions (87) and (90) do not seem to hold for all large Ra, as they are based on an empirical knowledge for a restricted parameter range outside the ultimate regime.

Comparing the scaling relations for the three Kraichnan's regimes (83), (88), and (91), one concludes that the transition between the moderate Pr regime and small Pr regime goes along a constant Pr ($Pr \approx 0.15$), while the transition to the large Pr regime should scale as $Pr \sim Ra^{2/3}$ (with a logarithmic correction). The shortcoming of the chosen assumptions and, therefore, the obtained outcomes of the model becomes apparent as a contradiction to the upper bound for the Nusselt number at large Pr (Choffrut, Nobili, and Otto, 2016). More precisely, when Pr grows faster than $Ra^{1/3}$ but slower than $Ra^{2/3}$, that is, as $Pr \sim Ra^a$, $1/3 < a < 2/3$, the heat transport, according to the scaling relation (91), should go as $Nu \sim Ra^\gamma$, with $\gamma = -a/4 + 1/2 > 1/3$, which contradicts the upper bound for the Nusselt number $\lesssim Ra^{1/3}$, which holds for $Pr \gtrsim Ra^{1/3}$ (all subject to logarithmic corrections); see Eq. (65).

F. Castaing *et al.* (1989) model and Shraiman and Siggia (1990) model

The models proposed by Castaing *et al.* (1989) and Shraiman and Siggia (1990) were based mainly on the

experimental results of [Castaing *et al.* \(1989\)](#) for Rayleigh-Bénard convection in cryogenic helium gas for Ra up to 6×10^{12} . In that experiment, they observed that the scaling exponent γ in the $Nu \sim Ra^\gamma$ relation was close to $2/7$ and offered a certain theoretical explanation of these observations. They assumed that the dimensionless heat flux scales as

$$Nu \sim \frac{u_c \theta_c}{\kappa \Delta / L}, \quad (94)$$

where the typical velocity u_c and the temperature θ_c are assumed to be related as

$$u_c \sim \sqrt{\alpha g \theta_c L} \sim \frac{\alpha g \Delta \lambda_\theta}{\nu / \lambda_\theta}, \quad (95)$$

with $\lambda_\theta \equiv L / (2Nu)$ the thickness of the thermal boundary layer, where again a thermal shortcut in the bulk is assumed. The heuristic assumptions (95) used by [Castaing *et al.* \(1989\)](#) are equivalent to

$$\frac{\theta_c}{\Delta} \sim \left(\frac{u_c}{u_{ff}} \right)^2 \quad (96)$$

and

$$\frac{u_c}{u_{ff}} \sim \frac{1}{Nu^2} \sqrt{\frac{Ra}{Pr}}, \quad (97)$$

which in combination with the scaling (94) gives the results of [Castaing *et al.* \(1989\)](#),

$$Nu \sim Pr^{-1/7} Ra^{2/7}, \quad (98)$$

$$Re \sim Pr^{-5/7} Ra^{3/7}, \quad (99)$$

where the Reynolds number is based on u_c .

The model by [Shraiman and Siggia \(1990\)](#) offers scaling relations similar to those of relations (98) and (99) with some logarithmic corrections, and analysis of the assumptions made in that model can explain the meaning of the heuristic relations (94) and (95).

As an alternative to Kraichnan's first assumption [Eqs. (79) and (93)], [Shraiman and Siggia \(1990\)](#) proposed to simply take

$$\epsilon_u \sim \frac{\nu^3}{L^4} Re_\tau^3, \quad (100)$$

by virtue of the fact that $Re_\tau < Re$ and that in the experiments by [Castaing *et al.* \(1989\)](#) and [Sano, Wu, and Libchaber \(1989\)](#) the scaling (93) was not observed. Instead, the quantity $(L^4/\nu^3)\epsilon_u/Re^3$ showed a monotonic decrease with increasing Ra .

The second assumption of [Shraiman and Siggia \(1990\)](#), as in Kraichnan's model, is the scaling relation (85), which reflects that the velocity boundary layers are turbulent with logarithmic profiles. The crucial third assumption in the [Shraiman and Siggia \(1990\)](#) model is that a considered large

Pr thermal boundary layer should always scale as in the laminar Prandtl-Blasius thermal BL case for $Pr \gg 1$. More precisely the horizontal velocity within the thermal BL was approximated as a linear function of the distance from the plate $u = (u_\tau^2/\nu)z$, meaning that, with a similarity variable $y \equiv z/(x^{1/3}L^{2/3})$ and the nondimensional temperature $\theta(y) = (T_+ - T)/\Delta$, the thermal BL equation should take the form

$$\theta'' + Pr Re_\tau^2 y^2 \theta' = 0, \quad (101)$$

$$\theta|_{y=0} = 0, \quad (102)$$

$$\theta|_{y \rightarrow \infty} = 1/2. \quad (103)$$

The prime denotes the derivative with respect to the similarity variable y . The solution of the thermal BL equation (101) with the boundary conditions (102) and (103) then is

$$\theta(y) = \frac{Pr^{1/3} Re_\tau^{2/3}}{2 \times 3^{1/3} \Gamma(4/3)} \int_0^y \exp\left(-\frac{Pr Re_\tau^2}{3} \eta^3\right) d\eta, \quad (104)$$

with Γ the gamma function. This implies that the Nusselt number should scale as

$$Nu \sim \theta'|_{z=0} \sim Pr^{1/3} Re_\tau^{2/3}. \quad (105)$$

The scaling relation (105) can also be written in terms of the friction coefficient $C_f \equiv Re_\tau^2/Re^2$ as $Nu \sim C_f^{1/3} Pr^{1/3} Re^{2/3}$ ([Lévêque, 1928](#)). Relation (105) is the third assumption in the model of [Shraiman and Siggia \(1990\)](#), which together with the other assumptions (85) and (100) lead to the following scaling relations in the model of [Shraiman and Siggia \(1990\)](#):

$$Nu \sim Pr^{-1/7} Ra^{2/7}, \quad (106)$$

$$Re \sim Pr^{-5/7} Ra^{3/7} \log Ra. \quad (107)$$

In this model, the kinetic energy dissipation rate seems to be underestimated; cf. the scaling (100). More critical here, however, is the assumption that for large Ra the thermal boundary layer remains scalingwise laminar, of the Prandtl-Blasius type for large Pr . For $Ra \rightarrow \infty$ this assumption seems to be unrealistic.

G. Chavanne *et al.* (1997) model

A modification of Kraichnan's model was proposed by [Chavanne *et al.* \(1997\)](#), who also reported an experimentally obtained transition to the ultimate regime for Rayleigh-Bénard convection in cryogenic helium in the Ra range $10^{11} \lesssim Ra \lesssim 10^{14}$; see Sec. VII.B. As in Kraichnan's model, [Chavanne *et al.*](#) assumed a logarithmic velocity profile [relation (85)] and the scaling (79) of the mean kinetic energy dissipation rate as in the isotropic turbulence case. However, instead of taking the empirical relation (87) or (90), [Chavanne *et al.* \(1997\)](#) proposed that in the highly turbulent regime

logarithmic profiles should also be expected for the temperature (Landau, 1944; Landau and Lifshitz, 1987),

$$\frac{\langle \theta \rangle_t}{\Delta} \sim \frac{\text{Nu}}{\text{Pr Re}_\tau} \log \frac{u_\tau z}{\kappa}, \quad (108)$$

which leads to the following third assumption in their model:

$$\text{Nu} \sim \frac{\text{Pr Re}_\tau}{\log(\text{Re}_\tau)}. \quad (109)$$

Combining the three assumptions (79), (85), and (109) of the model of Chavanne *et al.* (1997) leads to the following scaling relations:

$$\text{Nu} \sim \frac{\text{Pr}^{1/2} \text{Ra}^{1/2}}{(\log \text{Ra})^3}, \quad (110)$$

$$\text{Re} \sim \frac{\text{Pr}^{-1/2} \text{Ra}^{1/2}}{\log \text{Ra}}, \quad (111)$$

which were proposed for the large Ra regime. In this model, as in Kraichnan's model, the assumption (79) or, equivalently, the assumption (93) seems to be unfeasible for wall-bounded Rayleigh-Bénard flows. And for truly large Prandtl numbers that grow as a power law of Ra, the effective scaling exponent in the Nu versus Ra scaling relation would be larger than 1/2, which means that the scaling relation (110) cannot hold for Prandtl numbers larger than a certain threshold: $\mathcal{P}r \sim 1$.

H. Grossmann and Lohse (2011) model

In the model of Grossmann and Lohse (2011, 2012), turbulent velocity and temperature boundary layers in the ultimate regime were proposed, with logarithmic profiles of both the velocity and the temperature, and therefore relations (85) and (109) are the first two assumptions in their model. However, the proposed scaling relation for the mean kinetic energy dissipation rate ϵ_u differs from the relation (79) considered in the models of Kraichnan (1962) and Chavanne *et al.* (1997). Instead, Grossmann and Lohse (2011) assumed that the scaling of ϵ_u in turbulent Rayleigh-Bénard convection should be as in sheared, wall-bounded turbulent flows, i.e., as

$$\epsilon_u = \frac{\nu^3}{L^4} C_f \text{Re}^3, \quad (112)$$

with a friction coefficient C_f ,

$$C_f \equiv \frac{\text{Re}_\tau^2}{\text{Re}^2}. \quad (113)$$

Taking into account the analytical result (13), from Eqs. (85), (112), and (113) one obtains

$$\text{RaPr}^{-2}(\text{Nu} - 1) \sim \text{Re}_\tau^3 \log(\text{Re}_\tau). \quad (114)$$

Combining relations (85), (109), and (114), one derives the following scaling relations, which were proposed by Grossmann and Lohse (2011):

$$\text{Nu} \sim \frac{\text{Pr}^{1/2} \text{Ra}^{1/2}}{(\log \text{Ra})^2}, \quad (115)$$

$$\text{Re} \sim \text{Pr}^{-1/2} \text{Ra}^{1/2}. \quad (116)$$

The model has consistent assumptions that are usually considered for sheared, wall-bounded turbulent flows, including the turbulent thermal and viscous boundary layers with their logarithmic profiles. However, as in the previous models, the proposed scaling relation (115) cannot hold for all Prandtl numbers, since with any growth of Pr as a power law of Ra the proposed heat flux would exceed the upper bound that has the scaling exponent 1/2.

I. Proposed model for the ultimate regime

In this section, we analyze the Prandtl number dependences in the various subregimes of the ultimate regime and propose a model that includes these dependences. We start the derivation with a discussion on the boundary-layer equations for turbulent Rayleigh-Bénard convection.

1. Turbulent flow along a plate

We now consider the equations for the horizontal velocity u_x (along the turbulent wind when it exists and along any horizontal direction otherwise) and for the temperature θ for a turbulent flow next to a rigid horizontal wall,

$$\partial_t u_x + \mathbf{u} \cdot \nabla u_x + \partial_x p / \rho = \nu \nabla^2 u_x, \quad (117)$$

$$\partial_t \theta + \mathbf{u} \cdot \nabla \theta = \kappa \nabla^2 \theta, \quad (118)$$

and conduct the Reynolds decomposition of the flow components into their time averages and fluctuations, i.e., $\mathbf{u} = \langle \mathbf{u} \rangle_t + \mathbf{u}'$ and $\theta = \langle \theta \rangle_t + \theta'$. We further assume that the convective contributions from the mean, time-averaged flow are much smaller than the contributions from the Reynolds stresses, i.e., $|\langle \mathbf{u} \rangle_t \cdot \langle \nabla u_x \rangle_t| \ll |\langle \mathbf{u}' \rangle_t \cdot \langle \nabla u_x' \rangle_t|$ and $|\langle \mathbf{u} \rangle_t \cdot \langle \nabla \theta \rangle_t| \ll |\langle \mathbf{u}' \rangle_t \cdot \langle \nabla \theta' \rangle_t|$, and that the horizontal averages of the horizontal derivatives vanish, $\langle \partial_x * \rangle_{t,s_z} = 0$. Under the aforementioned assumptions, the time and area averaging of Eqs. (117) and (118) leads to the following reduced equations:

$$\partial_z \langle u_z' u_x' \rangle_{t,s_z} = \nu \partial_z^2 \langle u_x \rangle_{t,s_z}, \quad (119)$$

$$\partial_z \langle u_z' \theta' \rangle_{t,s_z} = \kappa \partial_z^2 \langle \theta \rangle_{t,s_z}. \quad (120)$$

Integrating Eqs. (119) and (120) from 0 to z , introducing the eddy viscosity ν_τ and the eddy thermal diffusivity κ_τ ,

$$\langle u_z' u_x' \rangle_{t,s_z} \equiv -\nu_\tau \partial_z \langle u_x \rangle_{t,s_z}, \quad (121)$$

$$\langle u_z' \theta' \rangle_{t,s_z} \equiv -\kappa_\tau \partial_z \langle \theta \rangle_{t,s_z}, \quad (122)$$

and taking into account the vanishing fluctuations at the plate and that $(\kappa\Delta/L)\text{Nu} \equiv -\kappa\partial_z\langle\theta\rangle_{t,s_z}|_{z=0}$ and $u_\tau^2 \equiv \nu\partial_z\langle u_x\rangle_{t,s_z}|_{z=0}$, we obtain the following useful relations:

$$u_\tau^2 = (\nu + \nu_\tau)\partial_z\langle u_x\rangle_{t,s_z}, \quad (123)$$

$$(\kappa\Delta/L)\text{Nu} = -(\kappa + \kappa_\tau)\partial_z\langle\theta\rangle_{t,s_z}. \quad (124)$$

2. Prandtl number dependence of the ultimate regime

To close the system (123) and (124), we need to know the functional dependences of the eddy viscosity $\nu_\tau(z)$ and the eddy thermal diffusivity $\kappa_\tau(z)$. Near the plate, within the viscous sublayer of the thickness $z_\tau \equiv \nu/u_\tau$, both the eddy viscosity $\nu_\tau(z)$ and the eddy thermal diffusivity $\kappa_\tau(z)$ behave as cubic functions of the distance from the plate $\propto z^3$, and therefore the contribution of the eddy viscosity and eddy thermal diffusivity within the viscous sublayer is negligible. The somewhat counterintuitive fact that $\nu_\tau(z)$ and $\kappa_\tau(z)$ behave as cubic functions of z follows from the continuity equations for the mean flow and for the fluctuations that lead to the vanishing of the first terms in the Taylor expansions (considered at $z=0$) of $\nu_\tau(z)$ and of $\kappa_\tau(z)$; see Antonia (1980), Antonia and Kim (1991), Shishkina *et al.* (2015), and Shishkina, Horn *et al.* (2017).

To estimate the mean vertical profiles of $\nu_\tau(z)$, $\kappa_\tau(z)$, and $\epsilon_u(z)$ outside the viscous sublayer, we follow Landau and make the following assumptions (Landau and Lifshitz, 1987):

- The turbulent Prandtl number Pr_τ ,

$$\text{Pr}_\tau \equiv \nu_\tau/\kappa_\tau, \quad (125)$$

is independent of (or only weakly dependent on) the molecular Pr.

- The mean vertical profiles of $\nu_\tau(z)$, $\kappa_\tau(z)$, and $\epsilon_u(z)$ are determined exclusively by the momentum transferred by the fluid to a solid wall, i.e., the friction velocity u_τ , and by the distance to the plate, subject to a certain Prandtl number dependence $z\text{Pr}^\zeta$.

By dimensional analysis, these assumptions imply that outside the viscous sublayer $\nu_\tau(z)$, $\kappa_\tau(z)$, and $\epsilon_u(z)$ should scale as

$$\nu_\tau(z) = \varkappa u_\tau z \text{Pr}^\zeta, \quad (126)$$

$$\kappa_\tau(z) = \varkappa_\theta u_\tau z \text{Pr}^\zeta, \quad (127)$$

$$\epsilon_u(z) = \frac{\varkappa_e u_\tau^3}{z \text{Pr}^\zeta}, \quad (128)$$

with the positive constants \varkappa , \varkappa_θ , and \varkappa_e .

We further propose that the turbulent diffusivities ν_τ and κ_τ are controlled by the smallest of the two fluid characteristics of diffusion, i.e., by either ν or κ . In other words, both ν_τ and κ_τ should be proportional to $\sqrt{\nu\partial_z\langle u_x\rangle_{t,s_z}|_{z=0}}$ for small $\text{Pr} \lesssim 1$, and to $\sqrt{\kappa\partial_z\langle u_x\rangle_{t,s_z}|_{z=0}}$ for large $\text{Pr} \gtrsim 1$, which implies that $\zeta = 0$ for $\text{Pr} \lesssim 1$ and $\zeta = -1/2$ for $\text{Pr} \gtrsim 1$.

Now, from Eqs. (13), (123), (124), and (126)–(128) we can derive the scaling relations that we propose for the ultimate regime for both small and large Pr.

Dividing both sides of Eq. (123) by $\nu + \nu_\tau$, substituting Eq. (126), and integrating the resulting equation in z from the edge of the viscous sublayer $z_\tau \equiv \nu/u_\tau$ to the location $L' \sim L/2$ of the maximal wind velocity $\langle u_x(L')\rangle_{t,s_z} = \nu\text{Re}/L$, we obtain

$$\begin{aligned} \text{Re} &\sim \frac{\text{Re}_\tau}{\varkappa \text{Pr}^\zeta} \log\left(\frac{\varkappa}{2} \text{Re}_\tau \text{Pr}^\zeta + 1\right) \\ &\sim \text{Re}_\tau \text{Pr}^{-\zeta} \log \text{Re}_\tau. \end{aligned} \quad (129)$$

Analogously, dividing both sides of Eq. (124) by $\kappa + \kappa_\tau$, substituting Eq. (127) and integrating the resulting equation in z from z_τ to $L/2$, we obtain

$$\text{Nu} \sim \frac{(\varkappa_\theta/2)\text{Re}_\tau \text{Pr}^{\zeta+1}}{\log[(\varkappa_\theta/2)\text{Re}_\tau \text{Pr}^{\zeta+1} + 1]} \sim \frac{\text{Re}_\tau \text{Pr}^{\zeta+1}}{\log \text{Re}_\tau}. \quad (130)$$

In the scaling relations (129) and (130) we have neglected the Pr dependences in the logarithmic corrections following the second tilde.

Finally, we consider $\epsilon_u(z)$. As $\epsilon_u(0) \sim \nu(\partial_z\langle u_x\rangle_{t,s_z}|_{z=0})^2 \sim u_\tau^4/\nu$, the contribution to the mean kinetic energy dissipation rate from the viscous sublayer is smaller than $\epsilon_u(0)z_\tau \sim (u_\tau^4/\nu)\nu/u_\tau = u_\tau^3$. In contrast, the contribution from the core part of the domain is scalingwise larger, as one can see when integrating Eq. (128),

$$\int_{z_\tau}^{L/2} \epsilon_u(z) dz \sim \frac{\varkappa_e u_\tau^3}{\text{Pr}^\zeta} \log(\text{Re}_\tau/2) \gtrsim u_\tau^3 \log \text{Re}_\tau. \quad (131)$$

In the estimate (131) we used the fact that $\text{Pr}^{-\zeta} \geq 1$ for all Prandtl numbers. Since the main contribution to the total kinetic energy dissipation rate ϵ_u comes from the bulk, using Eq. (13) we obtain

$$\frac{2}{L} \int_{z_\tau}^{L/2} \epsilon_u(z) dz \approx \epsilon_u = \frac{\nu^3}{L^4} \text{Ra} \text{Pr}^{-2} (\text{Nu} - 1). \quad (132)$$

From the relations (131) and (132) and $\text{Nu} \sim \text{Nu} - 1$ it follows that

$$\text{Ra} \text{Nu} \text{Pr}^{-2} \sim \text{Re}_\tau^3 \text{Pr}^{-\zeta} \log(\text{Re}_\tau). \quad (133)$$

Combining relations (129), (130), and (133), we obtain

$$\text{Re} \sim \text{Pr}^{-1/2} \text{Ra}^{1/2} \quad \text{for all Pr} \quad (134)$$

and

$$\text{Nu} \sim \frac{\text{Pr}^{2\zeta+1/2} \text{Ra}^{1/2}}{(\log \text{Ra})^2}, \quad (135)$$

with $\zeta = 0$ for $\text{Pr} \lesssim 1$ and $\zeta = -1/2$ for $\text{Pr} \gtrsim 1$. Note that in the scaling relations (134) and (135) we again neglected the Pr

dependences in the logarithmic corrections. Thus, we finally obtain the following scaling relations for the heat transport:

$$\text{Nu} \sim \frac{\text{Pr}^{-1/2} \text{Ra}^{1/2}}{(\log \text{Ra})^2} \quad \text{for } \text{Pr} \gtrsim 1 \text{ (regime IV}'_u), \quad (136)$$

$$\text{Nu} \sim \frac{\text{Pr}^{1/2} \text{Ra}^{1/2}}{(\log \text{Ra})^2} \quad \text{for } \text{Pr} \lesssim 1 \text{ (regime IV}'_\ell). \quad (137)$$

The derived regime IV'_ℓ [the scalings (134) and (137)] is the same as in the model of Grossmann and Lohse (2011). The scaling relations (134) and (136) extend that model toward large Prandtl numbers. The derived regimes are sketched in Fig. 9.

The relation $\text{Nu} \lesssim \text{Pr Re}$ is fulfilled for both regimes IV'_u and IV'_ℓ; cf. relations (30), (134), (136), and (137). The transition between the scaling regimes IV'_u and IV'_ℓ takes place at a constant Pr, where $\text{Nu} \sim \text{Ra}^{1/2}/(\log \text{Ra})^2$ grows slightly slower than $\sim \text{Ra}^{1/2}$ as $\text{Ra} \rightarrow \infty$; see the horizontal line for $\xi = 0$ in the Ra-Pr plane in Fig. 9, which indicates the transition $\text{Pr} \sim \text{Ra}^\xi$ between the neighboring regimes IV'_u and IV'_ℓ. Another boundary for the regime IV'_ℓ is for $\xi = -1$ (marked with a blue line in Fig. 9). While moving along this line for an increasing Ra and $\text{Pr} \sim \text{Ra}^{-1}$, the Nusselt number remains constant, and any steeper transition slope from regime IV'_ℓ would imply an unphysical limit $\text{Nu} \rightarrow 0$

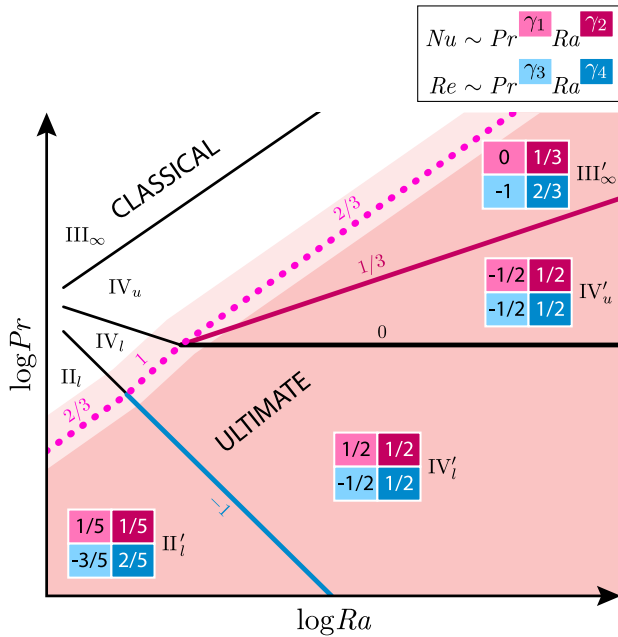


FIG. 9. Sketch of the proposed scaling relations in the ultimate regime of Rayleigh-Bénard convection in the Pr-Ra parameter space, where the ultimate regime is split into the subregimes IV'_u, IV'_ℓ, III'_∞, and II'_ℓ. The numbers in colored boxes show the scaling exponents in the relations $\text{Nu} \sim \text{Pr}^{\gamma_1} \text{Ra}^{\gamma_2}$ and $\text{Re} \sim \text{Pr}^{\gamma_3} \text{Ra}^{\gamma_4}$ (subject to logarithmic corrections). The straight lines indicate the slopes of the transitions between the neighboring regimes $\text{Pr} \sim \text{Ra}^\xi$, where the values of ξ are written next to the lines. The dotted line indicates where the laminar kinetic boundary layer is expected to become turbulent (when the shear Reynolds number achieves a critical value $\text{Re}_s = \text{const}$).

along that line. The blue line in Fig. 9 indicates the slope of the transition to the regime II'_ℓ, which has the same scaling exponents for Nu and Re as the GL regime II_ℓ.

Analogously, one can conclude that the slope of the upper boundary of the regime IV'_u should not be steeper than $\text{Pr} \sim \text{Ra}$ so that along this line the Nusselt number remains constant for increasing Ra. However, as we later explain, the transition from the regime IV'_u has a significantly more gentle slope, namely, $\text{Pr} \sim \text{Ra}^\xi$, with $\xi = 1/3$ (marked with a pink line in Fig. 9).

Indeed, for the no-slip boundary conditions each component u of the velocity field vanishes at the (Lipschitz) boundary of the domain, and therefore the Friedrichs inequality holds,

$$\lambda_1 \langle u^2 \rangle \leq \langle (\nabla u)^2 \rangle, \quad (138)$$

where λ_1 is the lowest positive eigenvalue of the Laplace operator in the considered domain with the corresponding boundary conditions that depends only on the geometrical characteristics and has the dimension of inverse squared length (Shishkina, 2021). Therefore, for any Rayleigh-Bénard flow the following relation should hold:

$$\text{Re}^2 \lesssim (L^4/\nu^3)\epsilon_u = \text{RaPr}^{-2}(\text{Nu} - 1), \quad (139)$$

where Re^2 is based on the kinetic energy $\langle u^2 \rangle$. In the regime IV'_ℓ (for small Pr), the relation (139) is always fulfilled within the discussed boundaries since it then means that $\text{Pr} \lesssim \text{Ra}$. However, in the regime IV'_u, the requirement (139) means that $\text{Pr} \lesssim \text{Ra}^{1/3}$ since it follows from the combination of the relations (134), (136), and (139). Therefore, the regime IV'_u can exist only for $\text{Pr} \lesssim \text{Ra}^{1/3}$. This is consistent with the results of Choffrut, Nobili, and Otto (2016), who derived that the upper bounds for the heat transport for large Prandtl numbers $\text{Pr} \gtrsim \text{Ra}^{1/3}$ cannot exceed $\sim \text{Ra}^{1/3}$ (all up to logarithmic corrections); see Sec. IV.B.2 and Eq. (65) for details.

While moving along the line $\text{Pr} \sim \text{Ra}^{1/3}$ with increasing Ra (the red line in Fig. 9), the Nusselt number effectively scales as $\text{Nu} \sim \text{Pr}^{-1/2} \text{Ra}^{1/2} \sim \text{Ra}^{1/3}$. We assume that this transition line $\text{Pr} \sim \text{Ra}^{1/3}$ connects the regimes IV'_u and III'_∞, where the scaling exponents in the regime III'_∞ are exactly the same as in the classical regime III_∞, namely, $\text{Nu} \sim \text{Pr}^0 \text{Ra}^{1/3}$. This result is again consistent with the findings of Choffrut, Nobili, and Otto (2016).

In summary, Fig. 9 shows the four subregimes of the ultimate regime, namely, III'_∞, IV'_u, IV'_ℓ, and II'_ℓ, which can all be interpreted as ultimate in the sense that one can approach infinite Ra within these regimes. All these subregimes lie to the right of the pink dotted line that indicates a constant Re_s , associated with the onset of a turbulent boundary layer. In the regimes III'_∞ and II'_ℓ the scaling exponent γ in the relation $\text{Nu} \sim \text{Ra}^\gamma$ is, however, smaller than 1/2. The regimes IV'_u and IV'_ℓ can be considered the “true” ultimate regimes in the sense that only there is $\gamma = 1/2$.

The proposed model thus indeed suggests that the scaling exponent $\gamma = 1/2$ in the scaling relation $\text{Nu} \sim \text{Ra}^\gamma$ can be asymptotically achieved within the regimes IV'_u and IV'_ℓ, but only for almost constant Prandtl numbers and logarithmic reductions. As soon as Pr changes as a power law of Ra^ξ

(with some small $|\xi|$; here it does not matter whether ξ is positive or negative), one should expect an asymptotic reduction of the effective scaling exponent as $\gamma = 1/2 - |\xi|/2$.

J. Comparison of the models

We now summarize the assumptions and outcomes of all of the previously discussed models for the ultimate regime. All models use the analytical integral relation (13) between the mean kinetic energy dissipation rate ϵ_u and Ra, Pr, and Nu. Each model is based on three assumptions that allow one to derive the scaling relations for the three unknown quantities: Nu, Re, and Re_τ versus the control parameters Ra and Pr. All discussed models assume that the velocity boundary layers are turbulent, with logarithmic velocity profiles. The other two assumptions, which are needed to close the system of the relations, include the proposed description of the thermal boundary-layer structure and scaling relation for the mean kinetic energy dissipation rate ϵ_u as a function of Re; these two assumptions are different in different models. In Table I, we summarize the assumptions and outcomes for each discussed model, i.e., the proposed scaling relations for the heat and momentum transport.

The assumptions of turbulent thermal and velocity boundary layers seem to be reasonable for the ultimate regime in Rayleigh-Bénard convection, as well as the scaling of the mean kinetic energy dissipation rate, as it should be in sheared wall-bounded turbulent flows. The models by *Chavanne et al. (1997)* and *Grossmann and Lohse (2011)*, which proposed that the Nusselt number in the ultimate regime should scale as $\sim Pr^{1/2} Ra^{1/2}$ subject to different logarithmic corrections, cannot hold for all Pr as $Ra \rightarrow \infty$. This reasoning is dictated by the mathematically strict upper bound $Nu \lesssim Ra^{1/2}$, with a prefactor that is independent of Pr. Indeed, for Prandtl numbers that grow with the Rayleigh number as $Pr \sim Ra^\xi$ with any $\xi > 0$, the relation $Nu \sim Pr^{1/2} Ra^{1/2} \sim Ra^{1/2+\xi/2} > Ra^{1/2}$ would imply the violation of the rigorous upper bound $Nu \lesssim Ra^{1/2}$. Therefore, the scaling relation $Nu \sim Pr^{1/2} Ra^{1/2}$ for $Ra \rightarrow \infty$ might hold only if the Prandtl number is smaller than a certain constant value.

The new model and Kraichnan’s model offer scaling relations for moderate Pr as well. However, in Kraichnan’s model the transition to the regime of high Rayleigh numbers where $Nu \sim Ra^{1/3}$ scales as $Pr \sim Ra^{2/3}$, which contradicts the result of *Choffrut, Nobili, and Otto (2016)* on the bound for the heat transport in large Prandtl number convection. In contrast, the new model suggests the scaling of that transition would be $Pr \sim Ra^{1/3}$, which is consistent with the upper-bound results. This new model can be understood as an extension of the model of *Grossmann and Lohse (2011)* to the case with large Prandtl numbers. In Sec. VII we reconsider different measurements of the Nusselt number at high Rayleigh numbers in light of the proposed model.

VI. RAYLEIGH-BÉNARD CONVECTION UNDER REALISTIC CONDITIONS

Most of the theoretical approaches, from those for the onset of convection (*Chandrasekhar, 1961*) or for weakly nonlinear

TABLE I. Assumptions on the scaling of the mean kinetic energy dissipation rate ϵ_u , Nu, and Re in different models for the ultimate regime, together with the outcomes of these models, i.e., the proposed scaling relations for Nu and Re as functions of the control parameters, which are Ra and Pr.

	Shraiman and Siggia (1990)	Kraichnan (1962)	Chavanne et al. (1997)	Grossmann and Lohse (2011)	Shishkina and Lohse (2024)
$\frac{\epsilon_u}{\nu} \sim$ (assumption)	Re_τ^3 (as an alternative to $\sim Re^3$)	Re^3 (isotropic turbulence)	Re^3 (isotropic turbulence)	$Re_\tau^2 Re$ (wall-bounded turbulence)	$Re_\tau^2 Re$ (wall-bounded turbulence)
$Nu \sim$ (assumption)	$Pr^{-1/3} Re_\tau^{2/3}$ (Prandtl-Blausius BL for $Pr \gg 1$)	$Pr Re_\tau$ ($Pr \leq 0.15$) $Pr^{1/2} Re_\tau$ ($0.15 < Pr \lesssim 1$) (empirical relations)	$\frac{Pr Re_\tau}{\log Re_\tau}$ (turbulent thermal BL)	$\frac{Pr Re_\tau}{\log Re_\tau}$ (turbulent thermal BL)	$\frac{Pr Re_\tau}{\log Re_\tau}$ ($Pr \lesssim 1$); $\frac{Pr^{1/2} Re_\tau}{\log Re_\tau}$ ($Pr \gtrsim 1$) (turbulent thermal BL)
$Re \sim$ (assumption)	$Re_\tau \log Re_\tau$ (turbulent velocity BL)	$Re_\tau \log Re_\tau$ (turbulent velocity BL)	$Re_\tau \log Re_\tau$ (turbulent velocity BL)	$Re_\tau \log Re_\tau$ (turbulent velocity BL)	$Re_\tau \log Re_\tau$ ($Pr \lesssim 1$); $Pr^{1/2} Re_\tau \log Re_\tau$ ($Pr \gtrsim 1$) (turbulent velocity BL)
$Nu \sim$ (outcome)	$Pr^{-1/7} Ra^{2/7}$	$\frac{Pr^{1/2} Ra^{1/2}}{(\log Ra)^{3/2}}$ ($Pr \leq 0.15$) $Pr^{-1/4} Ra^{1/2}$ ($0.15 < Pr \lesssim 1$)	$\frac{Pr^{1/2} Ra^{1/2}}{(\log Ra)^3}$	$\frac{Pr^{1/2} Ra^{1/2}}{(\log Ra)^2}$	$\frac{Pr^{1/2} Ra^{1/2}}{(\log Ra)^2}$ ($Pr \lesssim 1$) $\frac{Pr^{-1/2} Ra^{1/2}}{(\log Ra)^2}$ ($Pr \gtrsim 1$) $Pr^{-1/2} Ra^{1/2}$
$Re \sim$ (outcome)	$\frac{Ra^{3/7} \log Ra}{Pr^{5/7}}$	$\frac{Pr^{-1/2} Ra^{1/2}}{(\log Ra)^{1/2}}$ ($Pr \leq 0.15$) $\frac{Pr^{-3/4} Ra^{1/2}}{(\log Ra)^{1/2}}$ ($0.15 < Pr \lesssim 1$)	$\frac{Pr^{-1/2} Ra^{1/2}}{\log Ra}$	$Pr^{-1/2} Ra^{1/2}$	

or oscillatory regimes (Schlueter, Lortz, and Busse, 1965; Busse, 1967) to the models for the ultimate regime, that we discussed in Secs. IV and V consider the convective system as infinitely extended in the lateral directions, i.e., with an aspect ratio of $\Gamma = \infty$. Moreover, they assume perfect Oberbeck-Boussinesq conditions according to the equations given in Sec. II and perfect thermal boundary conditions, meaning infinite thermal conductivity of the upper and lower plates, which are assumed to be perfectly smooth. Sidewalls are absent in such idealized systems.

In laboratory Rayleigh-Bénard experiments, all of these idealized conditions cannot be realized: Unavoidably, real systems have a finite aspect ratio and thus also sidewalls, which do affect the flow. Moreover, the plates have thermal and mechanical imperfections that affect the flow boundary conditions, and the conditions and fluid properties are not perfectly Oberbeck-Boussinesq conditions, i.e., they are non-Oberbeck-Boussinesq (NOB) conditions, which does affect the heat transfer. In this section we discuss all of these imperfections and their possible effect on the heat transfer and flow organization.

A. The influence of the container's aspect ratio

In any laboratory RB experiment, the container is confined and its aspect ratio Γ can play an important role (Wu and Libchaber, 1992; Roche *et al.*, 2010; Roche, 2020; Shishkina, 2021; Ahlers *et al.*, 2022), particularly for small Γ . As discussed in Sec. III, in GL theory this is reflected in a Γ dependence of the four prefactors c_i and the prefactor a , which becomes relevant for small Γ .

The stabilizing effect of small Γ on the flow can already be seen in the Γ dependence of the critical Rayleigh number $Ra_{c,\Gamma}$ for the onset of convection, which can be estimated as (Shishkina, 2021)

$$Ra_{c,\Gamma} \sim Ra_{c,\infty}(1 + c_u\Gamma^{-2})(1 + c_\theta\Gamma^{-2}), \quad (140)$$

with positive constants c_u and c_θ that depend on the container shape and the sidewall boundary conditions for the velocity and temperature, respectively. In relation (140) $Ra_{c,\infty} \approx 1708$ is the well-known onset of convection rolls for $\Gamma = \infty$ following from linear stability analysis (Chandrasekhar, 1961). In scaling (140) one can see that $Ra_{c,\Gamma} \sim \Gamma^{-4}$ for small $\Gamma \ll 1$. For a given diameter of the plates $D \ll L$ and a given temperature difference between them, the Rayleigh number will grow as $\sim \Gamma^{-3}$ with increasing height of the container (or, in other words, with decreasing Γ), while the Rayleigh number for the onset of convection will grow much faster, as $Ra_{c,\Gamma} \sim \Gamma^{-4}$, which implies that at a certain sufficiently small Γ the convective fluid motion will be fully suppressed. Therefore, a large value of Ra does not mean in itself turbulence and does not even guarantee fluid motion inside the container if Γ is too small (Shishkina, 2021). Zhang and Xia (2023) and Ren *et al.* (2024) experimentally confirmed that the theoretical result $Ra_{c,\Gamma} \sim \Gamma^{-4}$ holds as expected for $\Gamma \rightarrow 0$ and found that the Ra range between the onset of convection and the onset of turbulence shrinks.

Given that for small Γ even the onset of convection is strongly shifted toward larger Rayleigh numbers, the onset

Ra^* of the transition to the ultimate regime also increases for finite Γ ; i.e., the turbulent flow is stabilized from the sidewalls. How does one quantitatively estimate the stabilizing effect of the sidewalls on the onset of the ultimate regime? From an analysis of the transition from the small- Γ regime to the large Γ regime, Shishkina (2021) and Ahlers *et al.* (2022) derived

$$\ell = D/\sqrt{\Gamma^2 + c_u} = L/\sqrt{1 + c_u/\Gamma^2} \quad (141)$$

as the relevant length scale for the transition, with $c_u \approx 1.49$ for a cylindrical container. $\ell(\Gamma)$ shows a crossover from $\ell = L$ for large Γ to $\ell = D$ for small Γ . For this reason, they suggested that the Γ dependence at the onset of the ultimate regimes is

$$Ra^* \approx Ra_{\infty}^*(1 + c_u/\Gamma^2)^{3/2}. \quad (142)$$

Compare Eq. (142) to Fig. 10, where the theoretical curve is compared with the experimental observations. In Eq. (142) Ra_{∞}^* is the Rayleigh number associated with the onset of the ultimate regime in an infinite fluid layer ($\Gamma = \infty$).

For small $\Gamma \ll 1$, Eq. (142) simplifies to $Ra^* \sim \Gamma^{-3}$, a relation suggested by Roche *et al.* (2010) based on an analysis of the Grenoble data, and by Roche (2020) based on different experimental data (Chavanne *et al.*, 1997, 2001; Niemela, Skrbek, Sreenivasan, and Donnelly, 2000; Niemela and Sreenivasan, 2003a, 2006b; Roche *et al.*, 2010; Ahlers, He *et al.*, 2012; He, Funfschilling, Nobach *et al.*, 2012; He, Funfschilling, Bodenschatz, and Ahlers, 2012; He *et al.*, 2013). The scaling of the transition of about Γ^{-3} in the Göttingen data was first reported by Bodenschatz *et al.* (2015). For large $\Gamma \gg 1$ the onset Ra^* of the ultimate regime becomes independent of Γ , as then only the height L of the container is the relevant length scale, as reflected in Eq. (142). Indeed, this is what was obtained in the analysis by Roche (2020) of various datasets for different Γ . Roche (2020) also proposed a crossover from a Γ^{-3} scaling of the transition to the ultimate regime for $\Gamma \lesssim 2$ to Γ independence for $\Gamma \gtrsim 3$; cf. Fig. 10.

The suggested Γ dependence of the onset of the ultimate regime (142) can be tested more generally by correspondingly replotting the experimental $Nu(Ra)$ data for various Γ : Indeed, a collapse of the onset value for a given dataset with various Γ is achieved this way; see Fig. 11. More concretely, when plotted that way all Göttingen data for various Γ collapse, as do all Grenoble data for various Γ (however, with different Ra_{∞}^*).

The collapse of the curves for different aspect ratios Γ in Fig. 11(b) implies that upon knowing $Nu(Ra, Pr)$ for one particular aspect ratio Γ_1 the dependences for all other aspect ratios Γ follow. In particular, within the framework of GL theory this implies that from the four prefactors c_i , $i = 1, 2, 3, 4$ for one particular aspect ratio (say, $\Gamma_1 = 1$), one can calculate the prefactors for all other aspect ratios Γ .

We note that not only the aspect ratio of the container but also its shape affect the heat transfer and the overall flow organization (Shishkina, 2021). Daya and Ecke (2001) compared RB convection in a cylindrical container and in a cubic container, finding major differences, but as their experiments were done in the classical regime, far away from the ultimate regime, we do not discuss them here. But, clearly, the shape of

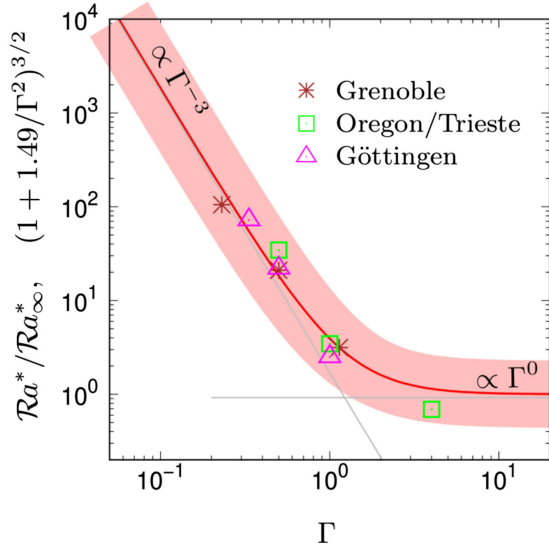


FIG. 10. Relative increase $(1 + 1.49/\Gamma^2)^{3/2}$ of the critical Rayleigh number Ra^* for the transition to the ultimate regime in a cylindrical container compared to the $\Gamma \rightarrow \infty$ case, according to the theory of Shishkina (2021) and Ahlers *et al.* (2022); cf. Eq. (142) (solid red line). The transitional Rayleigh number Ra^* should scale as $\propto \Gamma^{-3}$ for small Γ and as $\propto \Gamma^0$ for large Γ . Roche (2020) proposed a crossover from the $\sim \Gamma^{-3}$ dependence for $\Gamma \lesssim 2$ to Γ independence for $\Gamma \gtrsim 3$. The shaded red region symbolizes the range in which the transition to the ultimate regime could occur according to the non-normal–nonlinear picture. Symbols: The onset Rayleigh number Ra^* for the increase of the effective scaling exponent γ in the relation $Nu \sim Ra^\gamma$ as a function of the cylindrical container aspect ratio Γ , as found in various experimental data. The vertical offset Ra_∞^* represents the Rayleigh number for the onset of the ultimate regime in an infinite fluid layer ($\Gamma = \infty$); it is different for the three datasets. For the Grenoble and Göttingen datasets the right-end values of the determined transition (i.e., Ra_2^* from Table II in Sec. VII) are plotted. For the Oregon dataset the transitional Rayleigh number was not claimed by Niemela, Skrbek, Sreenivasan, and Donnelly (2000) but was proposed by Roche (2020).

the container will affect when the turbulent flow undergoes the transition to the ultimate regime.

B. From the idealized fluid to real fluids: Non-Oberbeck-Boussinesq effects

Material properties of any real fluid depend on the temperature and pressure. These dependences are not taken into account within the Oberbeck-Boussinesq approximation. They can cause the so-called non-Oberbeck-Boussinesq effects (NOB effects), which can imply significant deviations in the heat and momentum transport and/or global flow structures from what is predicted by the Oberbeck-Boussinesq equations.

The validity of the OB approximation in thermal convection was investigated in several theoretical studies, also in terms of orders of magnitude of particular terms in the governing equations; see Spiegel and Veronis (1960) and Veronis (1962). A mathematically rigorous variational approach in which expansions of the fluid properties as power series were considered was first applied by Mihaljan (1962), who,

however, considered only a temperature variation of the density. Later the method was extended to take the temperature dependences of other fluid parameters into account.

When going beyond the OB approximation, at first order one can consider a linear dependence of the five material properties of the fluid $\varphi = \rho, \mu, c_p, \alpha,$ and k (i.e., the density, absolute viscosity, specific heat at constant pressure, thermal expansion coefficient, and thermal conductivity, respectively) on the temperature and pressure,

$$\frac{\varphi}{\varphi_0} = 1 + \varepsilon_{\varphi,T} \frac{T - T_0}{\Delta} + \varepsilon_{\varphi,P} \frac{P - P_0}{\rho_0 g L}. \quad (143)$$

This implies that there are ten different sources for the NOB effects (non-Oberbeck-Boussinesq-ness, or NOB-ness), expressed in the ten dimensionless factors $\varepsilon_{\varphi,T}$ and $\varepsilon_{\varphi,P}$, with $\varphi = \rho, \mu, c_p, \alpha,$ and k ; see Gray and Giorgini (1976). For a certain fluid and a certain reference temperature T_0 and pressure P_0 of operation, it is *a priori* not clear which of these ten dimensionless parameters $\varepsilon_{\varphi,T}$ and $\varepsilon_{\varphi,P}$ are the most relevant ones to cause the NOB-ness of the experiment. Thus, every experiment requires an *a priori* characterization and estimate of its NOB-ness that can manifest in ten different ways, and often in several different ways simultaneously. To disentangle the various NOB effects, direct numerical simulations in which one can employ artificial fluids that display only one type of NOB-ness can be helpful. An example for such an analysis for ethane was provided by Ahlers *et al.* (2008). There have been further investigations of the NOB effects in Rayleigh-Bénard convection in helium and pressurized SF₆ (Roche *et al.*, 2010; Shishkina, Weiss, and Bodenschatz, 2016; Weiss *et al.*, 2018; Yik, Valori, and Weiss, 2020) and in water and glycerol (Manga and Weeraratne, 1999; Ahlers *et al.*, 2006; Sugiyama *et al.*, 2009; Horn, Shishkina, and Wagner, 2013; Horn and Shishkina, 2014). In several studies only the temperature variation of the density ($\alpha\Delta$) is considered as a measure of NOB-ness (Niemela and Sreenivasan, 2003a); however, this is only one ($\varepsilon_{\rho,T}$) of the many parameters ($\varepsilon_{\varphi,T}$) to be monitored as a possible source of NOB-ness. Usually the pressure variation has only a negligible effect on NOB-ness; the temperature variation plays a much more important role. Here we restrict ourselves to the lowest order and consider only a linear term in the temperature expansion [as in Eq. (143)] to capture the NOB effects. This is sufficient, as shown in a recent study by Macek *et al.* (2023) for the case of cryogenic helium.

Gray and Giorgini (1976) first went beyond the OB approximation in a comprehensive way, and we now recall their results; for a further discussion of the NOB effects, see Appendix A2 of Roche *et al.* (2010). The starting point is the set of the governing equations for a Newtonian fluid of variable properties with zero second viscosity (Batchelor, 1967),

$$D_t \rho + \rho \nabla \cdot \mathbf{u} = 0, \quad (144)$$

$$\rho D_t \mathbf{u} + \nabla P = \nabla \cdot (\mu \mathbf{S}_{ij}) - \rho g \mathbf{e}_z, \quad (145)$$

$$\rho c_p D_t T = \nabla \cdot (k \nabla T) + \alpha T D_t P + \mu \Phi, \quad (146)$$

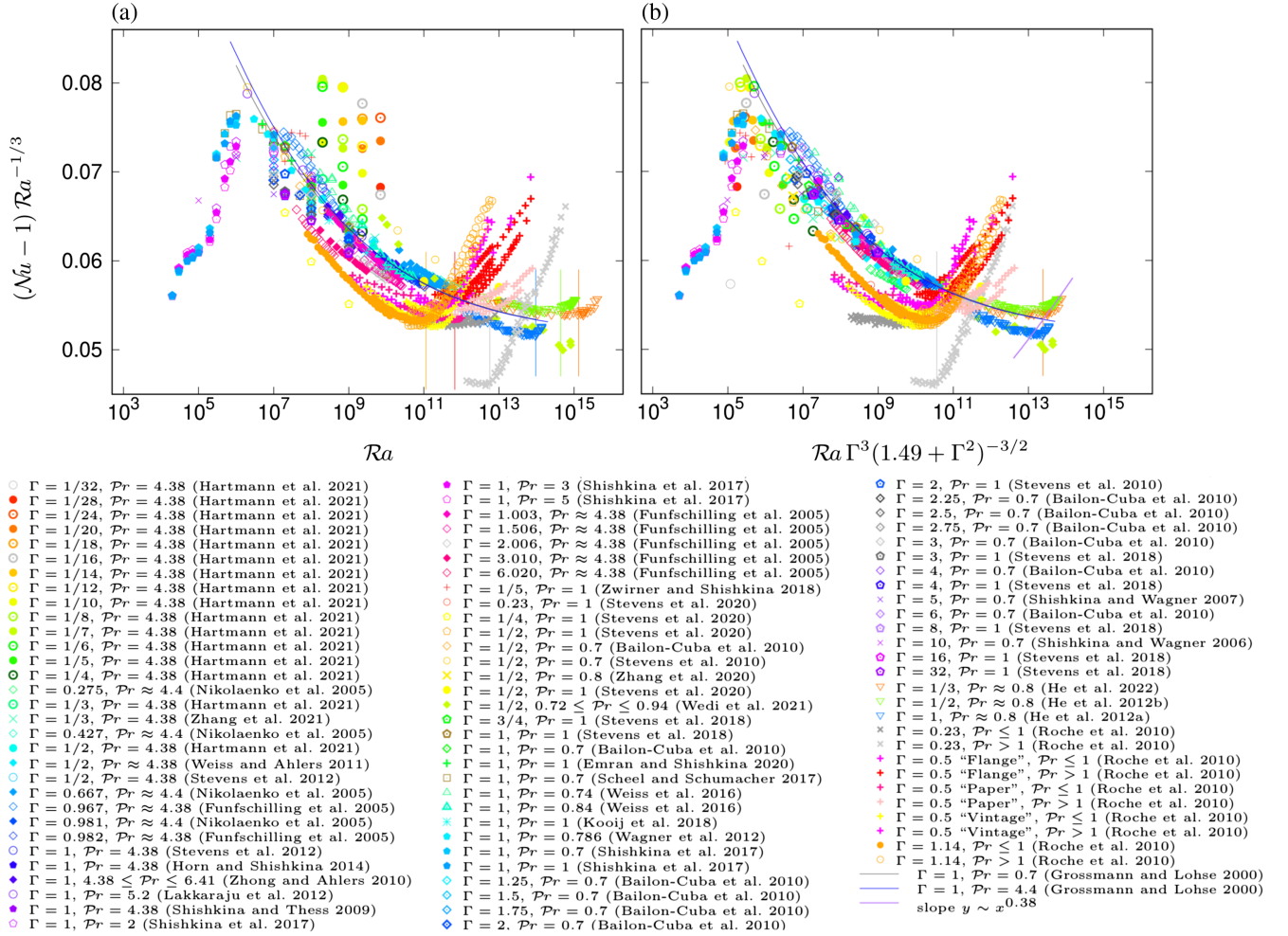


FIG. 11. (a) Nusselt number, compensated with $Ra^{1/3}$ vs Ra , for Prandtl numbers as appropriate for air and water at room temperature ($0.7 \leq Pr \leq 6$) for various aspect ratios Γ . Vertical lines correspond to the locations where the plots have a visible minimum (start of growth of the effective scaling exponent γ above $1/3$ in the scaling relation $Nu \sim Ra^\gamma$) in Göttingen measurements (short lines) and Grenoble measurements (long lines) for different aspect ratios. (b) Same as (a), but for Rayleigh numbers based on the relevant length scale [Eq. (142)]. All vertical lines are different in (a), while the Göttingen lines and the Grenoble lines collapse in (b). The inclined straight lines show the slope $\gamma \sim x^{0.38}$, while the upper (lower) curves correspond to the predictions of Grossmann and Lohse (2000) for $\Gamma = 1$ and $Pr = 4.4$ ($Pr = 0.7$). The references in the legend refer to Funfschilling *et al.* (2005), Nikolaenko *et al.* (2005), Shishkina and Wagner (2006, 2007), Shishkina and Thess (2009), Bailon-Cuba, Emran, and Schumacher (2010), Roche *et al.* (2010), Stevens, Clercx, and Lohse (2010a, 2010b), Zhong and Ahlers (2010), Weiss and Ahlers (2011), Ahlers, He *et al.* (2012), He, Funfschilling, Bodenschatz, and Ahlers (2012), He, Funfschilling, Nobach *et al.* (2012), Lakkaraju *et al.* (2012), Stevens *et al.* (2012), Wagner, Shishkina, and Wagner (2012), Horn and Shishkina (2014), Weiss, Wei, and Ahlers (2016), Scheel and Schumacher (2017), Shishkina, Emran *et al.* (2017), Kooij *et al.* (2018), Stevens *et al.* (2018), Zwirner and Shishkina (2018), Emran and Shishkina (2020), Stevens, Lohse, and Verzicco (2020), Zhang *et al.* (2020), Hartmann *et al.* (2021), Wedi *et al.* (2021), Zhang, Ecke, and Shishkina (2021), and He, Bodenschatz, and Ahlers (2022). Adapted from Shishkina, 2021, and Ahlers *et al.*, 2022.

where $P = p - \rho_0 g z e_z$ is the full pressure, $S_{ij} \equiv \partial_j u_i + \partial_i u_j - (2\delta_{ij}/3)\partial_k u_k$ is the deformation rate tensor, $\Phi \equiv (S_{ij}/2)(\partial_j u_i + \partial_i u_j)$ is the viscous dissipation function, $D_t \equiv \partial_t + \mathbf{u} \cdot \nabla$ denotes the full material derivative, and δ_{ij} represents the Kronecker symbol. The reference temperature and pressure for the system are denoted as T_0 and P_0 , respectively, and the corresponding fluid properties at the reference T_0 and P_0 in the following are also marked with a subscript 0.

It is further assumed that any fluid property φ that is involved in Eqs. (144)–(146) can be represented as a linear function of T and P according to Eq. (143). Substituting the

representations (143) of the fluid properties $\varphi = \rho, \mu, c_p, \alpha$, and k into Eqs. (144)–(146), one requires that the residuals, i.e., the terms that distinguish the resulting equations from their Oberbeck-Boussinesq approximation, to be negligibly small. The OB requirements are fulfilled if not only all $\varepsilon_{\varphi,T}$ and $\varepsilon_{\varphi,P}$ but also the magnitudes of the pressure work term ($\alpha T D_t P$) and the dissipation term ($\mu \Phi$) in Eq. (146) are negligibly small compared to the magnitudes of the other terms in Eq. (146). Comparing $\rho c_p D_t T$ with $\alpha T D_t P$ in Eq. (146), one concludes that the pressure work term is negligible if the following relation is fulfilled: $\rho_0 c_{p,0} \Delta \gg \alpha_0 T_0 \rho_0 g L$ (here we estimate the pressure

magnitude as $P \sim \rho_0 g L$, the magnitude of the temperature variation as Δ , and the magnitude of the absolute value of the temperature as T_0). Comparing $\nabla \cdot (k \nabla T)$ with $\mu \Phi$, one concludes that the dissipation term is negligible if $k_0 \Delta \gg \mu_0 \alpha_0 g \Delta L$ (here we estimate the velocity magnitude as the free-fall velocity $\sqrt{\alpha_0 g L \Delta}$). The last two inequalities can be reformulated as $b T_0 / \Delta \ll 1$ and $b \text{Pr}_0 \ll 1$, respectively, where $\text{Pr}_0 \equiv \nu_0 / \kappa_0$ is the reference Prandtl number, $\kappa_0 \equiv k_0 / (\rho_0 c_{p,0})$ is the reference thermal diffusivity, and $b \equiv \alpha_0 g L / c_{p,0}$.

We introduce a certain small threshold $\hat{\sigma}$, $0 < \hat{\sigma} \ll 1$, and define the OB approximation as valid with the accuracy $\hat{\sigma}$ if the following requirements are fulfilled (Weiss, Emran, and Shishkina, 2024):

$$\varepsilon_{\varphi,T} \ll \hat{\sigma}, \quad \varepsilon_{\varphi,P} \ll \hat{\sigma} \quad \text{for } \varphi = \rho, \mu, c_p, k, \quad (147)$$

$$b T_0 / \Delta \ll \hat{\sigma}, \quad b \text{Pr}_0 \ll \hat{\sigma}. \quad (148)$$

The parameter $\hat{\sigma}$ can be interpreted as a measure of the NOB-ness. Note that the requirements (147) and (148) can be derived by substituting Eq. (143) for all fluid properties into Eqs. (144)–(146) and requiring the terms that are not present in the OB approximation to become negligibly small as $\hat{\sigma} \rightarrow 0$.

Thus, for any given fluid and any given small threshold $\hat{\sigma}$ for the residuals, from the OB assumptions [(i) and (ii) in Sec. II.A] one can derive the region of the OB validity in terms of the upper bounds for the maximal possible temperature difference Δ of the system and the maximal possible size L of the container. The OB-validity region for any common fluid is sketched in Fig. 12. For any reasonable threshold, the OB-validity region (in terms of Δ and L) is bounded from above and below: this gives restrictions to the Rayleigh numbers, which can be achieved in almost-OB experiments (Gray and Giorgini, 1976; Horn and Shishkina, 2014; Weiss *et al.*, 2018). In particular, this means that for any chosen

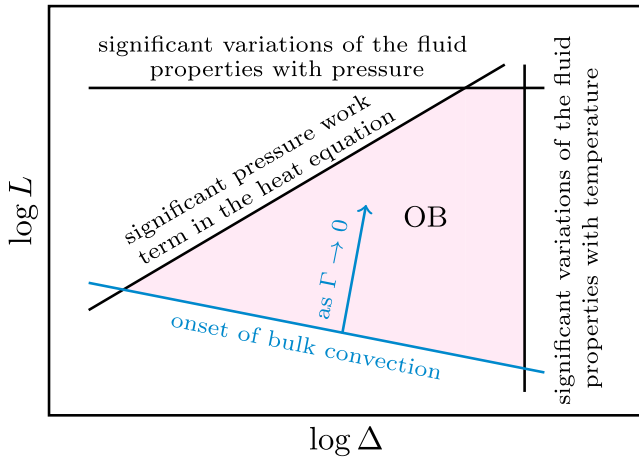


FIG. 12. Region of the validity of the Oberbeck-Boussinesq approximation in thermal convection for a given fluid sketched in terms of the maximal possible temperature difference Δ of the system and the maximal possible container height L ; see Gray and Giorgini (1976) and Ecke and Shishkina (2023).

fluid and any chosen threshold on the degree of NOB-ness (parameter $\hat{\sigma}$), Ra larger than a certain maximum value $\text{Ra}_{\text{max},\hat{\sigma}}$ can in principle not be realized.

In Fig. 13 the regions where the OB approximation is valid are presented for some fluids and operational conditions that are typically employed in thermal convection experiments, namely, water, air, ethane, helium, pressurized gas sulfur hexafluoride (SF_6) at near room temperature, and cryogenic helium. For any considered fluid and given reference temperature T_0 and reference pressure P_0 , these regions are calculated in terms of the maximum temperature difference Δ and the container height L . These regions depend on the threshold $\hat{\sigma}$; the choices $\hat{\sigma} = 5\%$, 10% , and 20% give the embedded domains of the OB approximation validity; they are displayed in green, blue, and red, respectively, in Fig. 13. The values that correspond to the upper right corners of each domain determine the maximum achievable Rayleigh numbers $\text{Ra}_{\text{max},\hat{\sigma}}$, which are indicated in Fig. 13 with the corresponding colors.

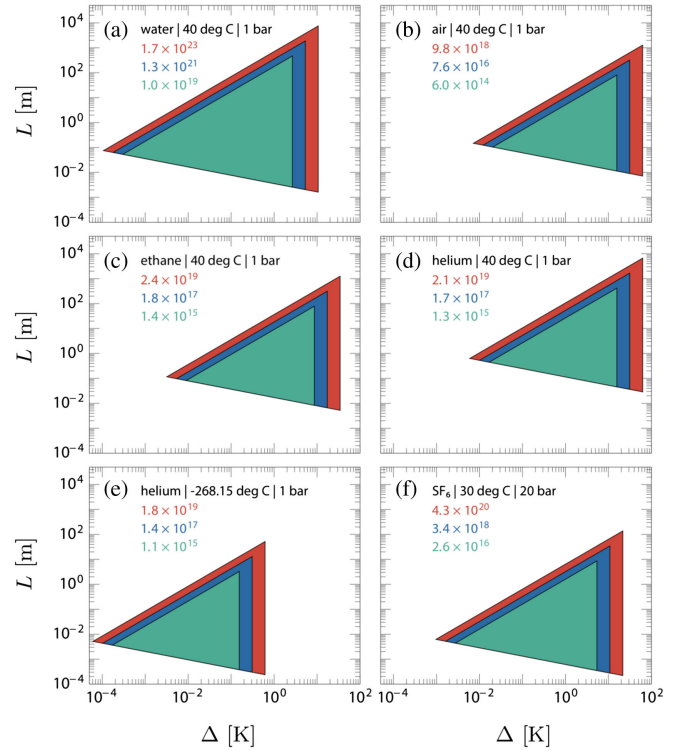


FIG. 13. Regions of the validity of the Oberbeck-Boussinesq approximation in terms of the maximum temperature difference Δ and the container height L according to Eqs. (147) and (148) for different fluids: (a) water at $T_0 = 40^\circ\text{C}$ and $P_0 = 1$ bar, (b) air at $T_0 = 40^\circ\text{C}$ and $P_0 = 1$ bar, (c) ethane at $T_0 = 40^\circ\text{C}$ and $P_0 = 1$ bar, (d) helium at $T_0 = 40^\circ\text{C}$ and $P_0 = 1$ bar, (e) helium at $T_0 = -268.15^\circ\text{C} = 5$ K and $P_0 = 1$ bar, and (f) SF_6 at $T_0 = 30^\circ\text{C}$ and $P_0 = 20$ bar. The nested green (smallest), blue, and red (largest) OB-validity regions correspond to the thresholds on the degree of NOB-ness $\hat{\sigma} = 0.05, 0.1$, and 0.2 , respectively. The corresponding maximum achievable Rayleigh numbers $\text{Ra}_{\text{max},\hat{\sigma}}$ are given in the respective colors (from bottom to top). Calculations are made using data from the National Institute of Standards and Technology (2013). Adapted from Weiss, Emran, and Shishkina, 2024.

From the comparison of the values of $Ra_{\max, \delta}$ for the considered fluids, one might conclude that water is the optimal fluid to study RB convections under OB conditions at extreme Ra since it has the largest $Ra_{\max, \delta}$. However, be aware that these extremely large Ra can be obtained only when the depth of the water layer is at least hundreds of meters. In this regard, the use of cryogenic helium and pressurized gas SF_6 is preferable for experimental studies of the transition to the ultimate regime.

C. From the idealized container to real containers: Small roughness and finite conductivity of the plates and sidewalls of the container

Further sources of possible differences between the heat and momentum characteristics of real convective flows and the corresponding characteristics obtained as solutions of the Oberbeck-Boussinesq equations (1)–(3) for the same control parameters are imperfections of the container in the sense that no real-experiment container can perfectly satisfy the idealized boundary conditions at the sidewalls and the plates. In addition, the surfaces of the containers are never perfectly smooth: they are always more or less rough. These container imperfections can be formally interpreted as a slight change of the boundary conditions at the horizontal or vertical surface in the convective system or as a slight change of the container shape due to the wall roughness. All of this can influence the response characteristics of the system like Re and Nu and, in particular, the onset of the transition to ultimate turbulence. In fact, dedicated containers have been built to study the effect of the plate roughness; then the roughness is controlled and considerable. These experiments are discussed in Sec. IX.C; see also Kaiser, Salort, and Roche (2011).

In addition, the imposed thermal boundary conditions at the sidewalls can substantially affect the heat transport in the system (Ahlers, 2000; Roche, Castaing, Chabaud, Hébral, and Sommeria, 2001; Stevens, Lohse, and Verzicco, 2014; Roche, 2020; Reiter, Zhang, and Shishkina, 2022) and the emergence of different flow states. Ideal sidewalls have adiabatic conditions. In reality, sidewalls can never be perfectly adiabatic but will be partially conducting, which is known to delay the onset of convection as compared to the adiabatic case (Buell and Catton, 1983; Puigjaner *et al.*, 2004, 2008; Hebert *et al.*, 2010). Sidewalls are also known to influence pattern formation (Cross and Hohenberg, 1993; de Bruyn *et al.*, 1996; Bodenschatz, Pesch, and Ahlers, 2000), so different sidewall boundary conditions can lead to different observed patterns even if the aspect ratio of the employed container is large (Hu, Ecke, and Ahlers, 1993).

But what about the effect of sidewalls in the turbulent case? In that case, nonperfectly adiabatic sidewalls imply unwanted outward or inward sidewall heat flux that can significantly bias global heat transport measurements and also the measured effective scaling exponent γ in the effective scaling relation $Nu \sim Ra^\gamma$ (Ahlers, 2000; Roche, Castaing, Chabaud, and Hébral, 2001; Roche *et al.*, 2010; Reiter, Zhang, and Shishkina, 2022).

As stated, in laboratory experiments the boundary conditions at the sidewalls are always a mixture of adiabatic and conducting sidewalls. To explore the influence of a finite

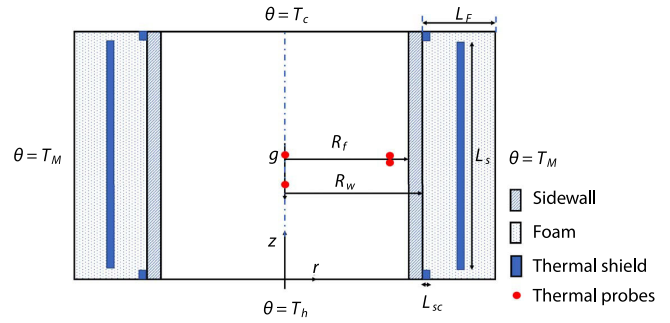


FIG. 14. Sketch of a numerical setup with sidewall, insulation layer, and thermal side shields, for which Wan *et al.* (2019) performed DNS, including all sidewalls, foam, and thermal shields. The aspect ratio of the fluid domain $\Gamma = 1$. The Plexiglass sidewall has a thickness $R_w - R_f = L/30$. The insulation layer has a thickness $L_F = 0.2L$. For the inner thermal side shields $L_{sc} = 0.015L$ with a square cross section. The outer thermal shield has a thickness of $0.02L$ and a height $L_s = 0.96L$, and its inner edge is located at $0.6L$ from the cylinder axis. The outer surface of the insulation layer is assumed to be isothermal at the arithmetic mean of the top (T_c) and bottom (T_h) temperatures $\theta = T_M \equiv (T_c + T_h)/2$. Adapted from Wan *et al.*, 2019.

thermal conductivity of the sidewalls, Verzicco (2002), Stevens, Lohse, and Verzicco (2014), and Reiter, Zhang, and Shishkina (2022) conducted numerical simulations where thermal conduction of the solid sidewalls was incorporated. Wan *et al.* (2019) simulated the full sidewalls with all their imperfections, such as finite heat conductivity, insulation by foam, and thermal shields; see Fig. 14. The numerical simulations showed that different thermal properties of the sidewall can alter the mean flow structure, leading to significant differences in the global heat transport if the considered Rayleigh numbers are relatively low. With increasing Ra , this effect is gradually reduced and becomes negligible, but only if the averaged sidewall temperature is kept constant and maintained at the arithmetic mean of the top and bottom plate temperatures.

If the mean sidewall temperature deviates from this arithmetic mean, the differences in the heat transport can persist even for large Rayleigh numbers (Stevens, Lohse, and Verzicco, 2014). Therefore, it is important to keep the mean temperature of the sidewalls at the arithmetic mean of the top and bottom temperatures. Probably the most reliable and easiest way to achieve this is to maintain the entire environment of the experimental facility at that temperature.

We now come to the plate effects. For the ideal case discussed in Sec. II, the thermal conductivity of the plate is infinite. In real experiments, however, the top and bottom plates have finite conductivity. The thermal plumes that detach from the heated or cooled plate alter the instantaneous temperature distributions at the plates, taking heat out of the plates, which for finite heat conductivity cannot instantaneously replenish (Ahlers and Xu, 2001; Chaumat, Castaing, and Chillà, 2002; Chillà *et al.*, 2004b). Therefore, the isothermal boundary conditions at the plates ($T = T_-$ at the top and $T = T_+$ at the bottom) are fulfilled in the best case only for the time- and area-averaged temperatures. The finite conductivity of the top and bottom plates can influence the

flow structure and may cause deviations of the measured heat transport in laboratory experiments from the heat transport in the perfect OB RB system for the same control parameters. The effect becomes worse for increasing Nusselt numbers and thus increasing Ra, as more heat is then taken out of the plates. [Verzicco \(2004\)](#) analyzed this effect and introduced a correction scheme that has been widely used, sometimes in modified forms. In this review we refer to various experimental papers that explained exactly how this is done.

D. Instrumentation in the container

Further deviations from the ideal conditions described in Sec. II are caused by instrumentation within the container, such as thermal probes in the thermal BLs at the plates or the kinetic BLs at the plates or sidewalls. In various experiments these probes were used to monitor the flow and to identify the dynamics of the large-scale convection roll; see [Chavanne et al. \(1997, 2001\)](#) and [Roche et al. \(2010\)](#). However, such probes can also trigger non-normal–nonlinear instabilities in the shear flow, as disturbances do in pipe flow ([Avila, Barkley, and Hof, 2023](#)). The consequences of the disturbance significantly depend on the exact position of the probe, its size, etc. In general, one would expect the absence of probes and any other instrumentation in the container to delay the transition to the ultimate regime. Indeed, [He, Funfschilling, Bodenschatz, and Ahlers \(2012\)](#) and [He, Funfschilling, Nobach et al. \(2012\)](#), who did not put any instrumentation in the container itself, found the transition to the ultimate regime later than [Chavanne et al. \(1997, 2001\)](#), who had thermal probes in the container. In fact, [Chavanne et al. \(2001\)](#) used these probes to show the transition from a laminar BL to a turbulent one.

The only way to use thermal probes and not affect the flow itself is to fully immerse them in the plates or in the sidewalls, and to make sure that on the inside side the plate or the wall at the position of the probe is perfectly smooth. This route was followed by the Göttingen group ([Ahlers, He et al., 2012](#); [Ahlers, Bodenschatz, and He, 2014](#)). Note that this usage of thermal probes works only under nonideal thermal boundary conditions; under ideal conditions the thermal fluctuations inside the container should not be reflected inside the sidewalls or the plates; see Sec. VI.C.

VII. LARGE RAYLEIGH NUMBER EXPERIMENTS

From the definition of the Rayleigh number [Eq. (4)], it is clear that in controlled convection experiments in principle there are three ways to increase Ra: to perform experiments in containers (i) with a large height L , (ii) with a large temperature difference Δ , and (iii) with appropriate material parameters of the fluid, i.e., a small kinematic viscosity ν , a thermal diffusivity κ , and a large thermal expansion coefficient α . Option (iii) can be realized by approaching the critical point of the fluid. However, in Sec. VI.B we saw that there are serious and unavoidable limitations with all three ways, in practice and in principle, if the Oberbeck-Boussinesq character of the flow is to be preserved. In addition, there are cost considerations and limitations. For example, even with an $L = 7$ m high cylinder (with $\Gamma = 1.23$) and air as a fluid ($\text{Pr} = 0.7$), [du Puits, Resagk, and Thess \(2007\)](#) and [du Puits et al. \(2007\)](#)

achieved “only” $\text{Ra} \approx 10^{12}$. In addition, for these large-scale experiments the thermal insulation of the sidewalls and constant temperature boundary conditions at the plates are major challenges, to a degree, in fact, that no meaningful global heat flux measurements were possible in these experiments. Owing to all of these limitations, all three ways must be combined to achieve the largest possible Ra, which is required for experimentally exploring the ultimate regime.

A. Chicago group

The first group to seriously explore large Ra RB convection by working with gases in the vicinity of their critical points where ν and κ are small was Albert Libchaber’s group at the University of Chicago ([Heslot, Castaing, and Libchaber, 1987](#); [Castaing et al., 1989](#); [Sano, Wu, and Libchaber, 1989](#); [Wu et al., 1990](#); [Procaccia et al., 1991](#); [Wu and Libchaber, 1992](#)), whose work was based on a prior idea and previous experiments conducted by [Threlfall \(1975\)](#). While Threlfall with his $L \approx 2$ cm high container and helium gas achieved only $\text{Ra} = 2 \times 10^9$, [Heslot, Castaing, and Libchaber \(1987\)](#) achieved $\text{Ra} = 10^{11}$ with their $L = 8.7$ cm high container, [Sano, Wu, and Libchaber \(1989\)](#) attained $\text{Ra} = 10^{12}$ with the same container, [Castaing et al. \(1989\)](#) achieved $\text{Ra} = 6 \times 10^{12}$, again with the same container, and [Wu et al. \(1990\)](#) and [Procaccia et al. \(1991\)](#) attained $\text{Ra} = 4 \times 10^{14}$ with their $L = 40$ cm high container. They reported an effective scaling law $\text{Nu} \sim \text{Ra}^\gamma$ with $\gamma \approx 0.29 \pm 0.005$ ([Heslot, Castaing, and Libchaber, 1987](#), [Castaing et al., 1989](#)) or, similarly, $\gamma = 0.286 \pm 0.003$ ([Wu and Libchaber, 1992](#)) up to their largest Ra. Libchaber’s group did not find hints of any transitions in the Nusselt number toward larger scaling exponents, even at their largest Ra. Note that the high-frequency transition reported in the temperature spectra in these experiments and derivatives of these temperature spectra ([Procaccia et al., 1991](#)) could consistently be accounted for as an effect of the thermal probe that, at high frequencies and large Ra, cannot follow the local thermal fluctuations ([Grossmann and Lohse, 1993](#)); this transition has nothing to do with a flow transition to the ultimate regime.

Though the Chicago experiments by Libchaber’s group did not find any evidence for the ultimate regime, their papers had a huge impact in defining the problem. At the end of their paper, [Castaing et al. \(1989\)](#) recollected, “[Kraichnan \(1962\)](#) predicts a new behavior appearing between $\text{Ra} = 10^{18}$ and $\text{Ra} = 10^{24}$ ” and wrote, “We do not know. Perhaps the hard turbulence (this is how they called their large-Ra regime) extends to infinitely large value of Ra, perhaps not.” [Castaing et al. \(1989\)](#) then encouraged future work on the subject.

B. Grenoble group

Indeed, the Chicago work on RB convection in cryogenic helium was followed up, namely, in Grenoble (and also in Lyon) by Bernard Castaing and colleagues. In their seminal paper, [Chavanne et al. \(1997\)](#) reported the observation of the ultimate regime for $\text{Ra} > \text{Ra}^* \approx 10^{11}$, with a pronouncedly steeper effective scaling exponent $\gamma \approx 0.38$ in the Nu versus Ra scaling relation; see Fig. 2. In these experiments, $\Gamma = 1/2$,

while Pr varies, generally increasing with increasing Ra ; see Fig. 7(a). Chavanne *et al.* (1997) also measured the local velocity at various places, namely, with anemometry with a couple of 200 μm cubic thermometers. The transition toward a steeper effective scaling exponent was confirmed by Chavanne *et al.* (2001) by experiments in the same container, who in addition, again by direct measurements of the velocity, could connect this change in the Nu versus Ra scaling with a laminar to turbulent transition of the velocity boundary layers induced by the large-scale flow near the wall of the container. The velocity measurements also revealed an effective scaling relation $Re \sim Ra^{0.49}$, which is consistent with the GL model and various other models; cf. Secs. III and V. Chavanne *et al.* (2001) found their data to be consistent with the model of Kraichnan (1962) for moderate Pr , including the nesting of the thermal boundary layer in the kinetic one, as expected for these Pr .

In the following two decades, the Grenoble and Lyon results on the transition to the ultimate regime and its various features got consolidated and extended (Chillà *et al.*, 2004a; Gauthier and Roche, 2008; Roche *et al.*, 2010; Salort *et al.*, 2014; Rusaouën *et al.*, 2018; Roche, 2020; Méthivier *et al.*, 2022), including to other aspect ratios and different Pr ranges. Gauthier and Roche (2008) and Gauthier *et al.* (2009) confirmed that the transition, there given at $Ra^* \approx 10^{12}$, is connected with a boundary-layer instability reflecting different temperature fluctuation statistics and skewness in the boundary layer below and above the transition. Chillà *et al.* (2004a) proposed that different thermal properties of the plates may explain the differences between the various experiments; however, this hypothesis could not be validated by Roche *et al.* (2005). Salort *et al.* (2014) demonstrated multistability for the flow geometry for RB containers with rough plates. Roche *et al.* (2010) showed that the transition has little or no effect on the large-scale convection roll, again giving evidence that it is a BL effect. Roche *et al.* (2010) also realized that the ultimate state may be triggered by some distortion of the flow (cf. Sec. VII.F) and explored the dependences of the heat flux and the transition on the aspect ratio Γ and Pr , covering the considerable parameter range of $0.23 \leq \Gamma \leq 1.14$ and $0.7 \leq Pr \leq 7$, even with different types of sidewalls; see Fig. 2. They found that the onset Ra^* of the transition to the ultimate regime with an effective slope of the Nu versus Ra scaling larger than $1/3$ depends on the type of sidewalls and the aspect ratio Γ , with smaller aspect ratios having a later onset; see Fig. 15(a). As mentioned in Sec. VI, based on their data they suggested a dependence of the onset Rayleigh number Ra^* as $\sim \Gamma^{-2.5}$ for aspect ratios $\Gamma < 1.5$ (and consistent with $\sim \Gamma^{-3}$ for $\Gamma \rightarrow 0$).

Roche (2020) demonstrated the robustness of the transition for various Γ and various types of thermal sidewall conditions, namely, by plotting the local slopes $\partial \log Nu / \partial \log Ra$ versus Ra of the various Nu versus Ra plots [cf. Fig. 4 of Roche (2020)], but the standard compensated plots $Nu/Ra^{1/3}$ versus Ra shown in that paper are also convincing.

Apart from plotting Nu versus Ra (or, more appropriately, modifications thereof, like the extremely useful compensated plots $Nu/Ra^{1/3}$ versus Ra or local slopes $\partial \log Nu / \partial \log Ra$ versus Ra), the Grenoble-Lyon group (Chavanne *et al.*, 2001;

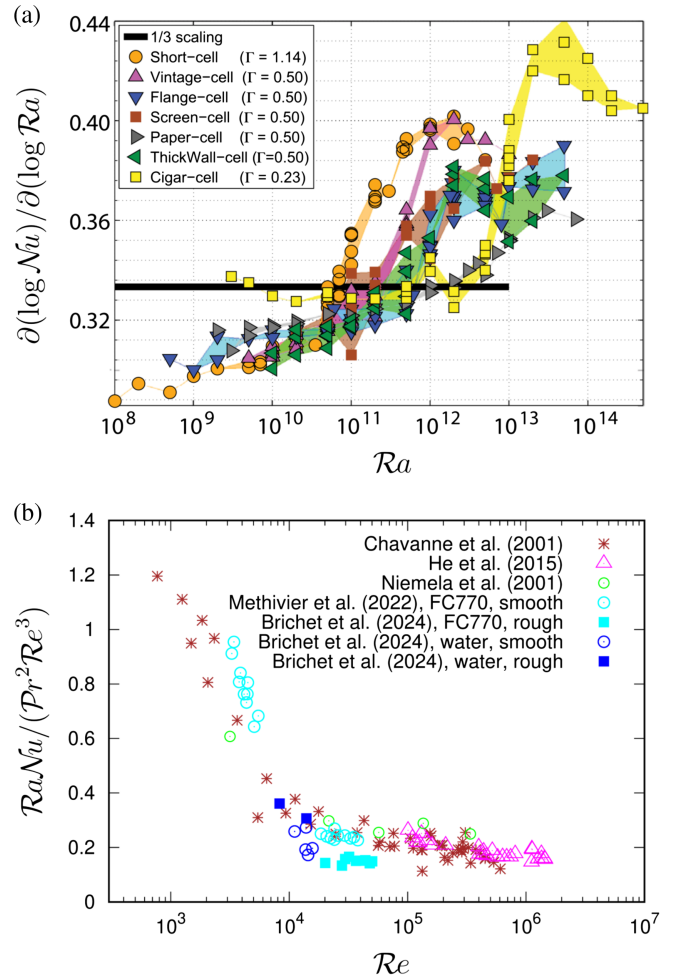


FIG. 15. (a) Local slopes $\partial \log Nu / \partial \log Ra$ as a function of Ra for various container types and aspect ratios Γ . The position of the onset of the ultimate regime depends on Γ and the type of the container, which differ in their sidewall properties. Adapted from Roche *et al.*, 2010. (b) $NuRa / (Pr^2 Re^3)$ vs Re for various RB measurements, with and without regular roughness of the plates. Adapted from Brichet *et al.*, 2024. The references in the legend refer to Chavanne *et al.* (2001), Niemela *et al.* (2001), He *et al.* (2015), Méthivier *et al.* (2022), and Brichet *et al.* (2024).

Méthivier *et al.*, 2022) went on to plot the Nu versus Re data, for example, as $NuRaPr^{-2}/Re^3$ versus Re ; see Fig. 15(b). The rationale behind this is the exact relation (13) for the kinetic energy dissipation rate and the decomposition (24) of GL theory or, equivalently, the assumption of Kraichnan (1962) and Chavanne *et al.* (1997) that $\epsilon_u \sim \nu^3 L^{-4} Re^3$ in the ultimate regime, which corresponds to the horizontal line in Fig. 15(b). Indeed, in Fig. 15(b), for large enough Ra and therefore large enough Re , the data asymptotically approach a horizontal line, which is consistent with the assumptions of an ultimate regime with a dominant energy dissipation rate of $\epsilon_u \sim \nu^3 L^{-4} Re^3$.

Finally, Roche *et al.* (2010) also analyzed the role of possible NOB effects (cf. Sec. VI.B) in the observed increase of the local Nu versus Ra scaling exponent to a value larger than $1/3$ and found that such NOB effects cannot account for the transition. In fact, various NOB effects would lower Nu rather than increase it.

C. Oregon, Trieste, and Brno groups

Russ Donnelly and his Oregon group took inspiration from Threlfall (1975) and Libchaber's Chicago group (Heslot, Castaing, and Libchaber, 1987; Castaing *et al.*, 1989; Wu and Libchaber, 1992) and performed RB experiments with cryogenic helium, but now in a much larger container with $L = 1$ m and $\Gamma = 1/2$ reaching $Ra \approx 10^{17}$ (Niemela, Skrbek, and Donnelly, 2000; Niemela, Skrbek, Sreenivasan, and Donnelly, 2000; Niemela, Skrbek, Swanson *et al.*, 2000). They provided an overall single power-law fit of the Nu versus Ra dependence in the range $10^6 \leq Ra \leq 10^{17}$, obtaining $Nu = 0.124Ra^{0.309 \pm 0.0043}$ [cf. Fig. 2(a)] without identifying any transition to an enhanced heat transport and to a steeper scaling exponent at larger Ra. The problem with plotting Nu versus Ra as in Fig. 2(a) and such an overall single power-law fit is that trends in the local slope are nearly invisible. As mentioned, these become visible in compensated plots $Nu/Ra^{1/3}$ versus Ra as in Figs. 2(b), 3, and 11 or when plotting the local slope $\partial \log Nu / \partial \log Ra$ versus Ra as in Fig. 15(a).

Niemela and Sreenivasan (2003a) extended these measurements to a $\Gamma = 1$ container ($L = 0.5$ m) reaching $Ra = 2 \times 10^{15}$. They found an enhanced heat transfer from $Ra^* \approx 10^{12}$ onward, which was larger than in their $\Gamma = 1/2$ container but not as large as in the experiments by Chavanne *et al.* (1997); cf. Figs. 2(b), 3, and 11 here and, in particular, Fig. 4 of Niemela and Sreenivasan (2003a), where only those three data sets are shown. Niemela and Sreenivasan (2003a) concluded that “consistent with the thinking of Grossmann and Lohse (2000), it is clear that a single power law is inadequate to describe the heat transfer scaling in the ($\Gamma = 1$) data over the entire range of Ra.” As seen in Fig. 2(b), beyond $Ra^* \approx 10^{12}$ the Oregon Nu versus Ra data for $\Gamma = 1$ (Niemela and Sreenivasan, 2003a) even scale more steeply than the Priestly-Malkus scaling $Nu \sim Ra^{1/3}$, though not as steeply as the Grenoble data given by Chavanne *et al.* (1997, 2001), which were well described by $Nu \sim Ra^{0.38}$. That the Oregon $\Gamma = 1$ data show a transition to a local Nu versus Ra scaling exponent larger than $1/3$ can also be seen in Fig. 9(a) of Roche (2020). Niemela and Sreenivasan (2003a) interpreted this steeper-than-one-third scaling exponent as a non-Oberbeck-Boussinesq effect (cf. Sec. VI.B) and concluded that, when restricting themselves to stricter Oberbeck-Boussinesq conditions, their large Ra data simply follow “the prediction of Grossmann and Lohse (2001) for their region IV_u , within which ... both data sets lie.”

By employing the same thermal probe technique as in Chavanne *et al.* (1997), Niemela *et al.* (2001) could also measure the scaling of the Reynolds number, resulting in $Re \sim Ra^{1/2}/Pr^{1/2}$ for $\Gamma = 1$ and in that experiment accessible Ra (up to 10^{13}).

The Oregon large Ra heat transfer RB experiments with cryogenic helium were continued in Trieste, where moreover older Oregon data were further analyzed. Niemela and Sreenivasan (2006a) provided data for Ra up to 2×10^{13} in a $\Gamma = 4$ container with a height of $L = 12.5$ cm. They found that for $Ra > Ra^* = 3 \times 10^{12}$ the slope of the Nu versus Ra curve increases significantly beyond $1/3$ but cautioned that

this may be due to non-Oberbeck-Boussinesq corrections. Niemela and Sreenivasan (2010) provided further data for a $\Gamma = 1$ container. They found an increase by about 20% in the compensated plot $Nu/Ra^{1/3}$ versus Ra at $Ra^* \approx 2 \times 10^{14}$ [cf. Fig. 1 of Niemela and Sreenivasan (2010)] but interpreted this increase as the transition from one state with $\gamma = 1/3$ slope in Nu versus Ra toward another state with the same $\gamma = 1/3$, but with a 20% larger prefactor. Niemela and Sreenivasan (2010) also provided further data for $\Gamma = 4$, confirming the transition of Niemela and Sreenivasan (2006a) to enhanced heat transport around $Ra^* = 3 \times 10^{12}$ [cf. Fig. 2 of Niemela and Sreenivasan (2010)], i.e., at a lower value of Ra as for the $\Gamma = 1$ container. This is consistent with the fact that in larger aspect ratio containers the transition should be expected at smaller Rayleigh numbers than in smaller aspect ratio containers.

We note, however, that Niemela and Sreenivasan (2010) interpreted their transitions in their $\Gamma = 1$ and 4 containers differently, namely, as a non-Oberbeck-Boussinesq effect. As “main empirical evidence against the Kraichnan argument” Niemela and Sreenivasan (2010) took “that the transition does not coincide with unique values of the similarity parameters Ra and Pr.” That argument, however, ignored the third similarity variable of the RB system, namely, the aspect ratio Γ , and the experimental and theoretical work of Roche *et al.* (2010), Shishkina (2021), Roche (2020), and Ahlers *et al.* (2022) has meanwhile firmly established the dependence of the transition to the ultimate regime on Γ . Moreover, owing to the non-normal–nonlinear behavior of the transition to the ultimate regime, even for the same Γ and the same convection container, one should not expect the onset of the heat transport increase to occur at the same Rayleigh numbers.

The Oregon large Ra RB experiments with cryogenic helium also found continuation in Brno (Urban *et al.*, 2010). Urban, Musilová, and Skrbek (2011), in a $\Gamma = 1$ container ($L = 30$ cm, no instrumentation inside the fluid, and $0.67 \leq Pr \leq 2.4$) and achieving Ra up to 4.6×10^{13} [thus smaller than the value $Ra = 2 \times 10^{14}$, where Niemela and Sreenivasan (2006a) found the transition in the $\Gamma = 1$ container], did not find any evidence for a transition to an ultimate state. Urban *et al.* (2012, 2013, 2014, 2019) and Skrbek and Urban (2015) extended the results to larger Ra up to 10^{15} , finding enhanced Nu versus Ra scaling with a local exponent $\gamma > 1/3$ of around $Ra = 10^{14}$, but argued that this would be a “spurious crossover” due to sidewall and non-Oberbeck-Boussinesq effects, breaking the top-bottom symmetry of the flow and, in particular, the deviation of the center temperature of the flow from the mean of the top and bottom plate temperature. This interpretation was challenged by He *et al.* (2013) and later by He, Bodenschatz, and Ahlers (2016), who showed that the observed transition to the regime of enhanced scaling with $\gamma > 1/3$ was robust and that there were no significant NOB effects near this transition.

Musilová *et al.* (2017) reported the scaling of the Reynolds number in the Brno $\Gamma = 1$ experiments in the range $10^8 < Ra < 10^{14}$ based on local temperature measurements with thermal sensors placed at roughly midheight of the containers. The observed transition around $Ra \sim 10^{10}$ to 10^{11} from a scaling of the energy dissipation rate ϵ_u (derived from the Nusselt number) from $\epsilon_u \sim \nu^3 L^{-4} Re^{5/2}$ to $\epsilon_u \sim \nu^3 L^{-4} Re^3$ and

toward a less steep $Re \sim Ra^{4/9}Pr^{-2/3}$ scaling of Re seems to be consistent with a transition to regime IV_u of GL theory (Grossmann and Lohse, 2000, 2001) but is not connected with the ultimate regime.

D. Göttingen: Large Ra experiments with pressurized SF₆

In RB experiments with cryogenic helium as the working fluid, achieving larger Ra generally coincides with larger Pr; see Figs. 7(a) and 7(b). When performing large-scale RB experiments with pressurized SF₆, it is possible to achieve high Ra while keeping Pr small and almost constant ($Pr < 1$); again see Fig. 7.

Employing a large $L = 2.24$ m container with $\Gamma = 1/2$ (the High-Pressure Convection Facility, which is placed inside a pressurized vessel, the so-called Göttingen U-Boot), Funfschilling, Bodenschatz, and Ahlers (2009) compared the heat flux in turbulent RB convection with SF₆, helium gas, and nitrogen at different pressures up to 15 bars, achieving Ra up to 3×10^{14} , but did not find a transition to an ultimate state with enhanced heat flux. Ahlers, Funfschilling, and Bodenschatz (2009) extended these measurements up to 19 bars and achieved $Ra = 10^{15}$. In these measurements they did not at first find a transition to a state with enhanced heat transfer either, but then did so in later experiments with the same setup, as reported in a note added in proof to the paper and, more extensively, in an addendum to the paper (Ahlers, Funfschilling, and Lohse, 2011), where beyond $Ra^* \approx 10^{13}$ they found an effective scaling of $Nu \sim Ra^\gamma$ with $\gamma = 0.36$, i.e., larger than $\gamma = 1/3$. Ahlers, Funfschilling, and Lohse (2011) and Ahlers, Bodenschatz *et al.* (2012) ascribed the smaller heat transfer measured by Ahlers, Funfschilling, and Bodenschatz (2009) to a small upward current of gas and thus spurious heat fluxes in a small gap outside the sidewalls, which in the new measurements were suppressed. Ahlers, Funfschilling, and Lohse (2011) wrote that “the heat transport in this system and at these Ra is extremely sensitive to details of the external conditions.”

Ahlers, He *et al.* (2012) and He, Funfschilling, Nobach *et al.* (2012) further refined and extended these measurements in the $\Gamma = 1/2$ container (achieving $Ra = 10^{15}$) and could then identify the transition to the ultimate state around $Ra \approx 10^{14}$. More precisely they found $\gamma \approx 0.31$ below $Ra_1^* \leq 10^{13}$ and $\gamma \approx 0.38$ above $Ra_2^* \approx 5 \times 10^{14}$; multistability was observed in between. In all of these experiments, the Prandtl number was nearly constant ($Pr \approx 0.8$). The transition in the Nu versus Ra scaling coincided with a transition in the Re versus Ra scaling, with an effective scaling exponent $\zeta \approx 0.43$ below $Ra_1^* \leq 10^{13}$, which was consistent with the classical GL regime of RB convection, and $\zeta \approx 0.50$ above $Ra_2^* \approx 5 \times 10^{14}$, which was consistent with the ultimate regime IV'_1 of GL theory. The determination of Re was done with thermal probes inside the container close to the sidewalls with which local temperature fluctuations could be measured. He, Funfschilling, Nobach *et al.* (2012) emphasized the discontinuous nature of the transition at $Ra_2^* \approx 5 \times 10^{14}$, which became visible both in Re associated with the mean flow and a Reynolds number associated with the velocity fluctuations, and interpreted the transition as a shear instability

of the BLs, which was in line with GL theory and the model of Grossmann and Lohse (2011), i.e., as the transition from the classical regime to the ultimate regime. For these experiments, Ahlers, Bodenschatz *et al.* (2012) and Ahlers, Bodenschatz, and He (2014) found a logarithmic mean temperature profile in the ultimate regime in line with the predictions of Grossmann and Lohse (2012), but logarithmic profiles can also be fitted in the classical regime, albeit in a small region (Ahlers, Bodenschatz *et al.*, 2012). He *et al.* (2014) worked out the analogies between temperature spectra and autocorrelation functions in the BLs for the ultimate regime and those for velocity spectra and autocorrelation functions in turbulent shear flow at large Reynolds numbers.

He, Funfschilling, Bodenschatz, and Ahlers (2012) extended the RB experiments with SF₆ from the $\Gamma = 1/2$ container to a $\Gamma = 1$ container [of half height as in the original container of He, Funfschilling, Nobach *et al.* (2012)], achieving up to $Ra = 2 \times 10^{14}$, again for $Pr \approx 0.8$. For $Ra \leq Ra_1^* = 2 \times 10^{13}$ they found an effective scaling exponent $\gamma \approx 0.32$, which was again consistent with the classical GL regime, and $\gamma \approx 0.37$ for larger Ra, which was consistent with the ultimate regime (He, Bodenschatz, and Ahlers, 2016). He *et al.* (2015) provided the corresponding Reynolds number measurements for that $\Gamma = 1$ container, both for the mean flow velocity (Re) and for the root-mean-square velocity fluctuations (Re_{fluct}). As with the $\Gamma = 1/2$ container, they found an effective Re versus Ra scaling exponent of $\zeta \approx 0.44$ below the transition at $Ra_1^* = 2 \times 10^{13}$

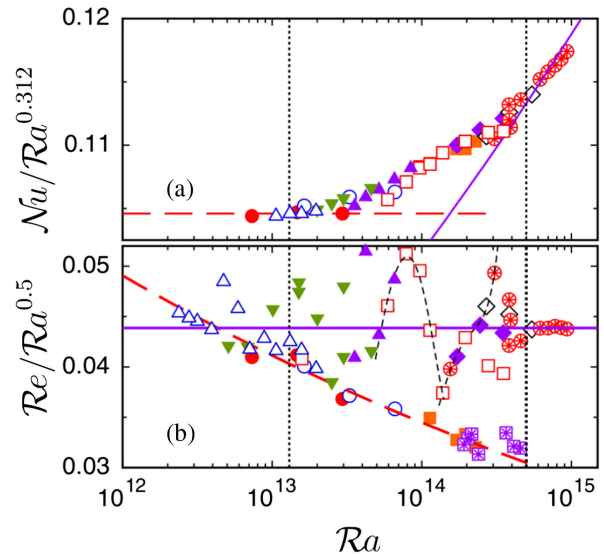


FIG. 16. Compensated (a) Nusselt number and (b) Reynolds number as a function of Ra as obtained in the Göttingen measurements in a $\Gamma = 1/2$ container using pressurized SF₆. The various symbols correspond to different operating mean pressures and temperatures. The solid purple lines correspond to $Nu \sim Ra^{0.38}$ in (a) and $Re \sim Ra^{1/2}$ in (b). The dashed red lines represent $Nu \sim Ra^{0.312}$ in (a) and $Re \sim Ra^{0.423}$ in (b). The vertical dotted black lines indicate the range of the transition, i.e., Ra_1^* and Ra_2^* . The thin dashed lines in (b) are guides for the eye to indicate the paths followed by the data. Adapted from He, Funfschilling, Nobach *et al.*, 2012.

and $\zeta \approx 0.5$ above $Ra_2^* \approx 8 \times 10^{13}$, which was again consistent with the GL interpretation of a transition from the classical to the ultimate regime. The transition was also observed in the evolution of $Re(Ra)$: for $Ra_1^* < Ra < Ra_2^*$ the $Re(Ra)$ dependency is nonmonotonic, with ups and downs, for all studied combinations of the mean temperature and pressure. However, when Ra exceeds the value of Ra_2^* , one sees $Re \sim Ra^{1/2}$; see Fig. 16. Later He, Bodenschatz, and Ahlers (2016) also found the transition in the Reynolds number associated with the azimuthal motion of the large-scale convection roll. Ahlers, Bodenschatz, and He (2017) used the experimental finding of the transition to the ultimate regime at $Ra_1^* = 2 \times 10^{13}$ for $Pr \approx 0.8$ in the $\Gamma = 1$ container to extrapolate to the case for $Pr = 0.021$ (liquid metal) based on GL theory (Grossmann and Lohse, 2000, 2001), which predicted $Ra^* \sim Pr^{3/2}$. They found $Ra^* \approx 10^{11}$ for the $Pr = 0.021$ case, which was consistent with the extrapolation of Schumacher *et al.* (2016) from their numerical results at smaller Ra .

He, Bodenschatz, and Ahlers (2022) further extended the RB experiments with pressurized SF_6 to a slender container with $\Gamma = 1/3$, achieving Ra up to 5×10^{15} . In this slender container, the transition moved up to $Ra_2^* \approx 2 \times 10^{15}$, above which the steep effective scaling $\gamma = 0.38$ of the ultimate regime can be seen in the Nu versus Ra scaling relation. The same held for the typical change in the temperature variance that is associated with the transition from the classical regime to the ultimate regime. Based on these experimental results, He, Bodenschatz, and Ahlers (2020, 2022) gave the Γ dependence of the transition toward the ultimate regime as $Ra_2^* \sim \Gamma^{-3.04}$, which was consistent with the results of Roche (2020), Shishkina (2021), and Ahlers *et al.* (2022); cf. Eq. (142).

We finally note that among the first to perform high-Ra RB experiments using SF_6 in the vicinity of its critical point were Ashkenazi and Steinberg (1999), who measured up to $Ra = 5 \times 10^{14}$, with $L = 10.5$ cm and $\Gamma = 0.72$, but found no transition to an enhanced Nu versus Ra scaling for large Ra . They varied Pr over a large range $1 \leq Pr \leq 93$ and, for the accessible range $10^9 \leq Ra \leq 10^{14}$, gave $Nu \sim Ra^{0.3 \pm 0.03} Pr^{-0.2 \pm 0.04}$ and $Re \sim Ra^{0.43 \pm 0.02} Pr^{0.75 \pm 0.02}$. These scaling relations are closer to those of the GL regime IV_u than to the ultimate scalings.

E. Lyon and Tokyo groups: Large Ra experiments with liquid mercury

According to GL theory, $Ra^* \sim Pr^{3/2}$ at the onset of the ultimate regime (Grossmann and Lohse, 2000, 2001). Thus, for low Pr liquids such as liquid metals the onset should occur at much lower Ra . However, there are not many RB experiments with liquid metals at large Ra , for cost and security reasons but also for principal reasons, as in ideal RB experiments the heat conductivity of the plates should be perfect compared to that of the liquid so that they can be kept at constant temperature. With liquid metals as fluid, however, this is difficult or even impossible to achieve, and one has to rely on corrections or deviate from the ideal RB conditions.

The first controlled high-Ra RB experiments with liquid metal involved the pioneering work⁴ of Cioni, Ciliberto, and Sommeria (1997) with liquid mercury, which has $Pr \approx 0.025$, in a container with $\Gamma = 1$. Cioni, Ciliberto, and Sommeria (1997) achieved $Ra = 5 \times 10^9$, finding a sharp transition to a much steeper Nu versus Ra dependence beyond $Ra^* = 2.1 \times 10^9$. The steeper regime was too short to extract a meaningful scaling exponent, but the data of Cioni, Ciliberto, and Sommeria (1997) showed bistability in this regime beyond $Ra = 2.1 \times 10^9$ [cf. Fig. 2(a) of their paper], with an upper branch with steeper Nu versus Ra scaling and a lower branch with the same scaling as in the classical regime, as at the onset to the ultimate regime in SF_6 measured by He, Funfschilling, Nobach *et al.* (2012). Cioni, Ciliberto, and Sommeria (1997) wrote that “the transition is possibly related to the onset of some instability occurring in the viscous boundary layer... Such boundary layer instabilities are known to be sensitive to the state of the surface of the wall, which could explain the lack of reproducibility (due to aging of the wall in contact with mercury).” They went on to write, “The Reynolds number (at the transition) corresponds to the threshold for instability in a boundary layer on a flat plane, leading to sudden enhancement of turbulence, sensitive to the presence of small perturbations, consistent with our observations of a sudden and non-reproducible transition.” This view, which was indeed pioneering and visionary, is consistent with today’s view (Roche, 2020; Lohse and Shishkina, 2023) that the transition to the ultimate regime is of a non-normal–nonlinear nature; see Fig. 3.

Prior RB experiments with mercury by Takeshita *et al.* (1996) achieved only $Ra = 10^8$ (also in a $\Gamma = 1$ container) and thus did not recognize the transition to the ultimate regime. Glazier *et al.* (1999) repeated these experiments in a $\Gamma = 1/2$ container in which they achieved $Ra = 8 \times 10^{10}$ and a $\Gamma = 2$ container in which they achieved $Ra = 10^7$. However, they did not see the transition to the ultimate regime either.

F. Reconciling the experimental findings: Non-normal–nonlinear transition

How does one reconcile the various experimental findings on high-Ra experiments reported in this section? In the conclusions of their Review of Modern Physics article on RB convection some 15 years ago, Ahlers, Grossmann, and Lohse (2009) wrote the following on the transition to the ultimate regime: “Though the Grenoble experiments suggest such a transition near $Ra = 10^{11}$, neither the Oregon-Trieste experiments nor numerical simulations do so. The reason for the discrepancy is presently unresolved.”

As reported in this section, there have been various new experiments in the past 15 years and new direct numerical simulations, as reported in Sec. VIII. The transitions to the ultimate regime found in these experiments (if any) and the

⁴D. L. notes that it was his visit with Sergio Ciliberto in Lyon at the end of October 1997 and the discussions of their mercury-RB experiment with the Pr dependence found there that triggered the development of what is now known as GL theory (Grossmann and Lohse, 2000).

TABLE II. Summary of Rayleigh numbers Ra^* for the onset of enhanced Nu vs Ra scaling with a local scaling exponent $\gamma > 1/3$. Note that in some cases in which no transition was observed the maximally achieved Ra was too small to expect such a transition.

Location	$0.23 \leq \Gamma \leq 0.33$	$\Gamma = 0.5$	$1 \leq \Gamma \leq 1.14$	$2 \leq \Gamma \leq 4$
<i>Grenoble</i> (<i>cryogenic He</i>)	$(\Gamma = 0.23)$	$(\Gamma = 0.5)$	$(\Gamma = 1.14)$	
References	Roche <i>et al.</i> (2010) Roche (2020)	Chavanne <i>et al.</i> (1997) Chavanne <i>et al.</i> (2001)	Roche <i>et al.</i> (2010) Roche (2020)	
Pr	$0.66 < Pr \leq 6.9$	$0.66 < Pr \leq 37$	$0.75 < Pr \leq 6.7$	
Ra_{\max}	$Ra_{\max} \approx 5.9 \times 10^{14}$	$Ra_{\max} \approx 2 \times 10^{14}$	$Ra_{\max} \approx 6.5 \times 10^{12}$	
Ra^*	$3 \times 10^{12} \leq Ra^* \leq 10^{14}$	$Ra^* \sim 10^{11}$	$5 \times 10^{10} \leq Ra^* \leq 3 \times 10^{12}$	
References		Gauthier <i>et al.</i> (2009) Roche (2020) and Roche <i>et al.</i> (2010)		...
Pr		$0.67 \leq Pr \leq 6.9$		
Ra_{\max}, Ra^*		$Ra_{\max} \approx 7 \times 10^{13}$ (“ThickWall”) $4 \times 10^{11} \leq Ra^* \leq 2 \times 10^{13}$ $Ra_{\max} \approx 7 \times 10^{13}$ (“Flange”) $6 \times 10^{11} \leq Ra^* \leq 2 \times 10^{13}$ $Ra_{\max} \approx 7 \times 10^{13}$ (“Vintage”) $2 \times 10^{11} \leq Ra^* \leq 2 \times 10^{13}$ $Ra_{\max} \approx 8 \times 10^{13}$ (“Paper”) $2 \times 10^{12} \leq Ra^* \leq 6 \times 10^{13}$		
<i>Lyon and Tokyo</i> (<i>mercury</i>)		(Tokyo, $\Gamma = 1/2$)	(Lyon, $\Gamma = 1$)	(Tokyo, $\Gamma = 2$)
References		Glazier <i>et al.</i> (1999)	Cioni, Ciliberto, and Sommeria (1997)	Glazier <i>et al.</i> (1999)
Pr	...	$0.024 \leq Pr \leq 0.027$	$0.021 \leq Pr \leq 0.026$	$0.018 \leq Pr \leq 0.027$
Ra_{\max}		$Ra_{\max} \approx 8 \times 10^{10}$	$Ra_{\max} \approx 5 \times 10^9$	$Ra_{\max} \approx 10^7$
Ra^*		None	2.1×10^9	None
<i>Oregon and Trieste</i> (<i>cryogenic He</i>)		$(\Gamma = 0.5)$	$(\Gamma = 1)$	$(\Gamma = 4)$
References		Niemela, Skrbek, and Donnelly (2000) and Niemela, Skrbek, Sreenivasan, and Donnelly (2000)	Niemela and Sreenivasan (2003a, 2003b)	Niemela and Sreenivasan (2006a)
Pr	...	$0.68 \leq Pr \leq 28.7$	$0.68 \leq Pr \leq 13.4$	$0.69 \leq Pr \leq 14.7$
Ra_{\max}		$Ra_{\max} \sim 10^{17}$	$Ra_{\max} \approx 2 \times 10^{15}$	$Ra_{\max} \approx 3 \times 10^{13}$
Ra^*		none or $Ra^* \sim 10^{12}$ (Roche, 2020)	$Ra^* \sim 10^{11a}$	$Ra^* \sim 2 \times 10^{10a}$
<i>Brno</i> (<i>cryogenic He</i>)			$(\Gamma = 1)$	
References			Urban <i>et al.</i> (2012, 2014, 2019)	
Pr	$0.68 \leq Pr < 11.5$...
Ra_{\max}			$Ra_{\max} \sim 10^{15}$	
Ra^*			none or $Ra^* \sim 10^{14a}$	
<i>Göttingen</i> (<i>pressurized SF₆</i>)	$(\Gamma = 1/3)$	$(\Gamma = 1/2)$	$(\Gamma = 1)$	
References	He, Bodenschatz, and Ahlers (2022)	He, Funfschilling, Nobach <i>et al.</i> (2012)	He, Funfschilling, Bodenschatz, and Ahlers (2012) and He <i>et al.</i> (2015)	
Pr	$0.78 \leq Pr \leq 0.86$	$0.78 \leq Pr \leq 0.86$	$0.78 \leq Pr \leq 0.86$...
Ra_{\max}	$Ra_{\max} \approx 4.1 \times 10^{15}$	$Ra_{\max} \approx 1.0 \times 10^{15}$	$Ra_{\max} \approx 1.4 \times 10^{14}$	
Ra_1^*	$Ra_1^* \approx 1.3 \times 10^{13}$	$Ra_1^* \approx 1.5 \times 10^{13}$	$Ra_1^* \approx 2 \times 10^{13}$	
Ra_2^*	$Ra_2^* \approx 2.3 \times 10^{15}$	$Ra_2^* \approx 7 \times 10^{14}$	$Ra_2^* \approx 8 \times 10^{13}$	

^aThe enhanced scaling was interpreted as a non-Oberbeck-Boussinesq effect.

earlier ones are summarized in Table II and in Fig. 10 for the aspect ratios $\Gamma = 4$ or 2 , $\Gamma \approx 1$, $\Gamma = 1/2$, and $\Gamma = 0.23$ or $1/3$.

There are two distinct reasons for the different transition Rayleigh numbers Ra^* in these experiments, namely, the difference in the control parameters Prandtl number Pr and

aspect ratio Γ . First, regarding the Prandtl number dependence: As stated, for mercury ($Pr \approx 0.02$) the found Ra^* scaling is in line with the GL prediction $Ra^* \sim Pr^{3/2}$ (Grossmann and Lohse, 2000, 2001) when one extrapolates the onset Ra^* from $Pr = 0.8$ (and the same $\Gamma = 1$) down to $Pr = 0.02$. For the

onset Ra^* at $Pr = 0.8$ Roche *et al.* (2010) gave 10^{11} , Niemela, Babuin, and Sreenivasan (2010) gave 10^{12} (though they interpreted the results differently), and He *et al.* (2015) gave 2×10^{13} . If we take the rough geometric mean 10^{12} , then the expectation at $Pr = 0.02$ would be $Ra^* = 10^{12} \times (0.02/0.8)^{3/2} \approx 4 \times 10^9$ rather than the measured $Ra^* \approx 2 \times 10^9$, and thus order of magnitude-wise in line. Further Pr dependences of the onset in the range $0.8 \leq Pr \leq 7$ for cryogenic helium were discussed by Roche *et al.* (2010), but more data are necessary to further understand this issue.

Second, regarding the aspect ratio Γ dependence: This dependence is visible in Table II and Fig. 10, in which we also plotted the theoretical expectation equation (142) of Ahlers *et al.* (2022), which is in line with the data. The theory explaining this dependence was discussed in Sec. VI.A.

But beyond the obvious reasons for the variations in Ra^* (the dependence on the control parameters Pr and Γ) there must be another reason; otherwise, the wide spread of Ra^* even for roughly the same control parameters Pr and Γ cannot be accounted for. The crucial idea of how to understand this variation of Ra^* for the onset of the ultimate transition even for roughly the same control parameters was put forward first by Roche (2020) and later by Lohse and Shishkina (2023). The idea was to interpret it as a subcritical transition of a non-normal–nonlinear nature similar to the transition from laminar to turbulence in pipe flow or channel flow; cf. Fig. 2 of Roche (2020) and Fig. 4 here. Previously many (Chavanne *et al.*, 1997; Cioni, Ciliberto, and Sommeria, 1997; Grossmann and Lohse, 2000, 2001, 2004, 2011; Chillà *et al.*, 2004a; Gauthier and Roche, 2008; Gauthier *et al.*, 2009; Roche *et al.*, 2010; Ahlers, He *et al.*, 2012; He, Funfschilling, Bodenschatz, and Ahlers, 2012; He, Funfschilling, Nobach *et al.*, 2012; He, Bodenschatz, and Ahlers, 2020) did realize that the onset of the ultimate regime is a shear instability of the laminar-(Prandtl-Blasius-) type BL, including taking the Tollmien value $Re_s^* = 420$ as a typical value for the onset (Grossmann and Lohse, 2000, 2001), but in contrast to Roche (2020) they did not fully appreciate the consequences of this insight, namely, that all characteristics of the non-normal–nonlinear transition carry over to the transition toward ultimate RB. As explained in the Introduction and in Sec. III.C, these characteristics are the subcritical nature of the onset, the possibility of multiple states in the range of the onset, and the double-threshold condition for the onset, with both Re_s and the distortions large enough for the onset to happen and, as a result, the pronounced sensitivity of the onset to distortions.

Indeed, all of these features of the non-normal–nonlinear transition did occur in the experiments described in Secs. VII.B–VII.E. For example, Ahlers (2000), Roche, Castaing, Chabaud, Hébral, and Sommeria (2001), Verzicco (2002), Chillà *et al.* (2004a), and Brown *et al.* (2005) showed that the thermal properties of the sidewalls and the top and bottom plates, respectively, have a significant influence on whether and when the transition occurs and on how smooth it is. Niemela and Sreenivasan (2003a) mentioned the important role of the thermal conditions of the sidewalls. In addition, the multistability of the convective system at large Rayleigh numbers has been reported (Cioni, Ciliberto, and Sommeria,

1997; Roche *et al.*, 2002; Chillà *et al.*, 2004a; Weiss and Ahlers, 2011; Salort *et al.*, 2014).

In these experiments the flow can show a seemingly statistically stable equilibrium for a long time (of the order of the diffusion times L^2/ν or L^2/κ) but can then nevertheless undergo a transition to another state with different transport properties. This is usually associated with changes related to the large-scale circulation, e.g., with its reversals or cessations (Villermaux, 1995; Cioni, Ciliberto, and Sommeria, 1997; Brown, Nikolaenko, and Ahlers, 2005; Brown and Ahlers, 2006; Xi, Zhou, and Xia, 2006; Xi and Xia, 2007) or with changes in the global flow structure, for example, among one, two, or more rolls (Weiss and Ahlers, 2011). However, Salort *et al.* (2014), who conducted measurements in a convection container with small regular roughness using water as the operating fluid, observed a flow multistability that was not associated with any changes (reversals) in the large-scale circulation. A small tilt of the convection container (Chillà *et al.*, 2004a; Weiss and Ahlers, 2013) can also have a visible effect on the heat transport and lifetime of the different states. When analyzing the transitions between different global flow states in a large Ra experiment ($5 \times 10^{11} < Ra < 4 \times 10^{12}$) in a $\Gamma = 1/2$ container filled with water and slightly inclined (a tilt less than 0.03 rad), Chillà *et al.* (2004a) observed multistability and concluded that “the Nusselt number observed in most high Ra experiments should significantly depend on initial conditions.” We note that all additional kinds of “noises” (vibration, instrumentation, or any other factors that can be understood as small additional body forces) can influence the transition to the ultimate regime.

What about the shear Reynolds number Re_s of the transition range? As discussed in Secs. I and III.C, a non-normal–nonlinear transition can occur in a considerable range of Re_s , and the earlier the transition occurs, the larger the distortion is (double-threshold behavior). As a guideline, Grossmann and Lohse (2000, 2001) took $Re_s^* = 420$ as a typical value for the onset, motivated by Tollmien (1929) and Landau and Lifshitz (1987). We assume that the transition given by He, Funfschilling, Nobach *et al.* (2012) (for $\Gamma = 1/2$ and $Pr = 0.8$) at $Ra^* \approx 10^{14}$ (disregarding the differences between Ra_1^* and Ra_2^*) corresponds to $Re_s = 420$. What shear Reynolds number then would the transition at $Ra \approx 10^{11}$ or 10^{12} [observed by Chavanne *et al.* (1997, 2001) and Gauthier *et al.* (2009) for the same $\Gamma = 1/2$ and a slightly larger Pr] correspond to? As $Re_s \sim Ra^{1/4}$, this would be a shear Reynolds number of 75 or 133, which indeed is in a range where with some larger distortion of the boundary layer such a transition could happen, in particular, considering that a thermal probe had been placed in the BL of the RB experiments of Chavanne *et al.* (1997, 2001), which could trigger an instability of the BL.

We also interpret the existence of two distinct transitional Rayleigh numbers Ra_1^* and Ra_2^* in the Göttingen experiments in light of the non-normal–nonlinear nature of the onset, with Ra_1^* the Rayleigh number (and the corresponding shear Reynolds number $Re_{s,1}^*$) from which a jump to the turbulent BL state is possible for large enough distortions, and Ra_2^* the Rayleigh number (and corresponding shear Reynolds number $Re_{s,2}^*$) above which the laminar-type BL cannot recover.

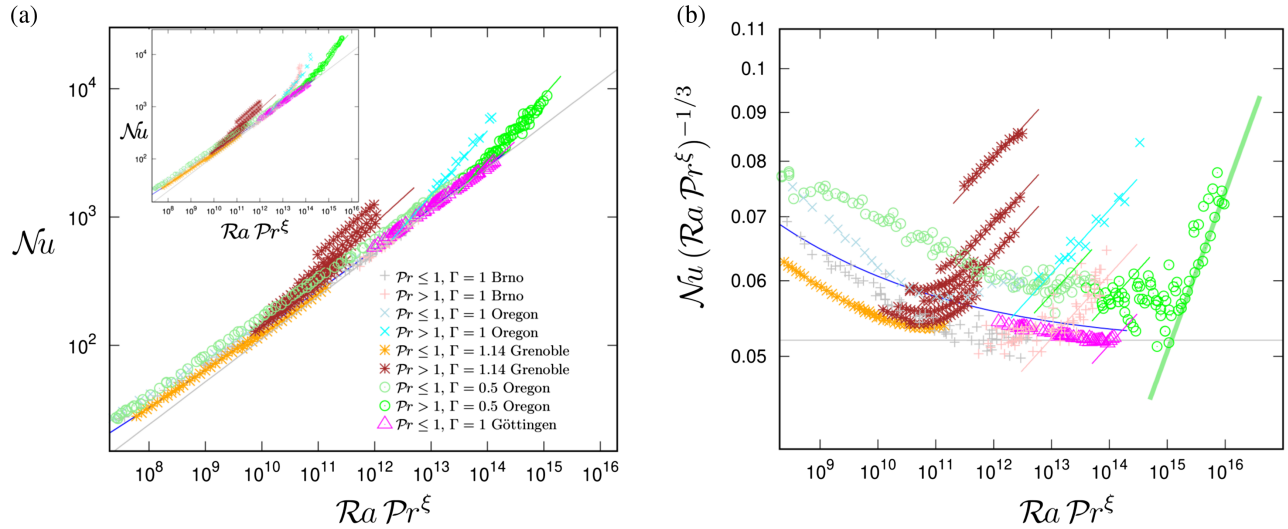


FIG. 17. (a) Nu vs $RaPr^\xi$ (with $\xi = 1$ for $Pr \leq 1$ and $\xi = -1$ for $Pr > 1$) and (b) compensated Nusselt number $Nu(RaPr^\xi)^{-1/3}$ vs $RaPr^\xi$ [where the function $\hat{\xi}(Pr) \equiv -\tanh(0.5\log_{10} Pr)$ helps smoothly connect the two regimes $\xi = 1$ for $Pr \ll 1$ and $\xi = -1$ for $Pr \gg 1$], as obtained in different Rayleigh-Bénard experiments in cylindrical containers; see the Fig. 2 caption for reference information. The blue curve shows the Grossmann-Lohse predictions for the classical regime for $Pr = 1$ and $\Gamma = 1$. The inset of (a) presents all available data, while the main (a) and (b) contain data only for $\alpha\Delta < 15\%$ (i.e., with one of the Oberbeck-Boussinesq conditions fulfilled; see Sec. VI.B). All datasets at the highest Rayleigh numbers achieved in these experiments show the transition to the ultimate regime, with slopes between $Nu \sim Ra^{0.4}$ (the thin solid brown, cyan, green, pink, and magenta lines) and $Nu \sim Ra^{0.5}$ (the thick solid green line). These transitions are also seen in the noncompensated plot (a). The same datasets are considered here as in Fig. 2.

We now discuss possible NOB effects (see Sec. VI.B) that were put forward by the Oregon, Trieste, and Brno groups to account for their observed transitions; see Sec. VII.C and Table II. Though NOB effects exist (see our discussion in Sec. VI.B), from our point of view the following arguments hold against this interpretation: (i) NOB effects generally set in gradually, whereas the observed transitions in the Oregon, Trieste, and Brno data are sudden, as expected for the onset of the non-normal–nonlinear instability. (ii) Direct numerical simulations⁵ (however, in the classical regime at lower Ra) show that in SF_6 and cryogenic helium the NOB effects on the heat transport are negligible and lead to a reduction of the Nusselt number, as in water or glycerol (Horn, Shishkina, and Wagner, 2013; Horn and Shishkina, 2014). In contrast, the increase in the experimentally measured Nu at the transition is large, far beyond a few percent. (iii) The observed transitions in the Oregon, Trieste, and Brno data are basically in the Ra range, where one would expect the non-normal–nonlinear instability of the laminar-type BL toward a turbulent-type BL for the given aspect ratio Γ and Pr ; i.e., the shear Reynolds number Re_s is in the appropriate range for such a transition. We speculate that the NOB effects, like any other distortion, can trigger the non-normal–nonlinear instability of the boundary layers, which at the end leads to a qualitative change in heat transport and a dramatic growth of Nu .

⁵Among all SF_6 and He properties the most sensitive one to temperature variation is the specific heat at constant pressure c_p . DNS for an extreme variation of c_p (as in the measurements at the highest Ra) considered for Ra up to 10^{10} show only a slight variation in Nu compared to the OB cases (Weiss, Emran, and Shishkina, 2024).

At the end of this section, we reconsider the experimental data presented in Fig. 2 in light of the model equations (136) and (137); cf. Fig. 9. According to the model, in the ultimate regime the following scaling should hold (up to logarithmic corrections): $Nu \sim Pr^{\pm 1/2} Ra^{1/2}$, where a negative exponent ($-1/2$) for Pr should be taken for large Pr and a positive one ($+1/2$) for small Pr . Thus, the Nusselt number is a function of $Pr^\xi Ra$, with $\xi = 1$ for $Pr \leq 1$ and $\xi = -1$ for $Pr > 1$. In Fig. 17(a), the experimental data considered for Nu are plotted versus $Pr^\xi Ra$. One sees that all datasets, including the Oregon data, follow a scaling close to $Nu \sim (Pr^\xi Ra)^\gamma$, with $\gamma \approx 1/3$ for smaller values of $Pr^\xi Ra$ and γ between 0.4 and 0.5 at the highest values of $Pr^\xi Ra$.

Figure 17(b) provides a compensated plot of $Nu(RaPr^\xi)^{-1/3}$ versus $RaPr^\xi$. Here $\hat{\xi}$ is a function of Pr that substitutes the discontinuous change of ξ from $+1$ to -1 at $Pr = 1$ for a continuous and smooth function $\hat{\xi}(Pr) \equiv -\tanh(d\log_{10} Pr)$ that matches the small Pr and large Pr regimes. [Here different options are possible to match the small Pr and large Pr regimes, particularly by optimizing the constant d , which in Fig. 17(b) equals $d = 0.5$.] All data again show a transition for large Ra . The thin inclined lines in Fig. 17(b) highlight the scaling exponent $\gamma = 0.4$ and the thick green line $\gamma = 0.5$. We interpret the results in Fig. 17(b) as support for the model of Eqs. (136) and (137); cf. Fig. 9.

G. Which experiments can verify and illuminate the subcritical nature of the transition to the ultimate regime?

Which further experiments should be done to learn more about the transition to ultimate turbulence? Larger Ra and a

larger range of the other two control parameters (Pr and Γ) are needed. Indeed, Table II has various gaps and should be extended to larger and smaller Γ and different Pr , which in the best case do not vary too much when one increases Ra . In particular, more measurements with liquid metals ($Pr \approx 0.02$) are needed, but also those for much larger Pr , for which only a few measurements of the heat flux exist (Xia, Lam, and Zhou, 2002). In addition to heat flux measurements, measurements on the Reynolds number are also needed and, in the best case, noninvasive. One should also continue trying to measure the velocity and temperature profiles in the boundary layers to directly verify their logarithmic character in the ultimate regime. These are all obvious extensions of the present type of measurements.

But we also suggest new types of experiments, namely, those that explicitly probe the non-normal–nonlinear nature of the transition to ultimate turbulence, to further establish (or falsify) and illuminate it. These experiments can be along the lines of what was done by Hof *et al.* (2006) and Avila *et al.* (2011, 2013) for pipe and channel flow [see also the reviews on the non-normal–nonlinear transition mentioned in the Introduction (Grossmann, 2000, Schmid and Henningson, 2001, Kerswell, 2002, Eckhardt *et al.*, 2007, Schmid, 2007, Barkley, 2016, Manneville, 2016, Wu, 2019, Avila, Barkley, and Hof, 2023)], namely, to locally apply controlled disturbances to the flow (here the BLs) such as placing obstacles, an injection of jets, and local vibrations at various Ra , and measure how the flow reacts: Can the transition from a laminar to a turbulent BL be triggered and identified based on local measurements or the overall heat transfer? And if so, what is the lifetime of the new turbulent state and how does it depend on Ra ? Does the laminar state recover? We also suggest probing the hysteretic character of the transition by slowly increasing and decreasing Ra around the transition. The non-normal–nonlinear picture suggests that the onset of the ultimate state should occur at larger Ra compared to the offset when decreasing Ra again. Performing corresponding experiments can confirm (or refute) the hypothesis about the subcritical nature of the transition to the ultimate regime.

VIII. LARGE RAYLEIGH NUMBER NUMERICS

A. 3D Rayleigh-Bénard flow simulations in the classical regime

One of the first direct numerical simulation (DNS) of 3D turbulent RB convection was done by Kerr (1996), who employed a spectral code with lateral periodicity boundary conditions. Kerr achieved $Ra = 2 \times 10^7$ on a $288 \times 288 \times 96$ grid. For $Pr = 0.7$ he found an effective power law $Nu \sim Ra^{0.28}$.

We first focus on large Ra DNS. Verzicco and Camussi (1999, 2003) and Stringano, Pascazio, and Verzicco (2006), building on the advanced finite difference scheme developed by Verzicco and Orlandi (1996), achieved up to $Ra = 2 \times 10^{11}$ for $Pr = 0.7$ in a slender container with $\Gamma = 1/2$. Using the same method, Stevens, Verzicco, and Lohse (2010) and Stevens, Lohse, and Verzicco (2011) achieved $Ra = 2 \times 10^{12}$ for a cylindrical container with $\Gamma = 0.23$ and $1/2$ and $0.5 < Pr < 10$. The largest currently achieved Rayleigh

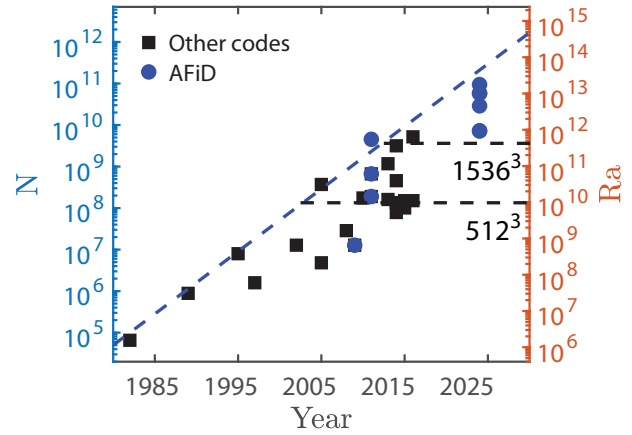


FIG. 18. Number of grid points N and Ra , which were achieved in sufficiently resolved 3D direct numerical simulations for a cylindrical container with $\Gamma = 1/2$ and $Pr \approx 1$, as a function of the available computational power, expressed during the year the simulation was done. Black squares, various data from the literature; blue bullets, simulations from Stevens, Lohse, and Verzicco (2020) and their prior data. Unpublished data from Stevens *et al.* are also included. Adapted from Stevens, Lohse, and Verzicco, 2020.

number⁶ is $Ra = 10^{13}$ for a cylinder $\Gamma = 1/2$; see Stevens, Lohse, and Verzicco (2020) and Figs. 18 and 19. This second-order finite difference code AFiD/RBflow was then further optimized, including for GPUs, by van der Poel *et al.* (2015) and Zhu, Mathai *et al.* (2018), who achieved $Ra = 10^{11}$ for laterally periodic boundary conditions.

There are other popular computational DNS codes that have also been used to study different aspects of turbulent Rayleigh-Bénard convection at smaller Ra . GOLDFISH code [see Shishkina *et al.* (2015), Reiter, Zhang *et al.* (2021), and Reiter, Zhang, and Shishkina (2022)] applies a fourth-order finite-volume discretization on staggered grids and a third-order Runge-Kutta time marching scheme. It was used to study thermal convection enhanced by rotation (Horn and Aurnou, 2018, 2019; Zhang *et al.*, 2020; Ecke, Zhang, and Shishkina, 2022; Ecke and Shishkina, 2023) or magnetic field (McCormack *et al.*, 2023; Teimurazov *et al.*, 2024) and convection at extremely small Prandtl numbers (Zwirner, Tilgner, and Shishkina, 2020; Zwirner *et al.*, 2020, 2022; Teimurazov *et al.*, 2023).

Other studies of Rayleigh-Bénard convection, also at Prandtl numbers that correspond to liquid metals, were conducted with a general purpose spectral-element code NEK5000; see Scheel and Schumacher (2016, 2017), Schumacher *et al.* (2016), and Pandey, Scheel, and Schumacher (2018). Although NEK5000 is significantly slower than dedicated codes like AFiD or

⁶Iyer *et al.* (2020) tried to calculate Nu for Ra of up to 10^{15} and $\Gamma = 1/10$. The Supplemental Material for that paper shows that the error intervals of the calculated Nusselt numbers are large. For $Ra = 10^{13}$ the error intervals for Nu calculated in different ways, namely, either evaluated at the plates or averaged over the entire volume, do not even intersect, which reflects the lack of grid resolution and/or statistical convergence. The reported Nu values therefore do not reflect the true heat transport in the system.

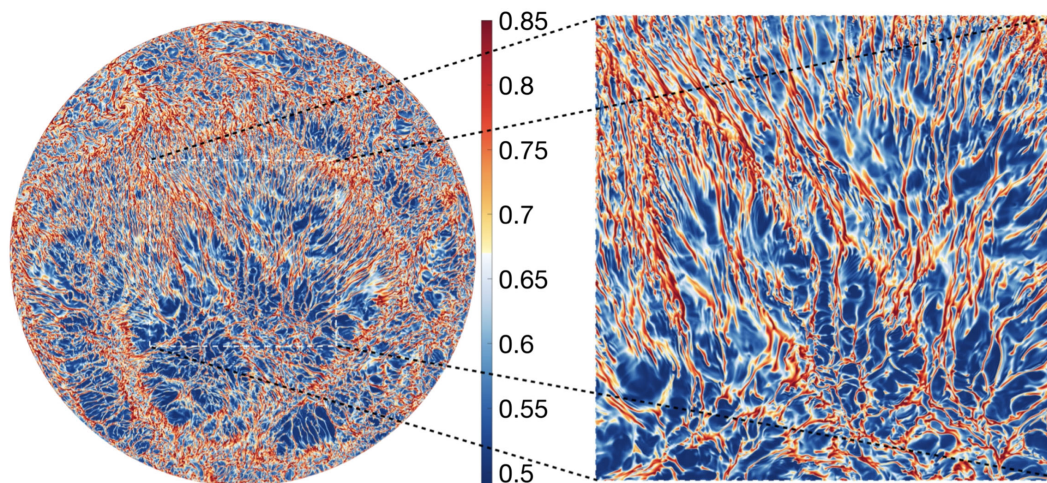


FIG. 19. Cross-sectional snapshot of the dimensionless temperature $(T - T_0)/\Delta$ as obtained in a fully resolved DNS of Stevens, Lohse, and Verzicco (2020) for $Ra = 10^{13}$, $Pr = 1$, and $\Gamma = 1/2$ at a distance of $z \approx \lambda_\theta$ from the bottom plate. Evident are the small thermal plume structures, which are visible due to the large grids employed in the simulation. Right panel: enlargement of the indicated area.

GOLDFISH [as Kooij *et al.* (2018) showed in a direct quantitative comparison at $Ra = 10^8$, $Pr = 1$, and $\Gamma = 1$], it has its own advantages, such as the ability to accurately calculate higher-order moments of flow components and to give a more detailed analysis of the boundary-layer structure provided that the grid resolution is sufficient and the convergence time large enough, as done by Scheel, Emran, and Schumacher (2013), Scheel and Schumacher (2014, 2016, 2017), and Schumacher *et al.* (2016). Bailon-Cuba, Emran, and Schumacher (2010) focused on cylindrical containers with large aspect ratios up to $\Gamma = 12$, with the cost restricted to at most $Ra = 10^9$. Emran and Schumacher (2015) even achieved the large aspect ratio $\Gamma = 50$, for which they were limited to $Ra = 5 \times 10^5$. All of these simulations are still far into the classical regime and quite far from the ultimate regime.

How does one numerically achieve the ultimate regime in 3D simulations? No kind of turbulence modeling, including Reynolds-averaged Navier-Stokes (RANS) simulations and large-eddy simulations (LESs) with available turbulence models, can be used to study the flow physics of the ultimate regime or the transition to this regime. To develop accurate turbulence models for the ultimate regime required for such RANS simulations or LESs, one must first know the detailed flow physics in that regime, which can be studied only through experiments and DNSs. DNSs, however, require fine resolution of the flow, i.e., fine computational grids in space and time, on the level of the Kolmogorov scales. We further discuss this in Sec. VIII.B. Under-resolved DNS might be interpreted as a type of LES modeling with an imposed (generally inaccurate) turbulence model, which then leads to incorrect results.⁷

⁷Amati *et al.* (2005) and Verzicco and Sreenivasan (2008) achieved $Ra = 2 \times 10^{14}$ at $Pr = 0.7$ and $\Gamma = 1/2$, but only at the cost of considerably overestimated heat transfer (i.e., Nu), as the dissipative flow structures are not resolved, as shown by Stevens, Verzicco, and Lohse (2010). Given the exact relation (14), which directly connects the thermal dissipation rate ϵ_θ with Nu , this connection is straightforward.

Thus, DNSs with sufficiently fine grids and sufficiently large time of statistical averaging seem to be the straightforward and correct way to numerically study high- Ra thermal convection, including the ultimate regime in RB convection. DNSs at high Ra are expensive. To save resources and ease the approach of the ultimate regime, one might consider simulating only a slender convection container, i.e., a container with $\Gamma \ll 1$. However, this is not viable. As we see in Sec. VIII.B, the complexity of the DNS, i.e., the number of operations needed to complete the DNS for a Rayleigh number at the transition to the ultimate regime, scales as $\sim \Gamma^3$ for large Γ and as Γ^{-1} for small Γ (Shishkina, 2021). Therefore, simulations with Γ of the order of 1 are the most reasonable when one wants to achieve large Ra . When making $\Gamma \ll 1$ smaller and smaller for large Ra , due to the required increase in computational resources as Γ^{-1} , one inevitably encounters under-resolution, a short statistical averaging time, too early of a start in collecting statistical information, or all of these problems.⁸

B. Basic resolution and convergence requirements for a direct numerical simulation

The requirements for a well-resolved numerical RB simulation were formulated first by Grötzbach (1983) and then with enhanced requirements by Shishkina *et al.* (2010), Stevens, Verzicco, and Lohse (2010), and Stevens *et al.* (2011) and in the Supplemental Material of Ahlers *et al.* (2022), which we closely adhere to in the following. These requirements hold in the classical regime, as described in Sec. VIII.A, and all the more so in the ultimate regime, for two reasons: First, there the fluctuations are even more intermittent (i.e., there is a larger flatness of the signals). Second, in the ultimate regime the BLs are even thinner, which requires not only more grid points because of the smaller BL thickness but also more grid points per BL thickness, as we explain in the following.

⁸For details on an attempt to calculate the heat transport at Ra up to 10^{15} for $\Gamma = 1/10$, see footnote 6.

The total number of grid points for a simulation is given by the sum of those needed to resolve the boundary layers and those for the bulk: the former depend on the boundary layer (thermal or kinetic), while the latter depend on the Kolmogorov (or Batchelor) scale and have a different dependence on the Rayleigh number. Having both regions with their much different flow dynamics (as also reflected in the GL approach of splitting the dissipation rates in the BL and the bulk part) properly discretized is crucial for the reliability of the numerical results, and their resolution requirements must be satisfied simultaneously. Moreover, what is crucial is that the statistical averaging of the data must be over a long enough period of time to achieve statistical convergence and that it must not start prior to the development of a statistically steady flow. We summarize these important criteria for the quality of direct numerical simulations of turbulent RB convection in confined geometry as follows.

Total number of grid points. Since the number of grid points in the bulk grows with Ra at a faster rate than that in the boundary layer, eventually the former becomes dominant, and one can estimate the total mesh size in direct numerical simulations while considering only the first contribution (with the caution that the actual number of nodes should always be larger). In particular, for cylindrical containers with the aspect ratio Γ an estimate for the required total number of grid points N (or, equivalently, the number of mesh cells or degrees of freedom) is

$$N \approx \frac{\pi \Gamma^2 L^3}{4 \eta^3} \sim \Gamma^2 \left(\frac{L^4 \epsilon_u}{\nu^3} \right)^{3/4} \quad (149)$$

(Shishkina *et al.*, 2010; Stevens, Verzicco, and Lohse, 2010; Stevens *et al.*, 2011), where $\eta \equiv \nu^{3/4} / \epsilon_u^{1/4}$ is the Kolmogorov microscale. With increasing computational power in recent decades, this number of grid points N has grown considerably, as shown in Fig. 18, thus allowing for larger and larger Rayleigh numbers in the simulations. We stress that the total number of grid point being large enough is not sufficient, as the flow field must be resolved in a proper way at all locations to avoid situations when some regions are over-resolved and the others are under-resolved.

Number of grid points in the boundary layers. In addition to the total number of grid points, what is also essential for accurate and well-resolved simulations is the boundary-layer resolution (Grötzbach, 1983; Shishkina *et al.*, 2010; Stevens, Verzicco, and Lohse, 2010). Shishkina *et al.* (2010) derived a lower bound for the number of required grid points in the thermal boundary layer, namely,

$$N_{\text{th,BL,min}} \approx 0.35 \text{Ra}^{0.15}, \quad (150)$$

which holds for $10^6 \leq \text{Ra} \leq 10^{10}$ and $\text{Pr} \approx 0.7$; see Eq. (44) of Shishkina *et al.* (2010). This implies that for increasing Ra an increasing number of grid points must be placed in the thermal boundary layers, which is in agreement with the numerical simulations of Stevens, Verzicco, and Lohse (2010). For larger $\text{Ra} > 10^{10}$ the power law $N_{\text{th,BL}} \sim \text{Ra}^{0.15}$ becomes even steeper due to the transition to turbulence of the boundary layers and the intermittency of the temperature field (Stevens *et al.*, 2011), as previously mentioned.

Statistical convergence. Not only resolution issues but also statistical stationarity and statistical convergence are important for the production of accurate data in DNS. One can only start to collect statistics when the flow is fully developed and has attained a statistically stationary state. This requires initial transient calculations to be run and, only after the statistically stationary state has been achieved, statistics to be collected for a sufficiently long time (Shishkina *et al.*, 2010; Stevens, Verzicco, and Lohse, 2010; Stevens *et al.*, 2011).

How many time steps N_t are needed in the simulations? The time steps N_t should scale as a ratio of the turnover time $\tau \sim 2(L+D)/U$ and the Kolmogorov time microscale $\tau_\eta \equiv (\nu/\epsilon_u)^{1/2}$, i.e., as

$$N_t \sim \frac{L+D}{U} \frac{\epsilon_u^{1/2}}{\nu^{1/2}} \sim \frac{\Gamma+1}{\text{Re}} \left(\frac{L^4 \epsilon_u}{\nu^3} \right)^{1/2}. \quad (151)$$

From the scaling relations (149) and (151) we find that the complexity of the DNS (the number of operations Σ) grows at least as fast as

$$\begin{aligned} \Sigma &\gtrsim N N_t \sim \frac{(\Gamma+1)\Gamma^2}{\text{Re}} \left(\frac{L^4 \epsilon_u}{\nu^3} \right)^{5/4} \\ &= \frac{(\Gamma+1)\Gamma^2}{\text{Re}} \text{Ra}^{5/4} (\text{Nu}-1)^{5/4} \text{Pr}^{-5/2} \\ &\gtrsim (\Gamma+1)\Gamma^2 \text{Ra}. \end{aligned} \quad (152)$$

In the estimate (152) we use the scaling relations of the classical regime. Therefore, the DNS complexity for $\text{Ra} \approx \text{Ra}^*$, i.e., close to the transition to the ultimate regime, scales with Γ as $\Sigma \gtrsim \Gamma^3$ for large $\Gamma \gg 1$ (as then Ra^* is independent of Γ), while for small $\Gamma \ll 1$ we have $\Sigma \gtrsim \Gamma^{-1}$ (as then $\text{Ra}^* \sim \Gamma^{-3}$). Therefore, $\Gamma \sim 1$ is the most reasonable choice to numerically achieve large Ra. Converged direct numerical simulations with smaller Γ generally require longer computational time, as confirmed by Zwirner, Tilgner, and Shishkina (2020) and Hartmann *et al.* (2021).

We add two notes on the issue of statistical convergence: First, for small Γ , the temporal averaging cannot be compensated by area averaging, as in the case of large Γ . Second, different flow quantities can require different averaging time for statistical convergence due to different probability distributions. For example, obtaining the average of higher-order moments takes more time than that of lower-order moments, as in the former the rare events of the tails of the probability distribution function have larger weight relative to what is the case for lower-order moments.

The aforementioned considerations on resolution and convergence imply that taking slender containers (i.e., small Γ) in the numerical simulations does not help one to achieve larger Ra with a well-resolved grid resolution and statistical convergence. This is intuitive upon realizing the large area of the sidewalls of containers with small Γ , implying a relatively large volume fraction of (here sidewall) BLs, which requires a particularly fine resolution. For a given plate size and maximal temperature difference Δ_{max} , the optimal aspect ratio Γ_{opt} of a cylindrical container that maximizes the Rayleigh number range between Ra_{max} (based on Δ_{max}) and the Rayleigh

number Ra_c for the onset of convection in that container is $\Gamma_{\text{opt}} \approx 0.46$ (Shishkina, 2021).

C. 2D Rayleigh-Bénard flow simulations at large Ra

To begin, one may want to ask what one could learn on 3D RB flow from 2D RB DNS. By 2D RB DNS we mean solving the dynamical equations given in Sec. II with their corresponding boundary conditions in a 2D domain. We note that this is much different from the limit of 3D RB, with one lateral dimension made small, as in that Hele-Shaw-type limit the flow is strongly stabilized by the no-slip sidewalls in that lateral direction (Chong and Xia, 2016; Chong *et al.*, 2018). While 2D and 3D homogeneous isotropic turbulence behave much differently due to an extra time-conserved quantity in the 2D case [enstrophy; cf. the seminal paper by Kraichnan (1967)], this does not hold for 2D and 3D RB turbulence, where this extra conserved quantity is absent due to the symmetry breaking by gravity.

Indeed, the theoretical arguments given in Sec. III (underlying GL theory) and many of those in Secs. IV and V are based on the Prandtl boundary-layer equations, which are two dimensional and which should hold equally well for 2D and 3D situations. Correspondingly, the usefulness of 2D RB DNS for the understanding of RB flow has been repeatedly demonstrated, from the early 2D RB DNS of Werne *et al.* (1991) on. van der Poel, Stevens, and Lohse (2013) systematically compared 2D and 3D RB DNS with respect to flow topology, boundary layers, and transport properties. While the large-scale flow topology in two and three dimensions can be much different due to the stronger confinement in two dimensions, the boundary-layer structures and the resulting heat transport (for sufficiently large Pr) are much less so. The reason for this lies in the fact that both 2D and 3D flows are driven by detaching thermal plumes from the BLs and the instabilities of the BLs.

For direct numerical RB simulations, the resolution and convergence criteria outlined in Sec. VIII.B in principle hold for both the 3D and 2D cases. 2D DNSs have the immediate advantages that there are many fewer grid points and that therefore they seem to be computationally cheaper. However, they come with the caveat that the time to achieve statistical convergence (expressed in large-eddy turnover times) is much longer than in three dimensions. This can be intuitively understood from the stronger confinement of the flow in two dimensions than in three dimensions. Another consequence of this stronger confinement in 2D RB simulations is the pronounced dependence of the flow on the initial flow conditions and the long transients, as shown by Wang *et al.* (2020, 2021) and Wang, Goluskin, and Lohse (2023).

In this review on the ultimate regime, we do not further report on the many 2D DNSs in the classical regime, but instead focus on the 2D DNSs with the largest Ra , namely, those discussed by Zhu, Mathai *et al.* (2018, 2019), who achieved up to $Ra = 4.64 \times 10^{14}$ on a $31\,200 \times 25\,600$ grid with 28 grid points in the boundary layers, with $Pr = 1$ and $\Gamma = 2$ with periodicity boundary conditions in the lateral direction. They did so by employing the highly parallelized and optimized AFiD code (van der Poel *et al.*, 2015). Note

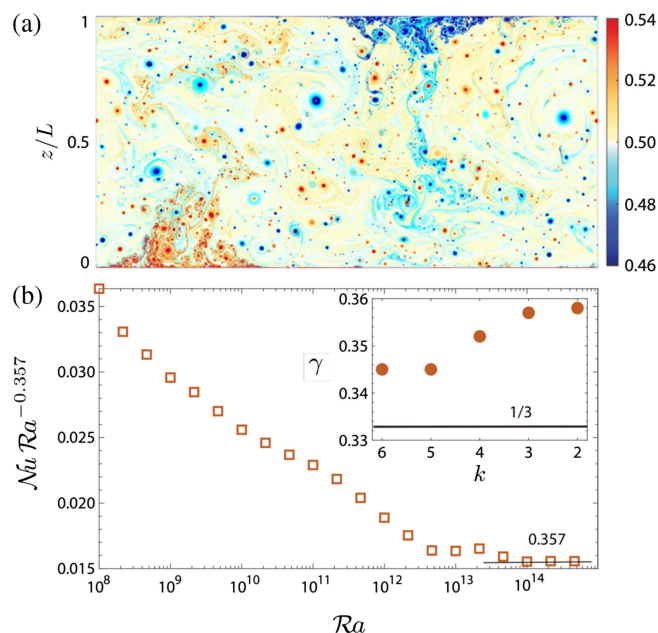


FIG. 20. (a) Snapshot of a 2D DNS at $Ra = 10^{14}$, $Pr = 1$, $\Gamma = 2$, and periodic boundary conditions in the horizontal direction. From Zhu, Mathai *et al.*, 2018. (b) Nu compensated with $Ra^{0.357}$ vs Ra . Inset: the effective scaling exponent γ obtained from a power-law fit $Nu \sim Ra^\gamma$ to the last k data points in the main figure. Adapted from Zhu, Mathai *et al.*, 2019.

that Zhu, Mathai *et al.* (2018, 2019) obeyed the resolution and convergence criteria outlined in Sec. VIII.B. A snapshot of the temperature field for $Ra = 10^{14}$ is shown in Fig. 20(a), while Fig. 20(b) shows $Nu(Ra)$ (in a compensated plot), clearly displaying a transition at around $Ra_c \approx 10^{13}$ from an effective local scaling exponent $\gamma < 1/3$ in $Nu \sim Ra^\gamma$ to $\gamma > 1/3$ and signaling the onset of the ultimate regime. This interpretation of the data of Zhu, Mathai *et al.* (2018) was challenged by Doering, Toppaladoddi, and Wettlaufer (2019), but Zhu, Stevens *et al.* (2019) irrefutably settled this issue and gave four pieces of evidence for the transition toward the ultimate regime in their 2D DNS: (i) They fitted the last k data points, with $2 \leq k \leq 6$ and $10^{13} \leq Ra \leq 4.64 \times 10^{14}$, of their results for $Nu(Ra)$ with an effective power law $Nu \sim Ra^\gamma$. For all cases $\gamma > 1/3$ [see the inset of Fig. 20(b)], which shows the ultimate regime. (ii) They locally measured the effective power-law exponent in the plume ejecting areas of the flow, which for large Ra dominate the overall heat transfer (Reiter, Shishkina *et al.*, 2021), and obtained $Nu_{\text{ejecting}} \sim Ra^{0.38}$ in those areas. (iii) They found a clear logarithmic velocity profile of the Prandtl-von Kármán type for much more than a decade in the kinetic boundary layer, thereby indicating the ultimate regime. (iv) Previously Krug *et al.* (2018), employing the data of Zhu, Mathai *et al.* (2018), found an extended self-similarity behavior of the temperature structure in the kinetic boundary layer (as is typical for fully developed turbulence flow) above the transition at $Ra^* \approx 10^{13}$, while this was absent below the transition.

We note that while the Nusselt number statistically converged in the simulations of Zhu, Mathai *et al.* (2018)

and Zhu, Verschoof *et al.* (2018), the overall Reynolds number, as defined using the root-mean-square velocity fluctuations, has not yet converged, thereby reflecting the challenge of the long convergence times (as measured in large-eddy turnover times) for some flow quantities in 2D RB DNS. Even longer simulations will be necessary to further explore the ultimate regime in 2D RB flow, and also in 3D RB flow, where, as stated in Sec. VIII.A, no ultimate regime has yet been achieved.

D. Can numerical simulations verify and illuminate the subcritical nature of the transition to the ultimate regime?

How can direct numerical simulations be helpful to further illuminate the nature of the ultimate regime and its onset, beyond simply moving toward larger and larger grids and higher and higher Ra? Our answer is similar to what we wrote in Sec. VII.G, in which we suggested subjecting the BLs in RB experiments with $Ra > 10^{11}$ to controlled distortions in order to trigger the onset of the ultimate regime. As explained in the Introduction and in Sec. III.C, with the hypothesis that the onset has a non-normal–nonlinear character, one would expect double-threshold behavior: For large enough Ra and at the same time large enough distortions, one would expect the onset of the transition; in fact, for a given Ra, the earlier the onset is, the larger the distortion. DNSs offer the opportunity to do this in a controlled way and it may numerically be only borderline affordable, in both 2D and 3D DNSs, given that the potential transition regime under investigation is between $Ra = 10^{11}$, where the transition was observed by Chavanne *et al.* (1997), and $Ra = 10^{14}$, where the transition was observed by He, Funfschilling, Bodenschatz, and Ahlers (2012) and He, Funfschilling, Nobach *et al.* (2012) (for both $\Gamma = 1/2$ and $Pr \sim 0.7$).

Even if one does not succeed in finding a distortion that is large enough to trigger a full and sustainable transition to the ultimate regime with its turbulent BL, one may be able to numerically measure the lifetime of the distortion as a function of Ra. Following the ideas of Hof *et al.* (2006) and Avila *et al.* (2011, 2013) [see also the reviews on the non-normal–nonlinear transition mentioned in the Introduction (Grossmann, 2000; Schmid and Henningson, 2001; Kerswell, 2002; Eckhardt *et al.*, 2007; Schmid, 2007; Barkley, 2016; Manneville, 2016; Wu, 2019; Avila, Barkley, and Hof, 2023)], even below onset of the non-normal–nonlinear transition to turbulence of the BL one would expect features of the turbulent state, namely, an increasing lifetime of the distortions with increasing Ra. These lifetimes could be numerically measured as a function of Ra and compared with the situations for pipe flow or channel flow just below onset of the transition to turbulence.

If one succeeds in numerically triggering by some distortion a full and sustainable transition toward the ultimate regime, say, at $Ra = 10^{12}$, it may even be numerically feasible to probe its hysteretic character [cf. Fig. 4(c)] by slowly reducing Ra and wondering when the system would recover in its classical state. However, the running times for such studies may be prohibitively long in DNSs at these high Ra, where the ultimate regime is expected.

IX. ULTIMATE TURBULENCE IN RELATED SYSTEMS

Ultimate turbulence occurs not only in strongly driven RB flow but also in various other related strongly driven wall-bounded flows. In Sec. I we outlined the analogy between the transition to ultimate RB turbulence and the transition to fully developed turbulence in pipe flow, channel flow, and flow along a plate; cf. Fig. 3. In this section we provide further examples, with a focus on thermally driven flows (which are incomplete due to limited space). In addition, we discuss Taylor-Couette (TC) turbulence (see Sec. IX.B) due to the close formal analogy between TC and RB flow.

A. Turbulent convection with centrifugal buoyancy

We began Sec. VII with the consideration that there are three different ways to increase Ra defined in Eq. (4), namely, by increasing the height L of the container or the temperature difference Δ or by optimizing the material properties of the fluid (for example, by decreasing ν and κ). However, from Eq. (4) it becomes clear that there is even a fourth way, namely, increasing the acceleration g . While this is impossible in long-time terrestrial experiments, large accelerations can be achieved in a centrifuge. This is exactly the path proposed and followed by Chao Sun and co-workers at Tsinghua University (Jiang *et al.*, 2020, 2022). The outward centrifugal acceleration in these experiments is much larger than the gravitational acceleration, namely, up to 100 times, so the effect of the gravitational acceleration can be considered small.

The principle of the setup is shown in Figs. 21(a) and 21(b). Two coaxial cylinders are rigidly rotating with an angular velocity ω around the vertical axes of the cylinders, with a fluid in between. The outer cylinder is heated and the inner cylinder is cooled, with a temperature difference Δ between them. Hot, lighter (colder, heavier) fluid then experiences inward centripetal (outward centrifugal) forces. The respective governing equations are similar to Eqs. (1)–(3), with an extra centrifugal acceleration $-\alpha(T - T_0)\omega^2 r \mathbf{e}_r$ and an extra Coriolis acceleration $2\omega \mathbf{u} \times \mathbf{e}_z$ in the Navier-Stokes equation (2). When one neglects the acceleration due to gravitational buoyancy, the extra Coriolis force, and the different geometry with the outer surface being larger than the inner one and both being curved, one can view the modified equations as identical to those of the RB system, with a centrifugal Rayleigh number

$$Ra = \frac{\omega^2(r_o + r_i)\alpha\Delta L^3}{2\kappa\nu}, \quad (153)$$

where $L = r_o - r_i$ is the gap width between the outer cylinder with radius r_o and the inner cylinder with radius r_i and ω is the angular velocity of the rotating setup. Within this approximation the other two control parameters remain as in the traditional RB geometry, namely, the Prandtl number Pr of the fluid and the aspect ratio $\Gamma = H/L$ of the cylindrical setup, where H is the height of the cylinder.

However, without this simplification the system has three additional dimensionless control parameters: The different domain geometry as compared to the original RB setup is quantified by the radius ratio $\eta = r_i/r_o$. Obviously, $r_i < r_o$,

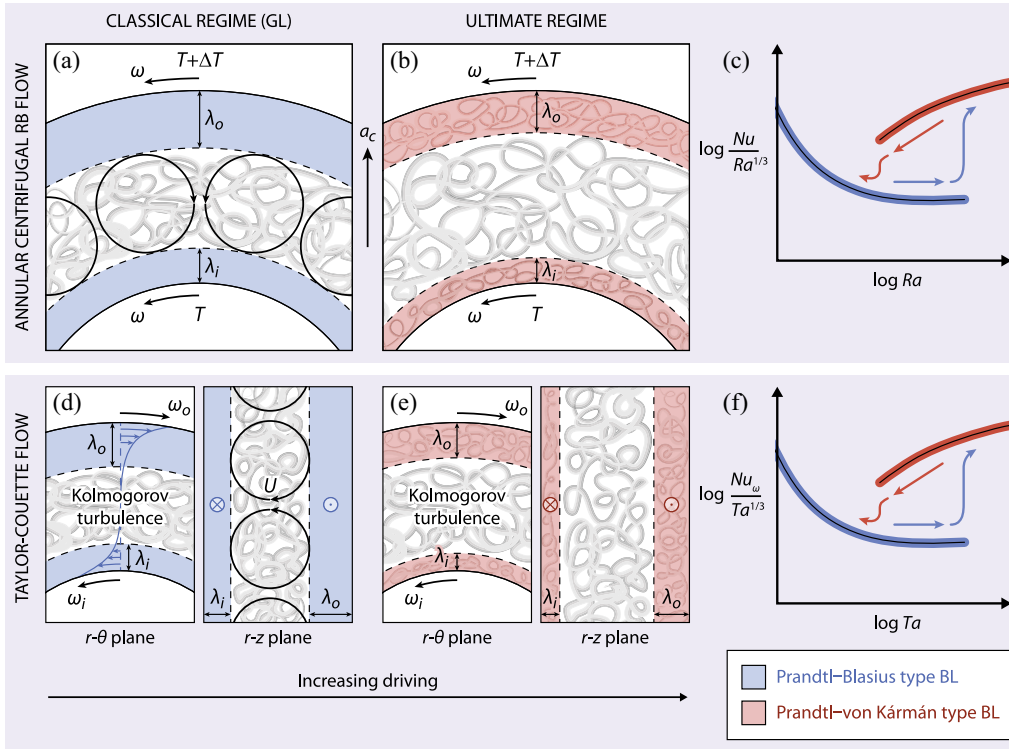


FIG. 21. Flow transitions (a)–(c) for turbulent convection with centrifugal buoyancy and (d)–(f) for Taylor-Couette flow. This depiction is analogous to Fig. 4, which was for turbulent RB flow and plate flow. In turbulent convection with centrifugal buoyancy, the core part of the flow is always turbulent. With increasing centrifugal driving strength [i.e., increasing Ra ; cf. Eq. (153)], the kinetic boundary layers (BLs) change from (a) a laminar Prandtl-Blasius-type BL (blue areas) to (b) a turbulent Prandtl–von Kármán-type BL (red areas). These two cases correspond to two distinct dependences of the heat transport (Nu) vs the thermal driving strength (Ra), which are illustrated in (c) with blue and red lines, respectively. In full analogy with Rayleigh-Bénard flow, Taylor-Couette flow undergoes a transition between (d) laminar and (e) turbulent BLs that have different dependences of the Nusselt number Nu_{ω} (which is the nondimensional angular velocity transport from the inner to the outer cylinder) on the Taylor number (Ta), which are sketched in (f) with blue and red lines, respectively.

which breaks the top-down symmetry of the original RB setup. In a sense this symmetry breaking can be viewed as a kind of non-Oberbeck-Boussinesq effect. In the experiments by Jiang *et al.* (2020, 2022) its value is $\eta = 1/2$. The second new control parameter is the inverse Rossby number

$$Ro^{-1} \equiv 2 \left(\frac{\alpha \Delta (r_o + r_i)}{2L} \right)^{-1/2} = \left(\frac{8}{\alpha \Delta} \frac{1 - \eta}{1 + \eta} \right)^{1/2}, \quad (154)$$

which is a measure of the Coriolis effects compared to the centrifugal effects. The measure depends on the geometry and on $\alpha \Delta$. And the third new control parameter is the original Rayleigh number (4) defined via the gravitational acceleration, which now, however, acts perpendicularly to the mean temperature gradient; we therefore call it Ra_{\perp} . For strong centrifugal acceleration as applicable in the ultimate regime, it has a small effect. Alternatively, as a third parameter one can take the inverse Froude number

$$Fr^{-1} \equiv \frac{2g}{\omega^2 (r_o + r_i)}, \quad (155)$$

which is a measure of the gravitational acceleration compared to the centrifugal acceleration. The main response parameter

remains Nu , which is the nondimensionalized heat flux from the outer to the inner cylinder.

The centrifugal buoyancy setup, therefore, is equivalent to the Rayleigh-Bénard setup under the following three limits (which must all hold): (i) $Fr \rightarrow \infty$ (required for the vanishing gravitational buoyancy term in the Navier-Stokes equation), (ii) $\eta \rightarrow 1$ (needed for the independence of the centrifugal buoyancy term from the radial coordinate r and for the vanishing Coriolis term, which is proportional to Ro^{-1} [cf. Eq. (154)]; for this the boundedness of $\alpha \Delta$ is also required), and (iii) $r_o \rightarrow \infty$ (required for vanishing curvature effects). In any real system, $\eta < 1$, and therefore the Coriolis term is always present; cf. Eq. (154), as well as the radial dependence of the centrifugal acceleration term (which can also be understood as a non-Oberbeck-Boussinesq effect). The gravitational buoyancy term [$\sim Fr^{-1}$; cf. Eq. (155)] also contributes, but only slightly for high rotation rates. The Coriolis force and the gravitational buoyancy provide additional shear to the system, namely, in the horizontal and vertical directions, respectively, which together with the curved surfaces can trigger the onset of the ultimate regime earlier than in the Rayleigh-Bénard system.

Some of the measurements by Jiang *et al.* (2020, 2022) of the Nusselt number in centrifugal buoyancy convection are

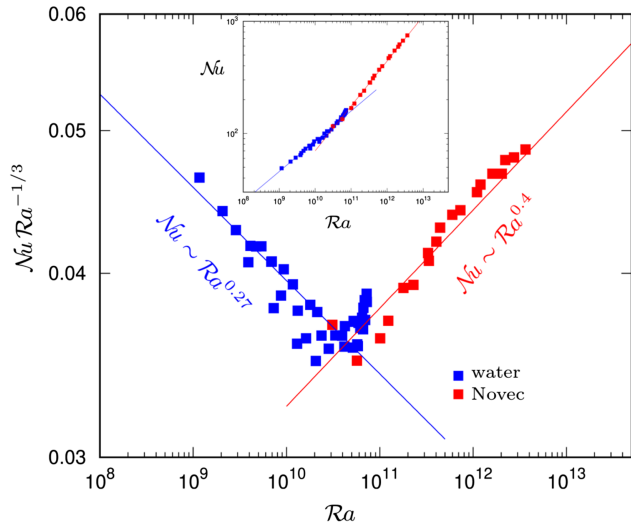


FIG. 22. Transport properties of turbulent convection with centrifugal buoyancy: the Nusselt number (compensated with $Ra^{1/3}$) vs the Rayleigh number in turbulent convection with centrifugal buoyancy for working fluid water ($4.0 \leq Pr \leq 4.3$; blue symbols on the left) and Novec ($10.0 \leq Pr \leq 10.4$; red symbols on the right). With growing Ra , the other control parameter changes almost monotonically from $Fr \approx 8.9$ and $Ro^{-1} \approx 58$ (i.e., $\alpha\Delta \approx 8 \times 10^{-4}$) for $Ra \approx 1.17 \times 10^9$ to $Fr \approx 100$ and $Ro^{-1} \approx 9$ (i.e., $\alpha\Delta \approx 3 \times 10^{-2}$) for $Ra \approx 3.65 \times 10^{12}$. Inset: Nu vs Ra . The transition in the scaling toward the ultimate regime is around $Ra \approx 5 \times 10^{10}$. Data are from Jiang *et al.* (2022).

shown in Fig. 22. At around $Ra \approx 5 \times 10^{10}$ one can identify the transition from the classical regime with $\gamma < 1/3$ to the ultimate regime $\gamma > 1/3$ with an enhanced heat transfer. The ultimate regime extends over more than 2 orders of magnitude in Ra . A power-law fit $Nu \sim Ra^\gamma$ in the regime $Ra > 5 \times 10^{10}$ gives an effective exponent of $\gamma \approx 0.40$ (Jiang *et al.*, 2022). The transition at $Ra \approx 5 \times 10^{10}$ is also seen in the rms temperature fluctuations.

The modified RB equations for centrifugal buoyancy in a cylindrical geometry with $\eta = 1/2$ and periodic boundary conditions in the vertical direction (but assuming $Ra_\perp = 0$ or $Fr = \infty$) were numerically solved by Jiang *et al.* (2020, 2022), Rouhi *et al.* (2021), Wang *et al.* (2022), and Zhong, Wang, and Sun (2023) for various control parameters. Their results accompany the experimental results of Jiang *et al.* (2020, 2022).

What about the shear Reynolds number Re_s around the transition? The largest DNS of Jiang *et al.* (2022) could be completed for $Ra = 4.7 \times 10^{10}$, just around the transition, and for that value $Re_s \approx 400$ was found (for $Pr = 4.3$), so it falls in the range where the transition can be expected. For that Rayleigh number Jiang *et al.* (2022), moreover, found a logarithmic boundary-layer velocity profile for more than 1.5 decades, thereby providing further evidence that the observed transition is indeed the one to the ultimate regime with a turbulent Prandtl-von Kármán BL and, correspondingly, enhanced heat transport.

For detailed discussions of the Coriolis effects in centrifugal buoyancy-driven convection and for further examples of

mixed centrifugal and buoyancy-driven convection with rotation, see Rouhi *et al.* (2021) (though in that paper the numerical simulations are only at the edge of the onset toward the ultimate regime). Again, also for centrifugal buoyancy-driven convection, 3D DNSs in the ultimate regime could not yet be realized.

B. Ultimate Taylor-Couette turbulence

As we later see, as compared to RB turbulence the situation with respect to the achievability of 3D DNS in the ultimate regime is much more favorable for ultimate TC turbulence. Indeed, ultimate TC turbulence could be realized both in 3D DNSs and in controlled experiments; see the review on TC turbulence by Grossmann, Lohse, and Sun (2016). The Taylor-Couette system consists of the flow between two independently rotating coaxial cylinders; see Figs. 21(d) and 21(e). The flow is driven by the centrifugal forces in an outward direction, but incompressibility and the outer cylinder eventually lead to the formation of convection rolls, as in RB flow; see Figs. 21(d) and 21(e). If the outer cylinder is corotating, it can partially or fully stabilize the flow, whereas some counterrotation of the outer cylinder leads to further destabilization; again see the review of Grossmann, Lohse, and Sun (2016).

In addition to the RB system, the TC system has always been a popular approach for developing new concepts in the physics of fluids, be it on linear instabilities (Chandrasekhar, 1953; Drazin and Reid, 1981), the flow organization just above the onset of instabilities (Andereck, Liu, and Swinney, 1986), pattern formation (Cross and Hohenberg, 1993; Fardin, Perge, and Taberlet, 2014), or turbulence (Grossmann, Lohse, and Sun, 2016). Busse (2012) called the RB and TC systems the twins of turbulence research. They share the properties that both of them are closed systems for which exact global balance relations between the driving and the dissipation can be derived and that they are experimentally accessible with high precision, thanks to the simple geometries and symmetries. The two systems in fact enjoy a much deeper formal analogy based on the underlying Navier-Stokes equations. At the onset of the instabilities it was first discovered by Bradshaw (1969), then extended to the fully turbulent regime by Dubrulle and Hersant (2002), Eckhardt, Grossmann, and Lohse (2007a, and 2007b), and Brauckmann, Eckhardt, and Schumacher (2017).

The underlying dynamical equations of TC flow are the Navier-Stokes equation (2), without the buoyancy term but supplemented by the Coriolis acceleration $2\omega \mathbf{u} \times \mathbf{e}_z$, and the continuity equation (1), with no-slip boundary conditions at the inner and outer cylinders and the top and bottom plates. The dimensionless control parameters of the system are the Reynolds number of the inner cylinder $Re_i = r_i(r_o - r_i)\omega_i/\nu$, that of the outer cylinder $Re_o = r_o(r_o - r_i)\omega_o/\nu$, the radius ratio $\eta = r_i/r_o$, and the aspect ratio $\Gamma = L/r_o$. Here $r_{i/o}$ is the radius of the inner (outer) cylinder, $\omega_{i/o}$ are the respective angular velocities, and L is the height of the cylinder.

Eckhardt, Grossmann, and Lohse (2007b) determined that the analogy between TC and RB flow becomes visible in the best way when the control parameters are taken as the Taylor number

$$\text{Ta} = \frac{(1 + \eta)^4 (r_o - r_i)^2 (r_i + r_o)^2 (\omega_i - \omega_o)^2}{64\eta^2 \nu^2} \quad (156)$$

and the rotation ratio $-\omega_o/\omega_i$ or, alternatively, the inverse Rossby number

$$\text{Ro}^{-1} = \frac{2\omega_o d}{|\omega_i - \omega_o| r_i} = 2 \frac{1 - \eta}{\eta} \frac{\omega_o/\omega_i}{|1 - \omega_o/\omega_i|} \quad (157)$$

and the main response parameter as a Nusselt number

$$\text{Nu}_\omega \equiv \frac{J^\omega}{J_{\text{lam}}^\omega} \equiv \frac{r^3 (\langle u_r \omega \rangle_{A,t} - \nu \partial_r \langle \omega \rangle_{A,t})}{J_{\text{lam}}^\omega}, \quad (158)$$

with the angular velocity $\omega = u_\phi/r$. In Eq. (158) $\langle \dots \rangle_{A,t}$ signals averaging over time and the area with constant distance from the axis. The reason for Nu_ω being such a relevant response parameter is that the conserved transport quantify in TC flow is the angular velocity flux J^ω from the inner to the outer cylinder. In the definition (158) it was nondimensionalized with the angular velocity flux $J_{\text{lam}}^\omega = 2\nu r_i^2 r_o^2 (\omega_i - \omega_o) / (r_o^2 - r_i^2)$ in the laminar case, as with RB flow, where the heat flux as a conserved quantity is nondimensionalized with the conductive heat flux in order to obtain the Nusselt number; cf. Eq. (11). With these definitions, the relation $\text{Nu}(\text{Ra})$ in RB flow directly corresponds to $\text{Nu}_\omega(\text{Ta})$ in TC flow.

The second key response parameter of the turbulent TC system is the degree of turbulence of the “wind” in the gap (of width $r_o - r_i$) between the cylinders, which measures the strength of the secondary flows, i.e., the r and z components of the velocity field (u_r and u_z). In a nondimensional way it is expressed as the wind Reynolds number

$$\text{Re} = \frac{\sigma_{u_w} (r_o - r_i)}{\nu}, \quad (159)$$

where σ_{u_w} is the standard deviation of either the radial or axial velocity. The wind Reynolds number in TC flow [Eq. (159)] directly corresponds to the wind Reynolds number Re in RB flow. Similarly, the exact relation (13) for the energy dissipation rate ϵ_u in RB flow has the exact relation

$$\epsilon_u - \epsilon_{u,\text{lam}} = \frac{\nu^3}{(r_o - r_i)^4} (\text{Nu}_\omega - 1) \text{Ta} \text{Pr}_{\text{geo}}^{-2} \quad (160)$$

as an analogy in TC flow. In Eq. (160) $\text{Pr}_{\text{geo}} = (1 + \eta)^4 / (16\eta^2)$ is a geometric factor (and not a material property like Pr in RB flow) and $\epsilon_{u,\text{lam}}$ is the kinetic energy dissipation rate of laminar TC flow in the limit of $\text{Re}_{i,o} \rightarrow 0$.

The main difference between TC and RB flow may be that in TC there is no symmetry between the inner and the outer cylinder ($r_i < r_o$ or $\eta < 1$), as there is in RB in the Oberbeck-Boussinesq case, where symmetry between the top and bottom plates holds. In a sense, just as for turbulent convection with centrifugal buoyancy (Sec. IX.A), this symmetry breaking can be seen as a kind of non-Oberbeck-Boussinesq effect.

In the classical regime, the boundary layer is of the laminar Prandtl-Blasius type, leading to an effective Nu_ω versus Ta

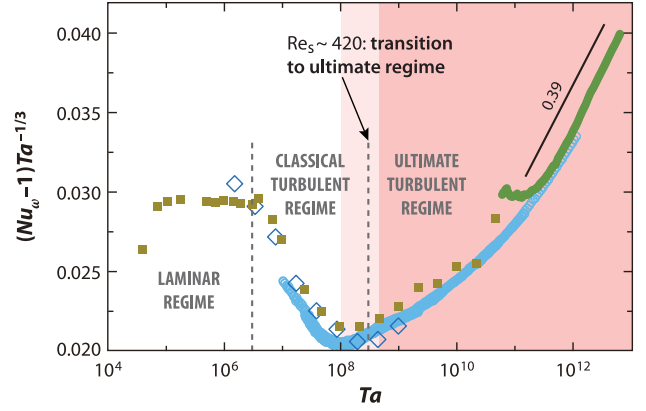


FIG. 23. Transport properties of Taylor-Couette flow: the Nusselt number Nu_ω (compensated with $\text{Ta}^{1/3}$) vs Ta for a radius ratio $0.71 \leq \eta \equiv r_i/r_o \leq 0.72$. The filled green circles represent experimental data from van Gils, Huisman *et al.* (2011) and van Gils *et al.* (2012) (the filled green circles for the smallest Ta reflect not the flow properties but an artifact of the torque sensor that is used to determine Nu_ω and that does not work properly in that regime), the open blue circles are experimental data points given by Lewis and Swinney (1999), the brown squares represent numerical data from Ostilla-Mónico *et al.* (2014a, 2014b), and the open blue diamonds depict numerical data by Brauckmann and Eckhardt (2013). The transition from the classical regime (white area) to the ultimate regime (red area) occurs at around $\text{Ta} = 2 \times 10^8$, where the shear Reynolds number is around $\text{Re}_s \approx 420$. Adapted from Grossmann, Lohse, and Sun, 2016.

scaling exponent $\gamma \leq 1/3$. However, when the shear Reynolds number Re_s is around 420, this laminar-type boundary layer can undergo a non-normal–nonlinear instability to become of the turbulent Prandtl–von Kármán type; see Fig. 23. This onset of the ultimate TC regime occurs at around $\text{Ta} \approx 2 \times 10^8$ (van Gils, Huisman *et al.*, 2011; Huisman *et al.*, 2012; Ostilla-Mónico *et al.*, 2014b; Grossmann, Lohse, and Sun, 2016); cf. Fig. 24(a). Beyond that the effective Nu_ω versus Ta scaling exponent is $\gamma \approx 0.38 > 1/3$, as in the ultimate RB regime. As expected for the ultimate TC regime, the mean velocity profile in the BLs is logarithmic, as confirmed by Huisman *et al.* (2013) in experiments [cf. Fig. 24(b)] and by Ostilla-Mónico *et al.* (2014a, 2014b) in direct numerical simulations.

One may wonder why the ultimate regime can be reached more easily in TC flow than in RB flow in both experiment and DNS. The simple reason is that the mechanical driving in TC flow is so much more efficient than the thermal driving in RB flow that the required shear Reynolds numbers to develop the non-normal–nonlinear instability can be reached relatively easily.

Finally, we note that for TC flow there is also a mathematically strict upper bound on the transport (Doering and Constantin, 1994), namely, when translated to Ta and Nu_ω as the control and response parameters, $\text{Nu}_\omega \lesssim \text{Ta}^{1/2}$, which is in direct analogy with the upper bounds $\text{Nu} \lesssim \text{Ra}^{1/2}$ discussed for RB flow in Sec. IV. Zhu, Verschoof *et al.* (2018) experimentally and numerically realized this asymptotic ultimate scaling exponent 1/2 in TC flow with rough walls (such that pressure drag is dominant); these experiments can

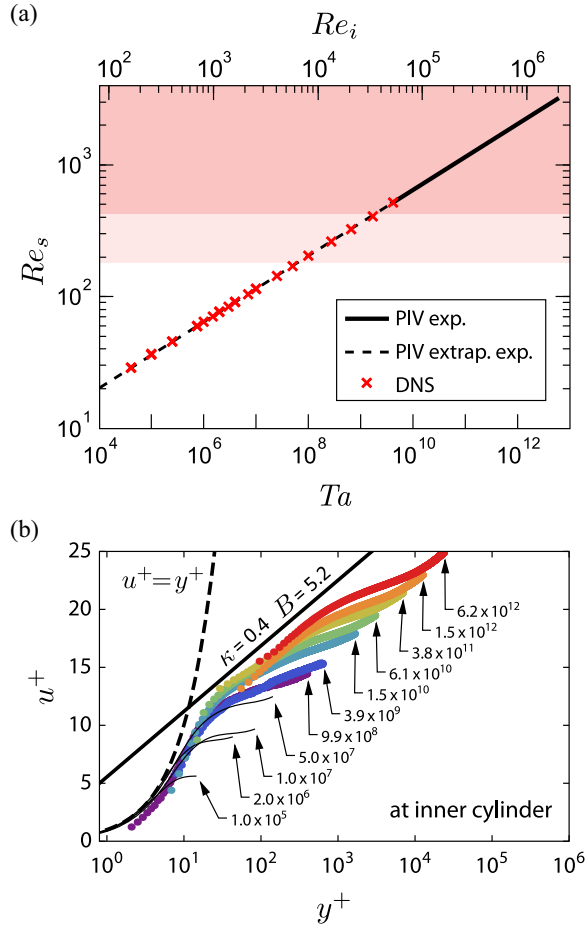


FIG. 24. Taylor-Couette flow. (a) Shear Reynolds number Re_s vs the Taylor number Ta from DNS and from particle image velocimetry (PIV) experiments. We also give Re_i (upper axis); the outer cylinder is at rest ($Re_o = 0$). The effective scaling exponent is close to $1/4$, as $Re \sim Ta^{1/2}$ and $Re_s \sim Re^{1/2}$. The transition from the classical regime to the ultimate regime is expected around the light red band for $Re_s \approx 420$. From [van Gils *et al.*, 2012](#). (b) Mean velocity profiles in so-called plus units $u^+(y^+)$ at the inner cylinder for various Ta . Also shown is the logarithmic Prandtl–von Kármán profile $u^+(y^+) = \kappa_K^{-1} \log(y^+) + B$ with the von Kármán constant $\kappa_K = 0.4$ ([Pope, 2000](#)). Adapted from [Huisman *et al.*, 2013](#).

be seen in analogy with the asymptotic ultimate scaling exponent $1/2$ in RB flow with roughness on all scales [cf. [Zhu, Stevens *et al.* \(2019\)](#)], which we discuss in Sec. IX.C. For further details on ultimate TC turbulence, see the turbulent Taylor-Couette review by [Grossmann, Lohse, and Sun \(2016\)](#).

C. Rayleigh-Bénard turbulence with pronounced plate roughness

As discussed in Sec. VI.C, some roughness of the plates and sidewalls of the RB container is unavoidable. To better understand the effect of roughness, measurements and numerical simulations in RB containers with pronounced and controlled plate roughness have been performed. Strictly speaking, such systems are different from RB systems, as the boundary conditions are deliberately different; therefore, we discuss them in this section on related systems.

Large isothermal obstacles inside a convection container can affect the heat transport in the system since in that case the flow is a complicated mixture of two differently scaling convective processes RB convection and vertical convection, where horizontal and vertical surfaces, respectively, are isothermal and therefore are additional heat sources or sinks; these flow configurations are beyond the scope of this review. More interesting is that roughness of the heated and cooled plates can significantly alter the mean heat and momentum transport, i.e., Nu and Re , and even their scaling relations with the main control parameter Ra . We discuss this further later in the review.

Most of the RB convection studies for containers with rough plates have been conducted for regular roughness, which is determined by a single or only a few roughness scales. An increase of Nu compared to the case of smooth plates is usually reported there if the roughness scale is about as large or larger than the BL thickness in the smooth case. One observes an increase of either the effective scaling exponent γ in $Nu \sim Ra^\gamma$ ([Roche, Castaing, Chabaud, and Hébral, 2001](#); [Qiu, Xia, and Tong, 2005](#); [Stringano, Pascazio, and Verzicco, 2006](#); [Tisserand *et al.*, 2011](#); [Salort *et al.*, 2014](#); [Liot *et al.*, 2016, 2017](#); [Xie and Xia, 2017](#); [Jiang *et al.*, 2018](#); [Xu *et al.*, 2018](#)) or the prefactor in this relation ([Shen, Xia, and Tong, 1996](#); [Du and Tong, 2000](#); [Wei and Ahlers, 2014](#); [Joshi *et al.*, 2017](#)).

[Roche, Castaing, Chabaud, and Hébral \(2001\)](#), based on their measurements in a cylindrical container with V-shape grooves that covered the entire interior surface of the container, plates, and sidewalls, found a roughness-induced increase of the scaling exponent $\gamma \approx 0.5$ in the $Nu \sim Ra^\gamma$ scaling relation. With growing Ra the BLs become thinner, and eventually their thickness reaches the roughness height. [Roche, Castaing, Chabaud, and Hébral \(2001\)](#) explained that when the BLs get sufficiently thin, the roughness imposes a new length scale to the BLs, which is a roughness height independent of Re . This makes the friction coefficient independent of Re too ([Roche, Castaing, Chabaud, and Hébral, 2001](#)), as in the asymptotic ultimate regime, i.e., without logarithmic corrections, which leads to the increased scaling exponent $\gamma \approx 1/2$ in their experiment. The situation is analogous to the frictional drag in a pipe flow in the fully rough case, which becomes independent of the Reynolds number ([Nikuradse, 1933](#); [Chung *et al.*, 2021](#)).

Three-dimensional DNS ([Wagner and Shishkina, 2015](#); [Emran and Shishkina, 2020](#); [Belkadi *et al.*, 2021](#)) and experiments ([Rusaouën *et al.*, 2018](#)) showed that, with increasing Ra , the scaling exponent γ first remains unaffected by the regular monoscale plate roughness, then increases, and finally stagnates again to the level in the smooth case (with the scaling prefactor being increased). In addition, a two-dimensional DNS by [Zhu *et al.* \(2017\)](#) for Ra up to 10^{12} showed that with increasing Ra , the local effective scaling exponent $\gamma = d \log Nu / d \log Ra$ is first about $1/3$, grows to $\gamma \approx 1/2$, and then falls back down to $\gamma \approx 1/3$. Therefore, the regime with a local effective exponent of $\gamma \approx 1/2$ cannot be interpreted as the ultimate regime or as a transition to the ultimate regime; it is instead an

intermediate regime,⁹ triggered by regular roughness, where the thermal BLs are perturbed, leading to more thermal plume shedding and having a large effective plate area. For larger Ra when the effective exponent is $\gamma = 1/3$ again, the thermal and kinetic BLs are thinner than the roughness length scale and follow the roughness structure but are not turbulent. For even larger Ra one still can expect a transition to the ultimate regime provided that the shear Reynolds number has become large enough and that the distortions are sufficient to trigger the transition. Note that in RB convection with rough plates, as in the case of smooth plates, the scaling exponent γ cannot be larger than $1/2$ when $Ra \rightarrow \infty$ (Goluskin and Doering, 2016).

An increase in the scaling exponent γ only for the case of irregular (power-law-distributed) roughness but not for regular (periodic) roughness was found experimentally by Ciliberto and Laroche (1999). This result was consistent with an idea of Villiermaux (1998), who proposed a significant increase of γ , which depends on the surface's fractal dimension if the spectrum of the typical roughness length scales is sufficiently broad. Later a DNS by Zhu, Stevens *et al.* (2019) also supported the hypothesis that the larger number of roughness scales extends the Ra range with increased γ . Therefore, one might expect that there exists an infinite spectrum of the roughness length scales that for all sufficiently large Ra leads to an increased scaling exponent γ for the rough plates compared to that for the smooth plates.

For completeness, we also note that the plate roughness can not only increase Nu but also decrease it, as demonstrated in experiments (Tisserand *et al.*, 2011), 2D DNSs (Shishkina and Wagner, 2011), 3D DNSs (Stringano, Pascazio, and Verzicco, 2006; Wagner and Shishkina, 2015; Zhang *et al.*, 2018; Emran and Shishkina, 2020), and large-eddy simulations (Foroozani *et al.*, 2019). In that case, the fluid stagnates in the gaps between the roughness elements, and this leads in general to thicker thermal BLs and smaller overall heat transport in the system. However, the problem involving heat transport reduction induced by the plates' roughness becomes irrelevant for high Ra, and therefore is irrelevant to the ultimate regime in RB convection.

D. Homogeneous Rayleigh-Bénard convection

The asymptotic ultimate regime can best be achieved by fully eliminating all effects from the BLs in order to create the conditions assumed in the model of Spiegel (1971) or regime IV'_ℓ of GL theory, i.e., $\epsilon_u \sim U^3/L$ and $\epsilon_\theta \sim U\Delta^2/L$, without any viscosity or thermal diffusivity entering. In experiments

⁹2D lattice Boltzmann simulations by Toppaladoddi, Succi, and Wettlaufer (2017) for $4 \times 10^6 \leq Ra \leq 3 \times 10^9$ and a fixed roughness height and varying roughness wavelengths λ of a monoscale plate roughness showed that Nu can scale as $\sim Ra^{0.48}$ if for each Ra one chooses the optimal $\lambda(Ra)$ that maximizes Nu. This optimal $\lambda(Ra)$ gradually decreases with growing Ra. However, when fixing the roughness wavelength λ and further increasing Ra, the scaling exponent decreases again to a value $\gamma \leq 1/3$, as indeed observed in 2D DNSs by Zhu *et al.* (2017) and Zhu, Stevens *et al.* (2019), in 3D DNSs by Emran and Shishkina (2020), and in experiments by Rusaouën *et al.* (2018).

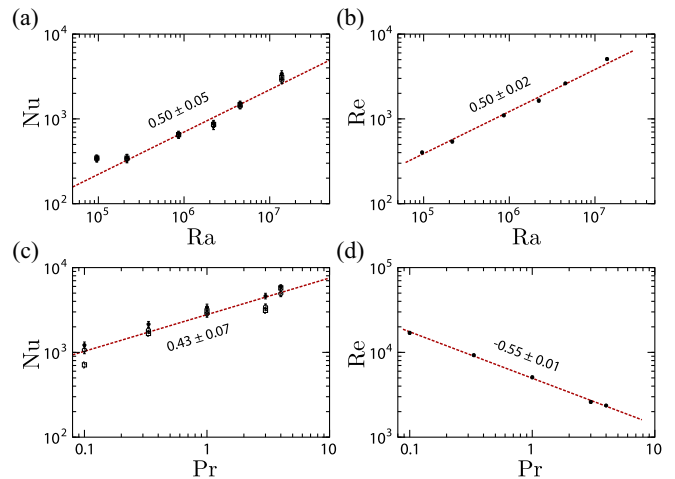


FIG. 25. DNS results for $Nu(Ra, Pr)$ and $Re(Ra, Pr)$ for homogeneous RB convection. Adapted from Calzavarini *et al.*, 2005.

this is nontrivial, but nonetheless approximately possible, as later discussed. In numerical simulations this can be achieved relatively easily by simulating so-called homogeneous RB, in which the top- and bottom-temperature boundary conditions have been replaced by periodic ones, with an unstratified temperature gradient imposed (Lohse and Toschi, 2003; Calzavarini *et al.*, 2005). Indeed, in simulations of such a flow the scaling exponent of the asymptotic ultimate regime have been realized; cf. Fig. 25. Schmidt *et al.* (2012) showed that this can be achieved in RB flow even in a cylinder in which only the vertical, axial direction is homogeneous. Note that in this type of flow (be it homogeneous in all directions or only in the vertical, axial one) exponentially growing (in time) solutions are possible; i.e., there are no mathematically strict upper bounds for Nu (Calzavarini *et al.*, 2006; Schmidt *et al.*, 2012). In the numerical simulations, however, the exponentially growing modes nonlinearly couple with each other and lose their energy in such a way that the heat flux does not grow beyond all bounds.

Another effective realization of asymptotic ultimate turbulence can be achieved in numerical simulations by introducing permeable walls in the vertical direction, as done by Kawano *et al.* (2021), who set the vertical component of the velocity at the top and bottom surfaces as proportional to the pressure fluctuations: $u_z \propto (p'/\rho)/u_{\text{ff}}$. With increasing permeability, the critical Ra_c for the onset of convection gradually reduces, and so does Ra^* for the onset of the ultimate regime. For $Pr = 1$, Kawano *et al.* (2021) observed a transition of the scaling exponent γ in $Nu \sim Ra^\gamma$ from $\gamma \approx 1/3$ to $1/2$ at $Ra \approx 10^7$. Thus, although the thermal BLs are still present at the plates, there is no dramatic change in the vertical velocity there, which makes the effect of the viscosity in general negligible, particularly near the plates.

In experiments, homogeneous turbulence can be achieved only approximately, as there are always BLs. However, one can measure the heat flux far from the heated or cooled plates in order to approximately realize homogeneous turbulence in the vertical direction. This route was followed by Perrier, Morat, and LeMouel (2002) and Gibert *et al.* (2006, 2009), who used a vertical channel with wide entrance and exit

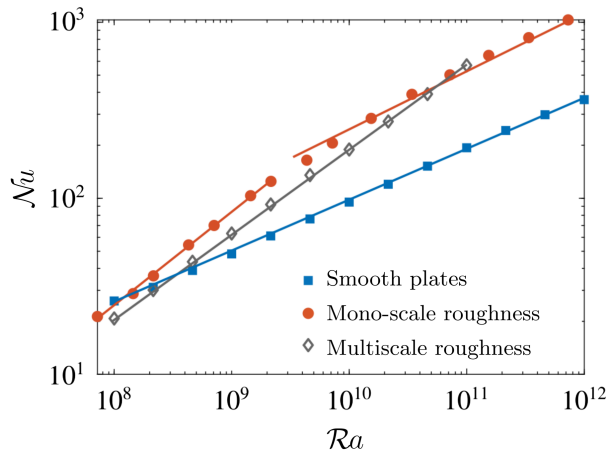


FIG. 26. Nu as a function of Ra for smooth plates and plates with monoscale or multiscale roughness. In the smooth case, the scaling exponent γ in $Nu \sim Ra^\gamma$ is $\gamma = 0.29 \pm 0.01$. For multiscale roughness, $\gamma = 0.49 \pm 0.02$. For monoscale roughness, an increased γ can be observed only in a restricted Ra range; for larger Ra , γ stagnated to that in the smooth case. In the monoscale case, sinusoidal roughness elements of the same height ($L/10$) were considered. In the multiscale case, sinusoidal roughness includes roughness elements with heights $L/10$, $L/20$, and $L/40$. Adapted from [Zhu, Stevens *et al.*, 2019](#).

sections that avoided the influence of the thermal BLs on the flow, and indeed achieved the asymptotic ultimate scaling relations $Nu \sim Ra^{1/2}$ and $Re \sim Ra^{1/2}$ in this way. The operating fluids were air in the work of [Perrier, Morat, and LeMouel \(2002\)](#) and water in the work of [Gibert *et al.* \(2006, 2009\)](#). A similar approach, but with the density gradients created by concentration differences and not temperature differences and thus for a much larger Pr , was followed by [Cholemani and Arakeri \(2005, 2009\)](#) and [Pawar and Arakeri \(2016\)](#), who drove the flow by an unstable density difference across the ends of a pipe, again achieving $Nu \sim Ra^{1/2}$ and $Re \sim Ra^{1/2}$. We note that even the local convective heat flux in the bulk of RB convection can be seen as homogeneous convection, and indeed for such local heat flux [Shang *et al.* \(2003\)](#) and [Shang, Tong, and Xia \(2008\)](#) measured $Nu_{\text{local}} \sim Ra^{1/2}$, which was confirmed in simulations by [Lakkaraju *et al.* \(2012\)](#).

E. Other convective systems

There are various further convective and thermally driven flow systems in which ultimate turbulence can occur. In this section, we provide further details and references on horizontal convection (HC) and internally heated convection (IHC).

In HC ([Hughes and Griffiths, 2008](#)) the flow is driven by differential heating along one horizontal plate; here we restrict ourselves to HC in a closed fluid-filled container, with one side of the horizontal plate heated and the other side cooled, with a distance L between the heated and cooled parts. For such a closed system, GL theory for RB flow can straightforwardly be extended by building on the balance relations for the kinetic energy dissipation rate ϵ_u and the thermal dissipation rate ϵ_θ . These are different for HC than for RB

convection but can again be straightforwardly derived from the underlying dynamical equations (1)–(3) with the appropriate boundary conditions for HC. This was done by [Shishkina, Grossmann, and Lohse \(2016\)](#). [Shishkina and Wagner \(2016\)](#), [Shishkina \(2017\)](#), and [Reiter and Shishkina \(2020\)](#) provided DNSs of HC in the laminar and classical regimes that were consistent with the predictions of the generalized GL theory for HC of [Shishkina, Grossmann, and Lohse \(2016\)](#). Their theory also predicted an ultimate regime for HC. The mechanism is the same as in strongly driven RB flow, pipe or channel flow or flow over a plate (see Fig. 4), or turbulent convection with centrifugal buoyancy or TC flow (see Fig. 21): a boundary layer along a plate or a sidewall becomes so strongly sheared that it undergoes the non-normal–nonlinear transition from laminar-type Prandtl–Blasius BL flow to turbulent-type Prandtl–von Kármán BL flow (“ultimate HC”), typically around a shear Reynolds number of $Re_s \approx 420$. However, in the present DNS of HC one is far from that regime, as thermal driving in the HC configuration with its only local heating and cooling is even less efficient than in the RB configuration. We finally also note that the scaling exponent γ in a rigorous upper bound $Nu \lesssim Ra^\gamma$ for HC is $\gamma = 1/3$ ([Siggers, Kerswell, and Balmforth, 2004](#)), i.e., significantly smaller than in RB convection.

Yet another convective system is IHC ([Goluskin, 2016](#)), where the flow is heated not from the walls but by thermal absorption in the bulk. IHC flows can be seen as homogeneous RB flows, and indeed the asymptotic ultimate scaling relations obtained in IHC ([Lepot, Aumaître, and Gallet, 2018](#); [Bouillaut *et al.*, 2019](#)) show the expected scaling relations, including the Prandtl number dependences $Nu \sim Ra^{1/2} Pr^{1/2}$ and $Re \sim Ra^{1/2} Pr^{-1/2}$ ([Miquel *et al.*, 2020](#)). [Wang, Lohse, and Shishkina \(2021\)](#) theoretically and numerically treated the case of homogeneous internal heating. They found that the main control parameter was the strength of the thermal driving of the bulk (in dimensionless form called the Rayleigh–Roberts number) and that the main response parameter was the average mean temperature that develops in the closed container. Again GL theory can be generalized to this case, and [Wang, Lohse, and Shishkina \(2021\)](#) did so. For strong enough driving the shear BLs along the plates and sidewall can again undergo the non-normal–nonlinear transition from laminar-type Prandtl–Blasius BL flow to turbulent-type Prandtl–von Kármán BL flow (“ultimate IHC”), where the average mean temperature depends more strongly on the driving strength. For details and DNSs on this problem, see [Wang, Lohse, and Shishkina \(2021\)](#).

X. CONCLUSIONS AND OUTLOOK

We started this review by discussing the consequences of the seminal insight that the onset of instabilities in various shear flows like pipe or channel flow or the flow along a plate is of non-normal–nonlinear character and, following [Roche \(2020\)](#) and [Lohse and Shishkina \(2023\)](#), argued that the onset of the ultimate regime of RB flow also has this character, as the boundary layers are strongly sheared through the wind of turbulence. This point was elaborated

in Sec. III.C. Based on this idea, we then tried to reconcile the various experimental and numerical findings on the onset of the ultimate regime; see, in particular, Sec. VII.F. The crucial insight is that the various results on the onset Rayleigh number Ra^* of the ultimate regime of RB turbulence do not necessarily contradict each other: first because Ra^* depends on the other two control parameters of the RB system, i.e., on Pr and on the aspect ratio Γ , and second because of the intrinsic character of such non-normal–nonlinear instability. It has no sharp onset but can occur in an entire range of the Rayleigh number, depending on even small distortions of the systems and its history, and it is subcritical and hysteretic.

Insights about the non-normal–nonlinear character of the onset of instabilities in shear flows in the late 1980s and early 1990s (Boberg and Brosa, 1988; Farrell, 1988; Farrell and Ioannou, 1993; Reddy and Henningson, 1993; Reddy, Schmid, and Henningson, 1993; Trefethen *et al.*, 1993) heralded a new era of creative experiments, numerical simulations, and theoretical and mathematical analyses on shear flows; see the reviews by Barkley (2016), Manneville (2016), Wu (2019), and Avila, Barkley, and Hof (2023). One key idea here has been to trigger the instabilities with controlled distortions and then measure the spreading and/or the lifetime of the distortion. Another line of research has been to study the hysteretic character of the transition. Analogous experiments, numerical simulations, and theoretical analyses should be done for RB flow and related systems. In Secs. VII.G and VIII.D we made some suggestions for such new experiments and numerical simulations, including detailed local flow visualizations. We foresee a boost of new activity along these lines that will either further establish the non-normal–nonlinear character of the transition to ultimate turbulence in RB flow and related systems for which this review has given so much evidence or falsify it.

One first result along this line is shown in Fig. 27. To show the hysteretic character of the transition toward the ultimate regime in Taylor-Couette flow (Huisman *et al.*, 2012), starting in the classical regime Luuk Blaauw and Sander G. Huisman (University of Twente) first slowly increased the driving strength Ta up to a sudden jump in the transport property Nu_ω to a higher value. The jump occurred at a nonreproducible value of Ta in a range of Ta between 2.5×10^8 and 3.5×10^8 ; see the light red regime in Fig. 27. When slowly reducing Ta again, Nu_ω does not jump back to the values for which the system underwent the transition, but instead stays at a higher value (the green curves in Fig. 27). Both phenomena support the non-normal–nonlinear nature of the transition. It was doubled-checked that the hysteretic phenomena are not caused by the torque sensor, which is used to deduce Nu_ω , but rather that they are actually a property of the flow, as the same features of the transition are also seen in measurements of the Reynolds number using laser Doppler velocimetry. We note that, in addition to the question as to whether the flow has turbulent-type BLs above the transition or laminar-type BLs below the transition, the number of vertically stacked Taylor rolls can change (Huisman *et al.*, 2014), which presumably is the reason why Nu_ω does not return to the value it had prior to the transition

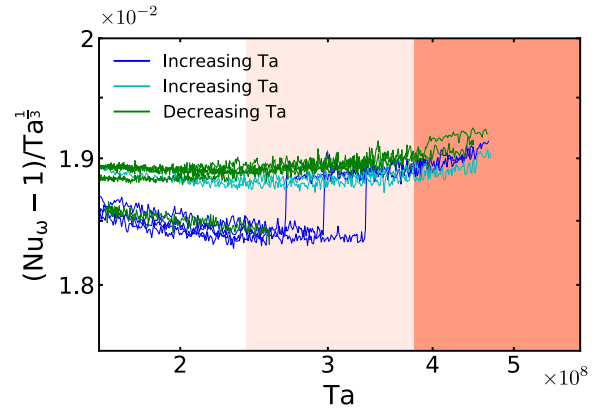


FIG. 27. $Nu_\omega - 1$ ($\approx Nu_\omega$ compensated with the classical scaling $Ta^{1/3}$) vs Ta as obtained in recent measurements by Luuk Blaauw and Sander G. Huisman in the Twente Turbulent Taylor-Couette facility (van Gils, Bruggert *et al.*, 2011; van Gils, Huisman *et al.*, 2011). The measurements reveal the hysteretic character of the transition toward the ultimate regime. For the dark and light blue curves Ta is slowly increasing (achieved by slowly heating the liquid and thus decreasing the kinematic viscosity), while for the green ones it is slowly decreasing (achieved by slowly cooling the liquid). The red region shows the ultimate regime, whereas the light red region shows the Ta range in which the transition to the ultimate regime can happen.

into the ultimate regime. To settle this question, rather than focusing on global response parameters, more work on the visualization of the local flow is necessary.

We also suggest further mathematically studying the Orr-Sommerfeld operator and properties of the associated non-normal operators for RB convection and related locally sheared thermal convection systems. If the eigenvalue analysis cannot predict the onset of turbulence and the ultimate regime, then how can this onset be mathematically identified and predicted in other ways? Can one give quantitative estimates with this respect? Indeed, as we saw regarding the strict upper bounds for the heat transport of Sec. IV, RB flow is a good example in which mathematical analysis goes hand in hand with experiments, numerical simulations, and theory.

Accurate and well-resolved direct numerical simulations for even more extreme parameters than have been studied to date are desired. As we discussed (Shishkina, 2021; Ahlers *et al.*, 2022), the aspect ratio $\Gamma \sim 1$ (to be more precise, close to $1/2$) is optimal in order to achieve the ultimate regime, and performing experiments or numerical simulations with small Γ is not the best or easiest pathway toward ultimate turbulence.

Finally, we emphasize the universality and generality of the approach outlined in this review; it is a versatile recipe applicable to any wall-bounded turbulent flow, be it Rayleigh-Bénard convection, turbulent convection with centrifugal buoyancy, double-diffusive convection, Taylor-Couette flow, pipe or channel flow, horizontal convection, vertical convection, internally heated convection, penetrative convection, or the flow in a stratified inclined duct. The first part of the approach was summarized in Fig. 5(c), namely, the generalized Grossmann-Lohse theory as described in Sec. III. With this the transport properties in the classical

regime, i.e., for not too strong driving so that the boundary layers are still of the Prandtl-Blasius type, can be obtained. The second part of the approach makes note of the fact that for strong enough driving the laminar Prandtl-Blasius-type boundary layers must become unstable and undergoes a transition to a turbulent boundary layer of the Prandtl-von Kármán type. We hypothesized that the nature of this instability is of the non-normal-nonlinear type, i.e., sub-critical; it has no sharp onset but can occur in a certain range of control parameters. In Sec. V we proposed a scaling model for the ultimate regime in RB convection, which can be understood as an extension of the model of Grossmann and Lohse (2011) to the case of large Prandtl numbers. In the research on wall-bounded turbulent flows, interesting times are ahead that will help us to better understand the details of the non-normal-nonlinear transition to the ultimate regime, as well as the ultimate regime itself.

ACKNOWLEDGMENTS

Science is a collective activity. The scientific insights in this review have been gained over more than three decades together with our colleagues, postdocs, doctoral students, and students, and we thank them for all of their work and contributions, and for the stimulation and intellectual pleasure we have enjoyed while working together on this wonderful problem. We particularly thankfully acknowledge all colleagues who have made their experimental and numerical data available to us and to the entire community, as well as those who gave us valuable feedback on the manuscript. We also thank Dennis van Gils for drawing and improving most of the figures.

REFERENCES

- Ahlers, G., 1974, “Low-Temperature Studies of the Rayleigh-Bénard Instability and Turbulence,” *Phys. Rev. Lett.* **33**, 1185.
- Ahlers, G., 2000, “Effect of sidewall conductance on heat-transport measurements for turbulent Rayleigh-Bénard convection,” *Phys. Rev. E* **63**, 015303.
- Ahlers, G., E. Bodenschatz, D. Funfschilling, S. Grossmann, X. He, D. Lohse, R. Stevens, and R. Verzicco, 2012, “Logarithmic Temperature Profiles in Turbulent Rayleigh-Bénard Convection,” *Phys. Rev. Lett.* **109**, 114501.
- Ahlers, G., E. Bodenschatz, D. Funfschilling, and J. Hogg, 2009, “Turbulent Rayleigh-Bénard convection for a Prandtl number of 0.67,” *J. Fluid Mech.* **641**, 157–167.
- Ahlers, G., E. Bodenschatz, and X. He, 2014, “Logarithmic temperature profiles of turbulent Rayleigh-Bénard convection in the classical and ultimate state for a Prandtl number of 0.8,” *J. Fluid Mech.* **758**, 436–467.
- Ahlers, G., E. Bodenschatz, and X. He, 2017, “Ultimate-state transition of turbulent Rayleigh-Bénard convection,” *Phys. Rev. Fluids* **2**, 054603.
- Ahlers, G., E. Brown, F. F. Araujo, D. Funfschilling, S. Grossmann, and D. Lohse, 2006, “Non-Oberbeck-Boussinesq effects in strongly turbulent Rayleigh-Bénard convection,” *J. Fluid Mech.* **569**, 409–446.
- Ahlers, G., E. Calzavarini, F. F. Araujo, D. Funfschilling, S. Grossmann, D. Lohse, and K. Sugiyama, 2008, “Non-Oberbeck-Boussinesq effects in turbulent thermal convection in ethane close to the critical point,” *Phys. Rev. E* **77**, 046302.
- Ahlers, G., D. Funfschilling, and E. Bodenschatz, 2009, “Transitions in heat transport by turbulent convection at Rayleigh numbers up to 10^{15} ,” *New J. Phys.* **11**, 123001.
- Ahlers, G., D. Funfschilling, and D. Lohse, 2011, “Addendum: Transitions in heat transport by turbulent convection at Rayleigh numbers up to 10^{15} ,” *New J. Phys.* **13**, 049401.
- Ahlers, G., S. Grossmann, and D. Lohse, 2009, “Heat transfer and large scale dynamics in turbulent Rayleigh-Bénard convection,” *Rev. Mod. Phys.* **81**, 503–537.
- Ahlers, G., X. He, D. Funfschilling, and E. Bodenschatz, 2012, “Heat transport by turbulent Rayleigh-Bénard convection for $Pr \sim 0.8$ and $3 \times 10^{12} \lesssim Ra \lesssim 10^{15}$: Aspect ratio $\Gamma = 0.50$,” *New J. Phys.* **14**, 103012.
- Ahlers, G., and X. Xu, 2001, “Prandtl-Number Dependence of Heat Transport in Turbulent Rayleigh-Bénard Convection,” *Phys. Rev. Lett.* **86**, 3320–3323.
- Ahlers, G., *et al.*, 2022, “Aspect Ratio Dependence of Heat Transfer in a Cylindrical Rayleigh-Bénard Cell,” *Phys. Rev. Lett.* **128**, 084501.
- Amati, G., K. Koal, F. Massaioli, K. R. Sreenivasan, and R. Verzicco, 2005, “Turbulent thermal convection at high Rayleigh-numbers for a constant-Prandtl-number fluid under Boussinesq conditions,” *Phys. Fluids* **17**, 121701.
- Andereck, C. D., S. S. Liu, and H. L. Swinney, 1986, “Flow regimes in a circular Couette system with independently rotating cylinders,” *J. Fluid Mech.* **164**, 155.
- Antonia, R. A., 1980, “Behaviour of the turbulent Prandtl number near the wall,” *Int. J. Heat Mass Transfer* **23**, 906–908.
- Antonia, R. A., and J. Kim, 1991, “Turbulent Prandtl number in the near-wall region of a turbulent channel flow,” *Int. J. Heat Mass Transfer* **34**, 1905–1908.
- Ashkenazi, S., and V. Steinberg, 1999, “High Rayleigh Number Turbulent Convection in a Gas near the Gas-Liquid Critical Point,” *Phys. Rev. Lett.* **83**, 3641–3644.
- Avila, K., D. Moxey, A. D. Lozar, M. Avila, D. Barkley, and B. Hof, 2011, “The onset of turbulence in pipe flow,” *Science* **333**6039, 192–196.
- Avila, M., D. Barkley, and B. Hof, 2023, “Transition to turbulence in pipe flow,” *Annu. Rev. Fluid Mech.* **55**, 575–602.
- Avila, M., F. Mellibovsky, N. Roland, and B. Hof, 2013, “Streamwise-Localized Solutions at the Onset of Turbulence in Pipe Flow,” *Phys. Rev. Lett.* **110**, 224502.
- Bailon-Cuba, J., M. S. Emran, and J. Schumacher, 2010, “Aspect ratio dependence of heat transfer and large-scale flow in turbulent convection,” *J. Fluid Mech.* **655**, 152–173.
- Barkley, D., 2016, “Theoretical perspective on the route to turbulence in a pipe,” *J. Fluid Mech.* **803**, P1.
- Batchelor, G. K., 1967, *An Introduction to Fluid Dynamics* (Cambridge University Press, Cambridge, England).
- Behringer, R. P., 1985, “Rayleigh-Bénard convection and turbulence in liquid-helium,” *Rev. Mod. Phys.* **57**, 657–687.
- Belkadi, M., A. Sergent, Y. Fraigneau, and B. Podvin, 2021, “On the role of roughness valleys in turbulent Rayleigh-Bénard convection,” *J. Fluid Mech.* **923**, A6.
- Blasius, H., 1908, “Grenzschichten in Flüssigkeiten mit kleiner Reibung [Boundary layers in fluids with low friction],” *Z. Angew. Math. Phys.* **56**, 1–37.
- Boberg, L., and U. Brosa, 1988, “Onset of turbulence in a pipe,” *Z. Naturforsch. A* **43**, 697–726.
- Bodenschatz, E., X. He, D. van Gils, and G. Ahlers, 2015, “Aspect-ratio dependence of the transition to the ultimate state of turbulent Rayleigh-Bénard convection,” in *Proceedings of the 15th European Turbulence Conference, Delft, Netherlands, 2015* (Delft University of Technology, Delft, Netherlands).

- Bodenschatz, E., W. Pesch, and G. Ahlers, 2000, “Recent developments in Rayleigh-Bénard convection,” *Annu. Rev. Fluid Mech.* **32**, 709–778.
- Bouillaut, V., S. Lepot, S. Aumaître, and B. Gallet, 2019, “Transition to the ultimate regime in a radiatively driven convection experiment,” *J. Fluid Mech.* **861**, R5.
- Boussinesq, J., 1903, *Théorie Analytique de la Chaleur* (Gauthier-Villars, Paris).
- Bradshaw, P., 1969, “The analogy between streamline curvature and buoyancy in turbulent shear flow,” *J. Fluid Mech.* **36**, 177–191.
- Brauckmann, H. J., and B. Eckhardt, 2013, “Direct numerical simulations of local and global torque in Taylor-Couette flow up to $Re = 30\,000$,” *J. Fluid Mech.* **718**, 398–427.
- Brauckmann, H. J., B. Eckhardt, and J. Schumacher, 2017, “Heat transport in Rayleigh-Bénard convection and angular momentum transport in Taylor-Couette flow: A comparative study,” *Phil. Trans. R. Soc. A* **375**2089, 20160079.
- Brichet, L., R. Braun, L. Méthivier, E. Bernard, F. Chillà, and J. Salort, 2024, “Universal scaling laws in turbulent Rayleigh-Bénard convection with and without roughness” (to be published).
- Brown, E., and G. Ahlers, 2006, “Rotations and cessations of the large-scale circulation in turbulent Rayleigh-Bénard convection,” *J. Fluid Mech.* **568**, 351–386.
- Brown, E., A. Nikolaenko, and G. Ahlers, 2005, “Reorientations of the Large-Scale Circulation in Turbulent Rayleigh-Bénard Convection,” *Phys. Rev. Lett.* **95**, 084503.
- Brown, E., A. Nikolaenko, D. Funfschilling, and G. Ahlers, 2005, “Heat transport in turbulent Rayleigh-Bénard convection: Effect of finite top- and bottom-plate conductivities,” *Phys. Fluids* **17**, 075108.
- Buell, J. C., and I. Catton, 1983, “The effect of wall conduction on the stability of a fluid in a right circular cylinder heated from below,” *J. Heat Transfer* **105**, 255–260.
- Burnishev, Y., E. Segre, and V. Steinberg, 2010, “Strong symmetrical non-Oberbeck-Boussinesq turbulent convection and the role of compressibility,” *Phys. Fluids* **22**, 035108.
- Busse, F. H., 1967, “The stability of finite amplitude cellular convection and its relation to an extremum principle,” *J. Fluid Mech.* **30**, 625–649.
- Busse, F. H., 1969, “On Howard’s upper bound for heat transport by turbulent convection,” *J. Fluid Mech.* **37**, 457–477.
- Busse, F. H., 2012, “Viewpoint: The twins of turbulence research,” *Physics* **5**, 4.
- Calzavarini, E., C. R. Doering, J. D. Gibbon, D. Lohse, A. Tanabe, and F. Toschi, 2006, “Exponentially growing solutions in homogeneous Rayleigh-Bénard convection,” *Phys. Rev. E* **73**, 035301(R).
- Calzavarini, E., D. Lohse, F. Toschi, and R. Tripiccione, 2005, “Rayleigh and Prandtl number scaling in the bulk of Rayleigh-Bénard turbulence,” *Phys. Fluids* **17**, 055107.
- Castaing, B., G. Gunaratne, F. Heslot, L. Kadanoff, A. Libchaber, S. Thomae, X.-Z. Wu, S. Zaleski, and G. Zanetti, 1989, “Scaling of hard thermal turbulence in Rayleigh-Bénard convection,” *J. Fluid Mech.* **204**, 1–30.
- Chan, S. K., 1971, “Infinite Prandtl number turbulent convection,” *Stud. Appl. Math.* **50**, 13–49.
- Chandrasekhar, S., 1953, “The instability of a layer of fluid heat below and subject to Coriolis forces,” *Proc. R. Soc. A* **217**, 306–327.
- Chandrasekhar, S., 1961, *Hydrodynamic and Hydromagnetic Stability* (Clarendon Press, Oxford).
- Chaumat, S., B. Castaing, and F. Chillà, 2002, “Rayleigh-Bénard cells: Influence of plate properties,” in *Advances in Turbulence IX: Proceedings of the 9th European Turbulence Conference*, edited by I. P. Castro, P. E. Hancock, and T. G. Thomas (International Center for Numerical Methods in Engineering, Barcelona).
- Chavanne, X., F. Chillà, B. Castaing, B. Hébral, B. Chabaud, and J. Chaussy, 1997, “Observation of the Ultimate Regime in Rayleigh-Bénard Convection,” *Phys. Rev. Lett.* **79**, 3648–3651.
- Chavanne, X., F. Chillà, B. Chabaud, B. Castaing, and B. Hébral, 2001, “Turbulent Rayleigh-Bénard convection in gaseous and liquid He,” *Phys. Fluids* **13**, 1300–1320.
- Chillà, F., M. Rastello, S. Chaumat, and B. Castaing, 2004a, “Long relaxation times and tilt sensitivity in Rayleigh-Bénard turbulence,” *Eur. Phys. J. B* **40**, 223–227.
- Chillà, F., M. Rastello, S. Chaumat, and B. Castaing, 2004b, “Ultimate regime in Rayleigh-Bénard convection: The role of plates,” *Phys. Fluids* **16**, 2452–2456.
- Chillà, F., and J. Schumacher, 2012, “New perspectives in turbulent Rayleigh-Bénard convection,” *Eur. Phys. J. E* **35**, 58.
- Ching, E. S. C., O.-Y. Dung, and O. Shishkina, 2017, “Fluctuating thermal boundary layers and heat transfer in turbulent Rayleigh-Bénard convection,” *J. Stat. Phys.* **167**, 626–635.
- Ching, E. S. C., H. S. Leung, L. Zwirner, and O. Shishkina, 2019, “Velocity and thermal boundary layer equations for turbulent Rayleigh-Bénard convection,” *Phys. Rev. Res.* **1**, 033037.
- Choffrut, A., C. Nobili, and F. Otto, 2016, “Upper bounds on Nusselt number at finite Prandtl number,” *J. Differ. Equations* **260**, 3860–3880.
- Cholehari, M. R., and J. H. Arakeri, 2005, “Experiments and a model of turbulent exchange flow in a vertical pipe,” *Int. J. Heat Mass Transfer* **48**, 4467–4473.
- Cholehari, M. R., and J. H. Arakeri, 2009, “Axially homogeneous, zero mean flow buoyancy-driven turbulence in a vertical pipe,” *J. Fluid Mech.* **621**, 69–102.
- Chong, K. L., S. Wagner, M. Kaczorowski, O. Shishkina, and K.-Q. Xia, 2018, “Effect of Prandtl number on heat transport enhancement in Rayleigh-Bénard convection under geometrical confinement,” *Phys. Rev. Fluids* **3**, 013501.
- Chong, K. L., and K.-Q. Xia, 2016, “Exploring the severely confined regime in Rayleigh-Bénard convection,” *J. Fluid Mech.* **805**, R4.
- Chung, D., N. Hutchins, M. P. Schultz, and K. A. Flack, 2021, “Predicting the drag of rough surfaces,” *Annu. Rev. Fluid Mech.* **53**, 439–471.
- Ciliberto, S., and C. Laroche, 1999, “Random Roughness of Boundary Increases the Turbulent Scaling Exponents,” *Phys. Rev. Lett.* **82**, 3998–4001.
- Cioni, S., S. Ciliberto, and J. Sommeria, 1997, “Strongly turbulent Rayleigh-Bénard convection in mercury: Comparison with results at moderate Prandtl number,” *J. Fluid Mech.* **335**, 111–140.
- Constantin, P., and C. R. Doering, 1999, “Infinite Prandtl number convection,” *J. Stat. Phys.* **94**, 159–172.
- Cross, M. C., and P. C. Hohenberg, 1993, “Pattern formation outside of equilibrium,” *Rev. Mod. Phys.* **65**, 851–1112.
- Daya, Z. A., and R. E. Ecke, 2001, “Does Turbulent Convection Feel the Shape of the Container?,” *Phys. Rev. Lett.* **87**, 184501.
- de Bruyn, J. R., E. Bodenschatz, S. W. Morris, S. Trainoff, Y. Hu, D. S. Cannell, and G. Ahlers, 1996, “Apparatus for the study of Rayleigh-Bénard convection in gases under pressure,” *Rev. Sci. Instrum.* **67**, 2043–2067.
- Doering, C., and P. Constantin, 1994, “Variational bounds on energy-dissipation in incompressible flow: Shear flow,” *Phys. Rev. E* **49**, 4087–4099.
- Doering, C. R., and P. Constantin, 1996, “Variational bounds on energy dissipation in incompressible flows. III. Convection,” *Phys. Rev. E* **53**, 5957.

- Doering, C. R., F. Otto, and M. G. Reznikoff, 2006, “Bounds on vertical heat transport for infinite-Prandtl number Rayleigh-Bénard convection,” *J. Fluid Mech.* **560**, 229–242.
- Doering, C. R., and I. Tobasco, 2019, “On the optimal design of wall-to-wall heat transport,” *Commun. Pure Appl. Math.* **72**, 2385–2448.
- Doering, C. R., S. Toppaladoddi, and J. S. Wettlaufer, 2019, “Absence of Evidence for the Ultimate Regime in Two-Dimensional Rayleigh-Bénard Convection,” *Phys. Rev. Lett.* **123**, 259401.
- Drazin, P., and W. H. Reid, 1981, *Hydrodynamic Stability* (Cambridge University Press, Cambridge, England).
- Du, Y. B., and P. Tong, 2000, “Turbulent thermal convection in a cell with ordered rough boundaries,” *J. Fluid Mech.* **407**, 57–84.
- Dubulle, B., and F. Hersant, 2002, “Momentum transport and torque scaling in Taylor-Couette flow from an analogy with turbulent convection,” *Eur. Phys. J. B* **26**, 379–386.
- du Puits, R., C. Resagk, and A. Thess, 2007, “Mean Velocity Profile in Confined Turbulent Convection,” *Phys. Rev. Lett.* **99**, 234504.
- du Puits, R., C. Resagk, A. Tilgner, F. H. Busse, and A. Thess, 2007, “Structure of thermal boundary layers in turbulent Rayleigh-Bénard convection,” *J. Fluid Mech.* **572**, 231–254.
- Ecke, R. E., and O. Shishkina, 2023, “Turbulent rotating Rayleigh-Bénard convection,” *Annu. Rev. Fluid Mech.* **55**, 603–638.
- Ecke, R. E., X. Zhang, and O. Shishkina, 2022, “Connecting wall modes and boundary zonal flows in rotating Rayleigh-Bénard convection,” *Phys. Rev. Fluids* **7**, L011501.
- Eckhardt, B., S. Grossmann, and D. Lohse, 2007a, “Fluxes and energy dissipation in thermal convection and shear flows,” *Europhys. Lett.* **78**, 24001.
- Eckhardt, B., S. Grossmann, and D. Lohse, 2007b, “Torque scaling in turbulent Taylor-Couette flow between independently rotating cylinders,” *J. Fluid Mech.* **581**, 221–250.
- Eckhardt, B., S. Grossmann, and D. Lohse, 2007c, “What Rayleigh-Bénard, Taylor-Couette, and pipe flows have in common,” in *Progress in Turbulence II: Proceedings of the iTi Conference in Turbulence 2005*, Springer Proceedings in Physics Vol. 109, edited by M. Oberlack, G. Khujudze, S. Günther, T. Weller, M. Frewer, J. Peinke, and S. Barth (Springer, New York), pp. 3–10.
- Eckhardt, B., T. Schneider, B. Hof, and J. Westerweel, 2007, “Turbulence transition in pipe flow,” *Annu. Rev. Fluid Mech.* **39**, 447–468.
- Emran, M. S., and J. Schumacher, 2012, “Conditional statistics of thermal dissipation rate in turbulent Rayleigh-Bénard convection,” *Eur. Phys. J. E* **35**, 108.
- Emran, M. S., and J. Schumacher, 2015, “Large-scale mean patterns in turbulent convection,” *J. Fluid Mech.* **776**, 96–108.
- Emran, M. S., and O. Shishkina, 2020, “Natural convection in cylindrical containers with isothermal ring-shaped obstacles,” *J. Fluid Mech.* **882**, A3.
- Fantuzzi, G., A. Arslan, and A. Wynn, 2022, “The background method: Theory and computations,” *Phil. Trans. R. Soc. A* **380**, 20210038.
- Fardin, M. A., C. Perge, and N. Taberlet, 2014, “The hydrogen atom of fluid dynamics—Introduction to the Taylor-Couette flow for soft matter scientists,” *Soft Matter* **10**, 3523–3535.
- Farrell, B. F., and P. J. Ioannou, 1993, “Optimal excitation of three-dimensional perturbations in viscous constant shear flow,” *Phys. Fluids* **5**, 1390–1400.
- Farrell, B. H., 1988, “Optimal excitation of perturbations in viscous shear flow,” *Phys. Fluids* **31**, 2093–2102.
- Fefferman, C. L., 2006, in *The Millennium Prize Problems*, edited by J. Carlson, A. Jaffe, and A. Wiles (American Mathematical Society, Providence), pp. 57–67.
- Fleischer, A. S., and R. J. Goldstein, 2002, “High-Rayleigh number convection of pressurized gases in a horizontal enclosure,” *J. Fluid Mech.* **469**, 1–12.
- Foroozani, N., J. J. Niemela, V. Armenio, and K. R. Sreenivasan, 2019, “Turbulent convection and large scale circulation in a cube with rough horizontal surfaces,” *Phys. Rev. E* **99**, 033116.
- Funfschilling, D., E. Bodenschatz, and G. Ahlers, 2009, “Search for the ‘Ultimate State’ in Turbulent Rayleigh-Bénard Convection,” *Phys. Rev. Lett.* **103**, 014503.
- Funfschilling, D., E. Brown, A. Nikolaenko, and G. Ahlers, 2005, “Heat transport by turbulent Rayleigh-Bénard convection in cylindrical samples with aspect ratio one and larger,” *J. Fluid Mech.* **536**, 145–154.
- Gauthier, F., and P.-E. Roche, 2008, “Evidence of a boundary layer instability at very high Rayleigh number,” *Europhys. Lett.* **83**, 24005.
- Gauthier, F., J. Salort, O. Bourgeois, J.-L. Garden, R. du Puits, A. Thess, and P.-E. Roche, 2009, “Transition on local temperature fluctuations in highly turbulent convection,” *Europhys. Lett.* **87**, 44006.
- Gebhardt, T., and G. Grossmann, 1994, “Chaos transition despite linear stability,” *Phys. Rev. E* **50**, 3705–3714.
- Gibert, M., H. Pabiou, F. Chillà, and B. Castaing, 2006, “High-Rayleigh-Number Convection in a Vertical Channel,” *Phys. Rev. Lett.* **96**, 084501.
- Gibert, M., H. Pabiou, J.-C. Tisserand, B. Gertjerenken, B. Castaing, and F. Chillà, 2009, “Heat convection in a vertical channel: Plumes versus turbulent diffusion,” *Phys. Fluids* **21**, 035109.
- Glazier, J. A., T. Segawa, A. Naert, and M. Sano, 1999, “Evidence against ‘ultrahard’ thermal turbulence at very high Rayleigh numbers,” *Nature (London)* **398**, 307–310.
- Goluskin, D., 2016, *Internally Heated Convection and Rayleigh-Bénard Convection* (Springer, New York).
- Goluskin, D., and C. R. Doering, 2016, “Bounds for convection between rough boundaries,” *J. Fluid Mech.* **804**, 370–386.
- Gray, D. D., and A. Giorgini, 1976, “The validity of the Boussinesq approximation for liquids and gases,” *Int. J. Heat Mass Transfer* **19**, 545–551.
- Grossmann, S., 2000, “The onset of shear flow turbulence,” *Rev. Mod. Phys.* **72**, 603–618.
- Grossmann, S., and D. Lohse, 1993, “Characteristic scales in Rayleigh-Bénard convection,” *Phys. Lett. A* **173**, 58.
- Grossmann, S., and D. Lohse, 2000, “Scaling in thermal convection: A unifying theory,” *J. Fluid Mech.* **407**, 27–56.
- Grossmann, S., and D. Lohse, 2001, “Thermal Convection for Large Prandtl Numbers,” *Phys. Rev. Lett.* **86**, 3316–3319.
- Grossmann, S., and D. Lohse, 2002, “Prandtl and Rayleigh number dependence of the Reynolds number in turbulent thermal convection,” *Phys. Rev. E* **66**, 016305.
- Grossmann, S., and D. Lohse, 2004, “Fluctuations in turbulent Rayleigh-Bénard convection: The role of plumes,” *Phys. Fluids* **16**, 4462–4472.
- Grossmann, S., and D. Lohse, 2011, “Multiple scaling in the ultimate regime of thermal convection,” *Phys. Fluids* **23**, 045108.
- Grossmann, S., and D. Lohse, 2012, “Logarithmic temperature profiles in the ultimate regime of thermal convection,” *Phys. Fluids* **24**, 125103.
- Grossmann, S., D. Lohse, and C. Sun, 2016, “High-Reynolds number Taylor-Couette turbulence,” *Annu. Rev. Fluid Mech.* **48**, 53–80.

- Grötzbach, G., 1983, “Spatial resolution requirements for direct numerical simulation of the Rayleigh-Bénard convection,” *J. Comput. Phys.* **49**, 241–264.
- Hartmann, R., K. Chong, R. Stevens, R. Verzicco, and D. Lohse, 2021, “Heat transport enhancement in confined Rayleigh-Bénard convection feels the shape of the container,” *Europhys. Lett.* **135**, 24004.
- Hassanzadeh, P., G. P. Chini, and C. R. Doering, 2014, “Wall to wall optimal transport,” *J. Fluid Mech.* **751**, 627–662.
- He, X., E. Bodenschatz, and G. Ahlers, 2016, “Azimuthal diffusion of the large-scale-circulation plane, and absence of significant non-Boussinesq effects, in turbulent convection near the ultimate-state transition,” *J. Fluid Mech.* **791**, R3.
- He, X., E. Bodenschatz, and G. Ahlers, 2020, “Aspect ratio dependence of the ultimate-state transition in turbulent thermal convection,” *Proc. Natl. Acad. Sci. U.S.A.* **117**, 30022.
- He, X., E. Bodenschatz, and G. Ahlers, 2022, “Universal scaling of temperature variance in Rayleigh-Bénard convection near the transition to the ultimate state,” *J. Fluid Mech.* **931**, A7.
- He, X., D. Funfschilling, E. Bodenschatz, and G. Ahlers, 2012, “Heat transport by turbulent Rayleigh-Bénard convection for $Pr \sim 0.8$ and $4 \times 10^{11} \lesssim Ra \lesssim 2 \times 10^{14}$: Ultimate-state transition for aspect ratio $\Gamma = 1.00$,” *New J. Phys.* **14**, 063030.
- He, X., D. Funfschilling, H. Nobach, E. Bodenschatz, and G. Ahlers, 2012, “Transition to the Ultimate State of Turbulent Rayleigh-Bénard Convection,” *Phys. Rev. Lett.* **108**, 024502.
- He, X., D. Funfschilling, H. Nobach, E. Bodenschatz, and G. Ahlers, 2013, “Comment on ‘Effect of Boundary Layers Asymmetry on Heat Transfer Efficiency in Turbulent Rayleigh-Bénard Convection at Very High Rayleigh Numbers,’ ” *Phys. Rev. Lett.* **110**, 199401.
- He, X., D. van Gils, E. Bodenschatz, and G. Ahlers, 2014, “Logarithmic Spatial Variations and Universal f^{-1} Power Spectra of Temperature Fluctuations in Turbulent Rayleigh-Bénard Convection,” *Phys. Rev. Lett.* **112**, 174501.
- He, X., D. van Gils, E. Bodenschatz, and G. Ahlers, 2015, “Reynolds numbers and the elliptic approximation near the ultimate state of turbulent Rayleigh-Bénard convection,” *New J. Phys.* **17**, 063028.
- Hebert, F., R. Hufschmid, J. Scheel, and G. Ahlers, 2010, “Onset of Rayleigh-Bénard convection in cylindrical containers,” *Phys. Rev. E* **81**, 046318.
- Herring, J. R., 1963, “Investigation of problems in thermal convection,” *J. Atmos. Sci.* **20**, 325–338.
- Herring, J. R., 1964, “Investigation of problems in thermal convection: Rigid boundaries,” *J. Atmos. Sci.* **21**, 277–290.
- Heslot, F., B. Castaing, and A. Libchaber, 1987, “Transitions to turbulence in helium gas,” *Phys. Rev. A* **36**, 5870–5873.
- Hof, B., J. Westerweel, T. M. Schneider, and B. Eckhardt, 2006, “Finite lifetime of turbulence in shear flow,” *Nature (London)* **443**, 59–62.
- Horn, S., and J. M. Aurnou, 2018, “Regimes of Coriolis-Centrifugal Convection,” *Phys. Rev. Lett.* **120**, 204502.
- Horn, S., and J. M. Aurnou, 2019, “Rotating convection with centrifugal buoyancy: Numerical predictions for laboratory experiments,” *Phys. Rev. Fluids* **4**, 073501.
- Horn, S., and O. Shishkina, 2014, “Rotating non-Oberbeck-Boussinesq Rayleigh-Bénard convection in water,” *Phys. Fluids* **26**, 055111.
- Horn, S., O. Shishkina, and C. Wagner, 2013, “On non-Oberbeck-Boussinesq effects in three-dimensional Rayleigh-Bénard convection in glycerol,” *J. Fluid Mech.* **724**, 175–202.
- Howard, L. N., 1963, “Heat transport by turbulent convection,” *J. Fluid Mech.* **17**, 405–432.
- Howard, L. N., 1972, “Bounds on flow quantities,” *Annu. Rev. Fluid Mech.* **4**, 473–494.
- Hu, Y., R. Ecke, and G. Ahlers, 1993, “Convection near threshold for Prandtl numbers near 1,” *Phys. Rev. E* **48**, 4399–4413.
- Hughes, G. O., and R. W. Griffiths, 2008, “Horizontal convection,” *Annu. Rev. Fluid Mech.* **40**, 185–208.
- Huisman, S. G., S. Scharnowski, C. Cierpka, C. Kähler, D. Lohse, and C. Sun, 2013, “Logarithmic Boundary Layers in Strong Taylor-Couette Turbulence,” *Phys. Rev. Lett.* **110**, 264501.
- Huisman, S. G., R. C. A. van der Veen, C. Sun, and D. Lohse, 2014, “Multiple states in highly turbulent Taylor-Couette flow,” *Nat. Commun.* **5**, 3820.
- Huisman, S. G., D. P. M. van Gils, S. Grossmann, C. Sun, and D. Lohse, 2012, “Ultimate Turbulent Taylor-Couette Flow,” *Phys. Rev. Lett.* **108**, 024501.
- Iyer, K. P., J. D. Scheel, J. Schumacher, and K. R. Sreenivasan, 2020, “Classical 1/3 scaling of convection holds up to $Ra = 10^{15}$,” *Proc. Natl. Acad. Sci. U.S.A.* **117**, 7594–7598.
- Jeffreys, H., 1928, “Some cases of instability in fluid motion,” *Proc. R. Soc. A* **118**, 195–208.
- Jiang, H., D. Wang, S. Liu, and C. Sun, 2022, “Experimental Evidence for the Existence of the Ultimate Regime in Rapidly Rotating Turbulent Thermal Convection,” *Phys. Rev. Lett.* **129**, 204502.
- Jiang, H., X. Zhu, V. Mathai, R. Verzicco, D. Lohse, and C. Sun, 2018, “Controlling Heat Transport and Flow Structures in Thermal Turbulence Using Ratchet Surfaces,” *Phys. Rev. Lett.* **120**, 044501.
- Jiang, H., X. Zhu, D. Wang, S. G. Huisman, and C. Sun, 2020, “Supergravitational turbulent thermal convection,” *Sci. Adv.* **6**, eabb8676.
- Joshi, P., H. Rajaei, R. P. J. Kunnen, and H. J. H. Clercx, 2017, “Heat transfer in rotating Rayleigh-Bénard convection with rough plates,” *J. Fluid Mech.* **830**, R3.
- Kadanoff, L. P., 2001, “Turbulent heat flow: Structures and scaling,” *Phys. Today* **54**, No. 8, 34–39.
- Kaiser, R., J. Salort, and P.-E. Roche, 2011, “The ultimate regime of convection over uneven plates,” *J. Phys. Conf. Ser.* **318**, 052044.
- Kawano, K., S. Motoki, M. Shimizu, and G. Kawahara, 2021, “Ultimate heat transfer in wall-bounded convective turbulence,” *J. Fluid Mech.* **914**, A13.
- Kerr, R. M., 1996, “Rayleigh number scaling in numerical convection,” *J. Fluid Mech.* **310**, 139–179.
- Kerswell, R. R., 2002, “Elliptical instability,” *Annu. Rev. Fluid Mech.* **34**, 83–113.
- Kolmogorov, A. N., 1941, “The local structure of turbulence in incompressible viscous fluid for very large Reynolds numbers,” *Dokl. Akad. Nauk SSSR* **30**, 299–303.
- Kooij, G. L., M. A. Botchev, E. M. Frederix, B. J. Geurts, S. Horn, D. Lohse, E. P. van der Poel, O. Shishkina, R. J. A. M. Stevens, and R. Verzicco, 2018, “Comparison of computational codes for direct numerical simulations of turbulent Rayleigh-Bénard convection,” *Comput. Fluids* **166**, 1–8.
- Kraichnan, R., 1962, “Turbulent thermal convection at arbitrary Prandtl number,” *Phys. Fluids* **5**, 1374–1389.
- Kraichnan, R., 1967, “Inertial ranges in two-dimensional turbulence,” *Phys. Fluids* **10**, 1417.
- Krug, D., X. Zhu, D. Chung, I. Marusic, R. Verzicco, and D. Lohse, 2018, “Transition to ultimate Rayleigh-Bénard turbulence revealed through extended self-similarity scaling analysis of the temperature structure functions,” *J. Fluid Mech.* **851**, R3.
- Lakkaraju, R., R. J. A. M. Stevens, R. Verzicco, S. Grossmann, A. Prosperetti, C. Sun, and D. Lohse, 2012, “Spatial distribution of heat flux and fluctuations in turbulent Rayleigh-Bénard convection,” *Phys. Rev. E* **86**, 056315.
- Landau, L. D., 1944, “On the problem of turbulence,” *Dokl. Akad. Nauk SSSR* **44**, 311–314.

- Landau, L. D., and E. M. Lifshitz, 1987, *Fluid Mechanics*, 2nd ed., Course of Theoretical Physics Vol. 6 (Butterworth-Heinemann, Oxford).
- Lepot, S., S. Aumaître, and B. Gallet, 2018, “Radiative heating achieves the ultimate regime of thermal convection,” *Proc. Natl. Acad. Sci. U.S.A.* **115**, 8937–8941.
- Lévêque, A., 1928, *Les Lois de la Transmission de Chaleur par Convection*, Annales des Mines (Dunod, Paris).
- Lewis, G. S., and H. L. Swinney, 1999, “Velocity structure functions, scaling, and transitions in high-Reynolds number Couette-Taylor flow,” *Phys. Rev. E* **59**, 5457–5467.
- Lindborg, E., 2023, “Scaling in Rayleigh-Bénard convection,” *J. Fluid Mech.* **956**, A34.
- Liot, O., Q. Ehlinger, E. Rusaouen, T. Coudarchet, J. Salort, and F. Chillà, 2017, “Velocity fluctuations and boundary layer structure in a rough Rayleigh-Bénard cell filled with water,” *Phys. Rev. Fluids* **2**, 044605.
- Liot, O., J. Salort, R. Kaiser, R. du Puits, and F. Chillà, 2016, “Boundary layer structure in a rough Rayleigh-Bénard cell filled with air,” *J. Fluid Mech.* **786**, 275–293.
- Lohse, D., and O. Shishkina, 2023, “Ultimate turbulent thermal convection,” *Phys. Today*, No. 11, **76**, 26–32.
- Lohse, D., and F. Toschi, 2003, “Ultimate State of Thermal Convection,” *Phys. Rev. Lett.* **90**, 034502.
- Lohse, D., and K.-Q. Xia, 2010, “Small-scale properties of turbulent Rayleigh-Bénard convection,” *Annu. Rev. Fluid Mech.* **42**, 335–364.
- Lorenz, E. N., 1963, “Deterministic nonperiodic flow,” *J. Atmos. Sci.* **20**, 130–141.
- Macek, M., G. Zinchenko, V. Musilova, P. Urban, and J. Schumacher, 2023, “Assessing non-Oberbeck-Boussinesq effects of convection in cryogenic helium,” *Phys. Rev. Fluids* **8**, 094606.
- Malkus, M. V. R., 1954, “The heat transport and spectrum of thermal turbulence,” *Proc. R. Soc. A* **225**, 196–212.
- Manga, M., and D. Weeraratne, 1999, “Experimental study of non-Boussinesq Rayleigh-Bénard convection at high Rayleigh and Prandtl numbers,” *Phys. Fluids* **11**, 2969–2976.
- Manneville, P., 2016, “Transition to turbulence in wall-bounded flows: Where do we stand?,” *Mech. Eng. Rev.* **3**, 15.
- Marusic, I., and J. P. Monty, 2019, “Attached eddy model of wall turbulence,” *Annu. Rev. Fluid Mech.* **51**, 49–74.
- McCormack, M., A. Teimurazov, O. Shishkina, and M. Linkmann, 2023, “Wall mode dynamics and transition to chaos in magnetoconvection with a vertical magnetic field,” *J. Fluid Mech.* **975**, R2.
- Méthivier, L., R. Braun, F. Chillà, and J. Salort, 2022, “Turbulent transition in Rayleigh-Bénard convection with fluorocarbon,” *Europhys. Lett.* **136**, 10003.
- Mihaljan, J. M., 1962, “A rigorous exposition of the Boussinesq approximations applicable to a thin layer of fluid,” *Astrophys. J.* **136**, 1126–1133.
- Miquel, B., V. Bouillaud, S. Aumaître, and B. Gallet, 2020, “On the role of the Prandtl number in convection driven by heat sources and sinks,” *J. Fluid Mech.* **900**, R1.
- Monin, A. S., and A. M. Yaglom, 1975, *Statistical Fluid Mechanics* (MIT Press, Cambridge, MA).
- Motoki, S., G. Kawahara, and M. Shimizu, 2018, “Maximal heat transfer between two parallel plates,” *J. Fluid Mech.* **851**, R4.
- Musilová, V., T. Králík, M. L. Mantia, M. Macek, P. Urban, and L. Skrbek, 2017, “Reynolds number scaling in cryogenic turbulent Rayleigh-Bénard convection in a cylindrical aspect ratio one cell,” *J. Fluid Mech.* **832**, 721–744.
- National Institute of Standards and Technology, 2013, computer code REFPROP, version 9.1.
- Niemela, J., L. Skrbek, K. R. Sreenivasan, and R. J. Donnelly, 2001, “The wind in confined thermal turbulence,” *J. Fluid Mech.* **449**, 169–178.
- Niemela, J. J., S. Babuin, and K. R. Sreenivasan, 2010, “Turbulent rotating convection at high Rayleigh and Taylor numbers,” *J. Fluid Mech.* **649**, 509–522.
- Niemela, J. J., L. Skrbek, and R. J. Donnelly, 2000, “Ultrahigh Rayleigh number convection in cryogenic helium gas,” *Physica (Amsterdam)* **284B–288B**, 61–62.
- Niemela, J. J., L. Skrbek, K. R. Sreenivasan, and R. J. Donnelly, 2000, “Turbulent convection at very high Rayleigh numbers,” *Nature (London)* **404**, 837–841.
- Niemela, J. J., L. Skrbek, C. Swanson, S. Hall, K. R. Sreenivasan, and R. J. Donnelly, 2000, “New results in cryogenic helium flows at ultra-high Reynolds and Rayleigh numbers,” *J. Low Temp. Phys.* **121**, 417–422.
- Niemela, J. J., and K. R. Sreenivasan, 2003a, “Confined turbulent convection,” *J. Fluid Mech.* **481**, 355–384.
- Niemela, J. J., and K. R. Sreenivasan, 2003b, “Rayleigh-number evolution of large-scale coherent motion in turbulent convection,” *Europhys. Lett.* **62**, 829–833.
- Niemela, J. J., and K. R. Sreenivasan, 2006a, “Turbulent convection at high Rayleigh numbers and aspect ratio 4,” *J. Fluid Mech.* **557**, 411–422.
- Niemela, J. J., and K. R. Sreenivasan, 2006b, “The use of cryogenic helium for classical turbulence: Promises and hurdles,” *J. Low Temp. Phys.* **143**, 163–212.
- Niemela, J. J., and K. R. Sreenivasan, 2008, “Formation of the Superconducting Core in Turbulent Thermal Convection,” *Phys. Rev. Lett.* **100**, 184502.
- Niemela, J. J., and K. R. Sreenivasan, 2010, “Does confined turbulent convection ever attain the asymptotic scaling with $1/2$ power,” *New J. Phys.* **12**, 115002.
- Nikolaenko, A., E. Brown, D. Funfschilling, and G. Ahlers, 2005, “Heat transport by turbulent Rayleigh-Bénard convection in cylindrical cells with aspect ratio one and less,” *J. Fluid Mech.* **523**, 251–260.
- Nikuradse, J., 1933, *Strömungsgesetze in rauhen Rohren*, Forschungsheft Vol. 361 (Verein Deutscher Ingenieure, Düsseldorf).
- Oberbeck, A., 1879, “Über die Wärmeleitung der Flüssigkeiten bei Berücksichtigung der Strömungen in Folge von Temperaturdifferenzen [On the heat conduction of liquids, taking into account the flow due to temperature differences],” *Ann. Phys. (Berlin)* **243**, 271–292.
- Obukhov, A., 1959, “Effect of Archimedean forces on the structure of the temperature field in a turbulent flow,” *Dokl. Akad. Nauk SSSR* **125**, 1246.
- Orr, W. M., 1907, “The stability or instability of steady motions of a liquid. Part II: A viscous liquid,” *Proc. R. Irish Acad. A* **27**, 69–138.
- Ostilla-Mónico, R., E. P. van der Poel, R. Verzicco, S. Grossmann, and D. Lohse, 2014a, “Boundary layer dynamics at the transition between the classical and the ultimate regime of Taylor-Couette flow,” *Phys. Fluids* **26**, 015114.
- Ostilla-Mónico, R., E. P. van der Poel, R. Verzicco, S. Grossmann, and D. Lohse, 2014b, “Exploring the phase diagram of fully turbulent Taylor-Couette flow,” *J. Fluid Mech.* **761**, 1–26.
- Otto, F., and C. Seis, 2011, “Rayleigh-Bénard convection: Improved bounds on the Nusselt number,” *J. Math. Phys. (N.Y.)* **52**, 083702.
- Pandey, A., J. D. Scheel, and J. Schumacher, 2018, “Turbulent superstructures in Rayleigh-Bénard convection,” *Nat. Commun.* **9**, 2118.
- Pawar, S. S., and J. H. Arakeri, 2016, “Kinetic energy and scalar spectra in high Rayleigh number axially homogeneous buoyancy driven turbulence,” *Phys. Fluids* **28**, 065103.

- Pellew, A., and R. V. Southwell, 1940, “On maintained convective motion in a fluid heated from below,” *Proc. R. Soc. A* **176**, 312–343.
- Perrier, F., P. Morat, and J. L. LeMouel, 2002, “Dynamics of Air Avalanches in the Access Pit of an Underground Quarry,” *Phys. Rev. Lett.* **89**, 134501.
- Plasting, S. C., and R. R. Kerswell, 2003, “Improved upper bound on the energy dissipation rate in plane Couette flow: The full solution to Busse’s problem and the Constantin-Doering-Hopf problem with one-dimensional background field,” *J. Fluid Mech.* **477**, 363–379.
- Pohlhausen, E., 1921, “Der Wärmeaustausch zwischen festen Körpern und Flüssigkeiten mit kleiner Reibung und kleiner Wärmeleitung [Heat exchange between solid bodies and fluids with low friction and low heat conduction],” *Z. Angew. Math. Mech.* **1**, 115–121.
- Pope, S. B., 2000, *Turbulent Flows*, 1st ed. (Cambridge University Press, Cambridge, England).
- Prandtl, L., 1905, “About fluid movement with very low friction,” in *Verhandlungen des III Internationalen Mathematiker Kongresses, Heidelberg, 1904* (Teubner, Leipzig), pp. 484–491.
- Prandtl, L., 1925, “Bericht über Untersuchungen zur ausgebildeten Turbulenz [Report on investigations into developed turbulence],” *Z. Angew. Math. Mech.* **5**, 136–139.
- Priestley, C. H. B., 1954, “Convection from a large horizontal surface,” *Aust. J. Phys.* **7**, 176–201.
- Procaccia, I., E. S. C. Ching, P. Constantin, L. P. Kadanoff, A. Libchaber, and X. Z. Wu, 1991, “Transition to convective turbulence: The role of thermal plumes,” *Phys. Rev. A* **44**, 8091–8102.
- Puigjaner, D., J. Herrero, C. Simo, and F. Giralt, 2004, “Stability analysis of the flow in a cubical cavity heated from below,” *Phys. Fluids* **16**, 3639–3655.
- Puigjaner, D., J. Herrero, C. Simo, and F. Giralt, 2008, “Bifurcation analysis of steady Rayleigh-Bénard convection in a cubical cavity with conducting sidewalls,” *J. Fluid Mech.* **598**, 393–427.
- Qiu, X.-L., K.-Q. Xia, and P. Tong, 2005, “Experimental study of velocity boundary layer near a rough conducting surface in turbulent natural convection,” *J. Turbulence* **30**, 1–13.
- Rayleigh, Lord, 1916, “LIX. On convection currents in a horizontal layer of fluid, when the higher temperature is on the under side,” *Philos. Mag.* **32**, 529–546.
- Reddy, S. C., and D. S. Henningson, 1993, “Energy growth in viscous channel flows,” *J. Fluid Mech.* **252**, 209–238.
- Reddy, S. C., P. J. Schmid, and D. S. Henningson, 1993, “Pseudo-spectra of the Orr-Sommerfeld operator,” *SIAM J. Appl. Math.* **53**, 15–47.
- Reiter, P., and O. Shishkina, 2020, “Classical and symmetrical horizontal convection: Detaching plumes and oscillations,” *J. Fluid Mech.* **892**, R1.
- Reiter, P., O. Shishkina, D. Lohse, and D. Krug, 2021, “Crossover of the relative heat transport contributions of plume ejecting and impacting zones in turbulent Rayleigh-Bénard convection,” *Europhys. Lett.* **134**, 34002.
- Reiter, P., X. Zhang, and O. Shishkina, 2022, “Flow states and heat transport in Rayleigh-Bénard convection with different sidewall boundary conditions,” *J. Fluid Mech.* **936**, A32.
- Reiter, P., X. Zhang, R. Stepanov, and O. Shishkina, 2021, “Generation of zonal flows in convective systems by travelling thermal waves,” *J. Fluid Mech.* **913**, A13.
- Ren, L., X. Tao, K.-Q. Xia, and Y.-C. Xie, 2024, “Transition to fully developed turbulence in liquid metal convection facilitated by spatial confinement,” *J. Fluid Mech.* **981**, R2.
- Reynolds, O., 1883, “An experimental investigation of the circumstances which determine whether the motion of water shall be direct or sinuous, and of the law of resistance in parallel channels,” *Proc. R. Soc. London* **35**, 84–99.
- Roberts, P. H., 1966, in *Non-Equilibrium Thermodynamics, Variational Techniques and Stability*, edited by R. J. Donnelly, R. Herman, and Ilya Prigogine (University of Chicago Press, Chicago), pp. 125–162.
- Roche, P.-E., 2020, “The ultimate state of convection: A unifying picture of very high Rayleigh numbers experiments,” *New J. Phys.* **22**, 073056.
- Roche, P.-E., B. Castaing, B. Chabaud, and B. Hébral, 2001, “Observation of the 1/2 power law in Rayleigh-Bénard convection,” *Phys. Rev. E* **63**, 045303.
- Roche, P.-E., B. Castaing, B. Chabaud, and B. Hébral, 2002, “Prandtl and Rayleigh numbers dependences in Rayleigh-Bénard convection,” *Europhys. Lett.* **58**, 693–698.
- Roche, P.-E., B. Castaing, B. Chabaud, B. Hébral, and J. Sommeria, 2001, “Side wall effects in Rayleigh-Bénard experiments,” *Eur. Phys. J. B* **24**, 405–408.
- Roche, P.-E., F. Gauthier, B. Chabaud, and B. Hébral, 2005, “Ultimate regime of convection: Robustness to poor thermal reservoirs,” *Phys. Fluids* **17**, 5107.
- Roche, P.-E., F. Gauthier, R. Kaiser, and J. Salort, 2010, “On the triggering of the ultimate regime of convection,” *New J. Phys.* **12**, 085014.
- Rouhi, A., D. Lohse, I. Marusic, C. Sun, and D. Chung, 2021, “Coriolis effect on centrifugal buoyancy-driven convection in a thin cylindrical shell,” *J. Fluid Mech.* **910**, A32.
- Rusaouën, E., O. Liot, B. Castaing, J. Salort, and F. Chillà, 2018, “Thermal transfer in Rayleigh-Bénard cell with smooth or rough boundaries,” *J. Fluid Mech.* **837**, 443–460.
- Salort, J., O. Liot, E. Rusaouën, F. Seychelles, J.-C. Tisserand, M. Creysse, B. Castaing, and F. Chillà, 2014, “Thermal boundary layer near roughnesses in turbulent Rayleigh-Bénard convection: Flow structure and multistability,” *Phys. Fluids* **26**, 015112.
- Sano, M., Z. Wu, and A. Libchaber, 1989, “Turbulence in helium-gas free convection,” *Phys. Rev. A* **40**, 6421.
- Scheel, J. D., M. S. Emran, and J. Schumacher, 2013, “Resolving the fine-scale structure in turbulent Rayleigh-Bénard convection,” *New J. Phys.* **15**, 113063.
- Scheel, J. D., E. Kim, and K. R. White, 2012, “Thermal and viscous boundary layers in turbulent Rayleigh-Bénard convection,” *J. Fluid Mech.* **711**, 281–305.
- Scheel, J. D., and J. Schumacher, 2014, “Local boundary layer scales in turbulent Rayleigh-Bénard convection,” *J. Fluid Mech.* **758**, 344–373.
- Scheel, J. D., and J. Schumacher, 2016, “Global and local statistics in turbulent convection at low Prandtl numbers,” *J. Fluid Mech.* **802**, 147–173.
- Scheel, J. D., and J. Schumacher, 2017, “Predicting transition ranges to fully turbulent viscous boundary layers in low Prandtl number convection flows,” *Phys. Rev. Fluids* **2**, 123501.
- Schlichting, H., 1979, *Boundary Layer Theory* (McGraw-Hill, New York).
- Schlueter, A., D. Lortz, and F. Busse, 1965, “On the stability of steady finite amplitude convection,” *J. Fluid Mech.* **23**, 129–144.
- Schmid, P. J., 2007, “Nonmodal stability theory,” *Annu. Rev. Fluid Mech.* **39**, 129–162.
- Schmid, P. J., and D. S. Henningson, 2001, *Stability and Transition in Shear Flows* (Springer-Verlag, New York).
- Schmidt, L. E., E. Calzavarini, D. Lohse, F. Toschi, and R. Verzicco, 2012, “Axially homogeneous Rayleigh-Bénard convection in a cylindrical cell,” *J. Fluid Mech.* **691**, 52–68.

- Schumacher, J., V. Bandaru, A. Pandey, and J. D. Scheel, 2016, “Transitional boundary layers in low-Prandtl-number convection,” *Phys. Rev. Fluids* **1**, 084402.
- Seis, C., 2015, “Scaling bounds on dissipation in turbulent flows,” *J. Fluid Mech.* **777**, 591–603.
- Shang, X. D., P. Tong, and K.-Q. Xia, 2008, “Scaling of the Local Convective Heat Flux in Turbulent Rayleigh-Bénard Convection,” *Phys. Rev. Lett.* **100**, 244503.
- Shang, X.-D., X.-L. Qiu, P. Tong, and K.-Q. Xia, 2003, “Measured Local Heat Transport in Turbulent Rayleigh-Bénard Convection,” *Phys. Rev. Lett.* **90**, 074501.
- Shen, Y., K.-Q. Xia, and P. Tong, 1996, “Turbulent Convection over Rough Surfaces,” *Phys. Rev. Lett.* **76**, 908–911.
- Shi, N., M. S. Emran, and J. Schumacher, 2012, “Boundary layer structure in turbulent Rayleigh-Bénard convection,” *J. Fluid Mech.* **706**, 5–33.
- Shishkina, O., 2017, “Mean flow structure in horizontal convection,” *J. Fluid Mech.* **812**, 525–540.
- Shishkina, O., 2021, “Rayleigh-Bénard convection: The container shape matters,” *Phys. Rev. Fluids* **6**, 090502.
- Shishkina, O., M. S. Emran, S. Grossmann, and D. Lohse, 2017, “Scaling relations in large-Prandtl-number natural thermal convection,” *Phys. Rev. Fluids* **2**, 103502.
- Shishkina, O., S. Grossmann, and D. Lohse, 2016, “Heat and momentum transport scalings in horizontal convection,” *Geophys. Res. Lett.* **43**, 1219–1225.
- Shishkina, O., S. Horn, M. S. Emran, and E. S. C. Ching, 2017, “Mean temperature profiles in turbulent thermal convection,” *Phys. Rev. Fluids* **2**, 113502.
- Shishkina, O., S. Horn, and S. Wagner, 2013, “Falkner-Skan boundary layer approximation in Rayleigh-Bénard convection,” *J. Fluid Mech.* **730**, 442–463.
- Shishkina, O., S. Horn, S. Wagner, and E. S. C. Ching, 2015, “Thermal Boundary Layer Equation for Turbulent Rayleigh-Bénard Convection,” *Phys. Rev. Lett.* **114**, 114302.
- Shishkina, O., and D. Lohse, 2024, “Ultimate regime of Rayleigh-Bénard turbulence: Sub-regimes and their scaling relations for Nu vs. Ra and Pr ,” [arXiv.org/abs/2407.16573](https://arxiv.org/abs/2407.16573).
- Shishkina, O., R. J. A. M. Stevens, S. Grossmann, and D. Lohse, 2010, “Boundary layer structure in turbulent thermal convection and its consequences for the required numerical resolution,” *New J. Phys.* **12**, 075022.
- Shishkina, O., and A. Thess, 2009, “Mean temperature profiles in turbulent Rayleigh-Bénard convection of water,” *J. Fluid Mech.* **633**, 449–460.
- Shishkina, O., and C. Wagner, 2006, “Analysis of thermal dissipation rates in turbulent Rayleigh-Bénard convection,” *J. Fluid Mech.* **546**, 51–60.
- Shishkina, O., and C. Wagner, 2007, “Boundary and interior layers in turbulent thermal convection in cylindrical containers,” *Int. J. Comput. Sci. Math.* **1**, 360–373.
- Shishkina, O., and C. Wagner, 2011, “Modelling the influence of wall roughness on heat transfer in thermal convection,” *J. Fluid Mech.* **686**, 568–582.
- Shishkina, O., and S. Wagner, 2016, “Prandtl-Number Dependence of Heat Transport in Laminar Horizontal Convection,” *Phys. Rev. Lett.* **116**, 024302.
- Shishkina, O., S. Wagner, and S. Horn, 2014, “Influence of the angle between the wind and the isothermal surfaces on the boundary layer structures in turbulent thermal convection,” *Phys. Rev. E* **89**, 033014.
- Shishkina, O., S. Weiss, and E. Bodenschatz, 2016, “Conductive heat flux in measurements of the Nusselt number in turbulent Rayleigh-Bénard convection,” *Phys. Rev. Fluids* **1**, 062301(R).
- Shraiman, B. I., and E. D. Siggia, 1990, “Heat transport in high-Rayleigh-number convection,” *Phys. Rev. A* **42**, 3650–3653.
- Siggers, J. H., R. R. Kerswell, and N. J. Balmforth, 2004, “Bounds on horizontal convection,” *J. Fluid Mech.* **517**, 55–70.
- Siggia, E., 1994, “High Rayleigh number convection,” *Annu. Rev. Fluid Mech.* **26**, 137–168.
- Skrbek, L., and P. Urban, 2015, “Has the ultimate state of turbulent thermal convection been observed?,” *J. Fluid Mech.* **785**, 270–282.
- Sommerfeld, A., 1909, in *Atti del IV Congresso Internazionale dei Matematici*, Rome, 1908, Vol. **IV**, edited by G. Castelnuovo (Tipografia della R. Accademia dei Lincei, Rome), pp. 116–124.
- Sorokin, V. S., 1954, “On stationary motions in a fluid heated from below,” *Prikl. Mat. Mekh.* **18**, 197–204.
- Souza, A. N., I. Tobasco, and C. R. Doering, 2020, “Wall-to-wall optimal transport in two dimensions,” *J. Fluid Mech.* **889**, A34.
- Spiegel, E. A., 1971, “Convection in stars I. Basic Boussinesq convection,” *Annu. Rev. Astron. Astrophys.* **9**, 323–352.
- Spiegel, E. A., and G. Veronis, 1960, “On the Boussinesq approximation for a compressible fluid,” *Astrophys. J.* **131**, 442–447.
- Stevens, R. J. A. M., A. Blass, X. Zhu, R. Verzicco, and D. Lohse, 2018, “Turbulent thermal superstructures in Rayleigh-Bénard convection,” *Phys. Rev. Fluids* **3**, 041501(R).
- Stevens, R. J. A. M., H. J. H. Clercx, and D. Lohse, 2010a, “Boundary layers in rotating weakly turbulent Rayleigh-Bénard convection,” *Phys. Fluids* **22**, 085103.
- Stevens, R. J. A. M., H. J. H. Clercx, and D. Lohse, 2010b, “Optimal Prandtl number for heat transfer in rotating Rayleigh-Bénard convection,” *New J. Phys.* **12**, 075005.
- Stevens, R. J. A. M., D. Lohse, and R. Verzicco, 2011, “Prandtl and Rayleigh number dependence of heat transport in high Rayleigh number thermal convection,” *J. Fluid Mech.* **688**, 31–43.
- Stevens, R. J. A. M., D. Lohse, and R. Verzicco, 2014, “Sidewall effects in Rayleigh-Bénard convection,” *J. Fluid Mech.* **741**, 1–27.
- Stevens, R. J. A. M., D. Lohse, and R. Verzicco, 2020, in *Direct and Large Eddy Simulation XII* ERCOFTAC Series Vol. 27, edited by M. García-Villalba, H. Kuerten, and M. V. Salvetti (Springer, New York), p. 215.
- Stevens, R. J. A. M., J. Overkamp, D. Lohse, and H. J. H. Clercx, 2011, “Effect of aspect-ratio on vortex distribution and heat transfer in rotating Rayleigh-Bénard convection,” *Phys. Rev. E* **84**, 056313.
- Stevens, R. J. A. M., E. P. van der Poel, S. Grossmann, and D. Lohse, 2013, “The unifying theory of scaling in thermal convection: The updated prefactors,” *J. Fluid Mech.* **730**, 295–308.
- Stevens, R. J. A. M., R. Verzicco, and D. Lohse, 2010, “Radial boundary layer structure and Nusselt number in turbulent Rayleigh-Bénard convection,” *J. Fluid Mech.* **643**, 495–507.
- Stevens, R. J. A. M., Q. Zhou, S. Grossmann, R. Verzicco, K.-Q. Xia, and D. Lohse, 2012, “Thermal boundary layer profiles in turbulent Rayleigh-Bénard convection in a cylindrical sample,” *Phys. Rev. E* **85**, 027301.
- Stewartson, K., 1966, in *Non-Equilibrium Thermodynamics, Variational Techniques and Stability*, edited by R. J. Donnelly, R. Herman, and Ilya Prigogine (University of Chicago Press, Chicago), pp. 158–162.
- Stringano, G., G. Pascazio, and R. Verzicco, 2006, “Turbulent thermal convection over grooved plates,” *J. Fluid Mech.* **557**, 307–336.
- Strogatz, S. H., 1994, *Nonlinear Dynamics and Chaos* (Perseus Press, Reading, MA).
- Sugiyama, K., E. Calzavarini, S. Grossmann, and D. Lohse, 2009, “Flow organization in two-dimensional non-Oberbeck-Boussinesq Rayleigh-Bénard convection in water,” *J. Fluid Mech.* **637**, 105–135.

- Sun, C., L.-Y. Ren, H. Song, and K.-Q. Xia, 2005, “Heat transport by turbulent Rayleigh-Bénard convection in 1 m diameter cylindrical cells of widely varying aspect ratio,” *J. Fluid Mech.* **542**, 165–174.
- Sun, C., and K.-Q. Xia, 2005, “Scaling of the Reynolds number in turbulent thermal convection,” *Phys. Rev. E* **72**, 067302.
- Tai, N. C., E. S. C. Ching, L. Zwirner, and O. Shishkina, 2021, “Heat flux in turbulent Rayleigh-Bénard convection: Predictions derived from a boundary layer theory,” *Phys. Rev. Fluids* **6**, 033501.
- Takeshita, T., T. Segawa, J. A. Glazier, and M. Sano, 1996, “Thermal Turbulence in Mercury,” *Phys. Rev. Lett.* **76**, 1465–1468.
- Teimurazov, A., M. McCormack, M. Linkmann, and O. Shishkina, 2024, “Unifying heat transport model for the transition between buoyancy-dominated and Lorentz-forcedominated regimes in quasi-static magnetoconvection,” *J. Fluid Mech.* **980**, R3.
- Teimurazov, A., S. Singh, S. Su, S. Eckert, O. Shishkina, and T. Vogt, 2023, “Oscillatory large-scale circulation in liquidmetal thermal convection and its structural unit,” *J. Fluid Mech.* **977**, A16.
- Threlfall, D. C., 1975, “Free convection in low-temperature gaseous helium,” *J. Fluid Mech.* **67**, 17–28.
- Tisserand, J. C., M. Creysseis, Y. Gasteuil, H. Pabiau, M. Gibert, B. Castaing, and F. Chillà, 2011, “Comparison between rough and smooth plates within the same Rayleigh-Bénard cell,” *Phys. Fluids* **23**, 015105.
- Tobasco, I., and C. R. Doering, 2017, “Optimal Wall-to-Wall Transport by Incompressible Flows,” *Phys. Rev. Lett.* **118**, 264502.
- Tollmien, W., 1929, “Über die Entstehung der Turbulenz. I. Mitteilung [On the origin of turbulence. First communication],” *Nachr. Ges. Wiss. Goettingen, Math.-Phys. Kl.* 21–44.
- Toppaladoddi, S., S. Succi, and J. S. Wettlaufer, 2017, “Roughness as a Route to the Ultimate Regime of Thermal Convection,” *Phys. Rev. Lett.* **118**, 074503.
- Trefethen, L. N., A. E. Trefethen, S. C. Reddy, and T. A. Driscoll, 1993, “Hydrodynamic stability without eigenvalues,” *Science* **261**, 578–584.
- Urban, P., P. Hanzelka, T. Králík, M. Macek, V. Musilová, and L. Skrbek, 2019, “Elusive transition to the ultimate regime of turbulent Rayleigh-Bénard convection,” *Phys. Rev. E* **99**, 011101.
- Urban, P., P. Hanzelka, T. Králík, V. Musilová, L. Skrbek, and A. Srnka, 2010, “Helium cryostat for experimental study of natural turbulent convection,” *Rev. Sci. Instrum.* **81**, 085103.
- Urban, P., P. Hanzelka, T. Králík, V. Musilová, A. Srnka, and L. Skrbek, 2012, “Effect of Boundary Layers Asymmetry on Heat Transfer Efficiency in Turbulent Rayleigh-Bénard Convection at Very High Rayleigh Numbers,” *Phys. Rev. Lett.* **109**, 154301.
- Urban, P., P. Hanzelka, T. Králík, V. Musilová, A. Srnka, and L. Skrbek, 2013, “Urban *et al.* Reply:,” *Phys. Rev. Lett.* **110**, 199402.
- Urban, P., P. Hanzelka, V. Musilová, T. Králík, M. L. Mantia, A. Srnka, and L. Skrbek, 2014, “Effect of boundary layers asymmetry on heat transfer efficiency in turbulent Rayleigh-Bénard convection at very high Rayleigh numbers,” *New J. Phys.* **16**, 053042.
- Urban, P., V. Musilová, and L. Skrbek, 2011, “Efficiency of Heat Transfer in Turbulent Rayleigh-Bénard Convection,” *Phys. Rev. Lett.* **107**, 014302.
- Vallis, G. K., 2017, *Atmospheric and Oceanic Fluid Dynamics* (Cambridge University Press, Cambridge, England).
- van der Poel, E. P., R. J. A. M. Stevens, and D. Lohse, 2013, “Comparison between two- and three-dimensional Rayleigh-Bénard convection,” *J. Fluid Mech.* **736**, 177–194.
- van der Poel, E. P., R. Ostilla-Mónico, J. Donners, and R. Verzicco, 2015, “A pencil distributed finite difference code for strongly turbulent wall-bounded flows,” *Comput. Fluids* **116**, 10–16.
- van Gils, D. P. M., G. W. Bruggert, D. P. Lathrop, C. Sun, and D. Lohse, 2011, “The Twente turbulent Taylor-Couette (T³C) facility: Strongly turbulent (multiphase) flow between two independently rotating cylinders,” *Rev. Sci. Instrum.* **82**, 025105.
- van Gils, D. P. M., S. G. Huisman, G.-W. Bruggert, C. Sun, and D. Lohse, 2011, “Torque Scaling in Turbulent Taylor-Couette Flow with Co- and Counterrotating Cylinders,” *Phys. Rev. Lett.* **106**, 024502.
- van Gils, D. P. M., S. G. Huisman, S. Grossmann, C. Sun, and D. Lohse, 2012, “Optimal Taylor-Couette turbulence,” *J. Fluid Mech.* **706**, 118–149.
- van Reeuwijk, M., H. Jonker, and K. Hanjalić, 2008, “Wind and boundary layers in Rayleigh-Bénard convection. II. Boundary layer character and scaling,” *Phys. Rev. E* **77**, 036312.
- Veronis, G., 1962, “The magnitude of the dissipation terms in the Boussinesq approximation,” *Astrophys. J.* **135**, 655–656.
- Verzicco, R., 2002, “Sidewall finite-conductivity effects in confined turbulent thermal convection,” *J. Fluid Mech.* **473**, 201–210.
- Verzicco, R., 2004, “Effect of non-perfect thermal sources in turbulent thermal convection,” *Phys. Fluids* **16**, 1965–1979.
- Verzicco, R., and R. Camussi, 1999, “Prandtl number effects in convective turbulence,” *J. Fluid Mech.* **383**, 55–73.
- Verzicco, R., and R. Camussi, 2003, “Numerical experiments on strongly turbulent thermal convection in a slender cylindrical cell,” *J. Fluid Mech.* **477**, 19–49.
- Verzicco, R., and P. Orlandi, 1996, “A finite-difference scheme for three-dimensional incompressible flow in cylindrical coordinates,” *J. Comput. Phys.* **123**, 402–413.
- Verzicco, R., and K. R. Sreenivasan, 2008, “A comparison of turbulent thermal convection between conditions of constant temperature and constant heat flux,” *J. Fluid Mech.* **595**, 203–219.
- Villermaux, E., 1995, “Memory-Induced Low Frequency Oscillations in Closed Convection Boxes,” *Phys. Rev. Lett.* **75**, 4618–4621.
- Villermaux, E., 1998, “Transfer at Rough Sheared Interfaces,” *Phys. Rev. Lett.* **81**, 4859–4862.
- von Kármán, T., 1923, “Gastheoretische Deutung der Reynoldsschen Kennzahl [Gas-theoretical interpretation of the Reynolds number],” *Z. Angew. Math. Mech.* **3**, 395.
- Wagner, S., and O. Shishkina, 2015, “Heat flux enhancement by regular surface roughness in turbulent thermal convection,” *J. Fluid Mech.* **763**, 109–135.
- Wagner, S., O. Shishkina, and C. Wagner, 2012, “Boundary layers and wind in cylindrical Rayleigh-Bénard cells,” *J. Fluid Mech.* **697**, 336–366.
- Wan, Z., P. Wei, R. Verzicco, D. Lohse, G. Ahlers, and R. J. A. M. Stevens, 2019, “Effect of sidewall on heat transfer and flow structure in Rayleigh-Bénard convection,” *J. Fluid Mech.* **881**, 218–243.
- Wang, D., H. Jiang, S. Liu, X. Zhu, and C. Sun, 2022, “Effects of radius ratio on annular centrifugal Rayleigh-Bénard convection,” *J. Fluid Mech.* **930**, A19.
- Wang, D., J. Liu, Q. Zhou, and C. Sun, 2023, “Statistics of temperature and velocity fluctuations in supergravitational convective turbulence,” *Acta Mech. Sin.* **39**, 122387.
- Wang, Q., D. Goluskin, and D. Lohse, 2023, “Lifetimes of metastable windy states in two-dimensional Rayleigh-Bénard convection with stress-free boundaries,” *J. Fluid Mech.* **976**, R2.

- Wang, Q., H. Liu, R. Verzicco, O. Shishkina, and D. Lohse, 2021, “Regime transitions in thermally driven high-Rayleigh number vertical convection,” *J. Fluid Mech.* **917**, A6.
- Wang, Q., D. Lohse, and O. Shishkina, 2021, “Scaling in internally heated convection: A unifying theory,” *Geophys. Res. Lett.* **48**, e2020GL091198.
- Wang, Q., R. Verzicco, D. Lohse, and O. Shishkina, 2020, “Multiple States in Turbulent Large-Aspect Ratio Thermal Convection: What Determines the Number of Convection Rolls?,” *Phys. Rev. Lett.* **125**, 074501.
- Wang, X., 2004, “Infinite Prandtl number limit of Rayleigh-Bénard convection,” *Commun. Pure Appl. Math.* **57**, 1265–1282.
- Wang, X., 2007, “Asymptotic behavior of the global attractors to the Boussinesq system for Rayleigh-Bénard convection at large Prandtl number,” *Commun. Pure Appl. Math.* **60**, 1293–1318.
- Wang, X., 2008, “Bound on vertical heat transport at large Prandtl number,” *Physica (Amsterdam)* **237D**, 854–858.
- Wedi, M., D. P. van Gils, S. Weiss, and E. Bodenschatz, 2021, “Rotating turbulent thermal convection at very large Rayleigh numbers,” *J. Fluid Mech.* **912**, A30.
- Wei, P., and G. Ahlers, 2014, “Logarithmic temperature profiles in the bulk of turbulent Rayleigh-Bénard convection for a Prandtl number of 12.3,” *J. Fluid Mech.* **758**, 809–830.
- Weiss, S., and G. Ahlers, 2011, “Turbulent Rayleigh-Bénard convection in a cylindrical container with aspect ratio $\Gamma = 0.50$ and Prandtl number $Pr = 4.38$,” *J. Fluid Mech.* **676**, 5–40.
- Weiss, S., and G. Ahlers, 2013, “Effect of tilting on turbulent convection: cylindrical samples with aspect ratio $\Gamma = 0.50$,” *J. Fluid Mech.* **715**, 314–334.
- Weiss, S., M. S. Emran, and O. Shishkina, 2024, “What Rayleigh numbers are achievable under Oberbeck-Boussinesq conditions?,” *J. Fluid Mech.* **986**, R2.
- Weiss, S., X. He, G. Ahlers, E. Bodenschatz, and O. Shishkina, 2018, “Bulk temperature and heat transport in turbulent Rayleigh-Bénard convection of fluids with temperature-dependent properties,” *J. Fluid Mech.* **851**, 374–390.
- Weiss, S., P. Wei, and G. Ahlers, 2016, “Heat-transport enhancement in rotating turbulent Rayleigh-Bénard convection,” *Phys. Rev. E* **93**, 043102.
- Werne, J., E. E. DeLuca, R. Rosner, and F. Cattaneo, 1991, “Development of Hard-Turbulent Convection in Two Dimensions: Numerical Evidence,” *Phys. Rev. Lett.* **67**, 3519.
- Whitehead, J. P., and C. R. Doering, 2011, “Ultimate State of Two-Dimensional Rayleigh-Bénard Convection between Free-Slip Fixed-Temperature Boundaries,” *Phys. Rev. Lett.* **106**, 244501.
- Wittenberg, R. W., 2010, “Bounds on Rayleigh-Bénard convection with imperfectly conducting plates,” *J. Fluid Mech.* **665**, 158–198.
- Wu, X., 2019, “Nonlinear theories for shear flow instabilities: Physical insights and practical implications,” *Annu. Rev. Fluid Mech.* **51**, 451–485.
- Wu, X. Z., and A. Libchaber, 1991, “Non-Boussinesq effects in free thermal convection,” *Phys. Rev. A* **43**, 2833–2839.
- Wu, X. Z., and A. Libchaber, 1992, “Scaling relations in thermal turbulence: The aspect-ratio dependence,” *Phys. Rev. A* **45**, 842–845.
- Wu, X.-Z., L. Kadanoff, A. Libchaber, and M. Sano, 1990, “Frequency Power Spectrum of Temperature Fluctuations in Free Convection,” *Phys. Rev. Lett.* **64**, 2140–2143.
- Xi, H.-D., and K.-Q. Xia, 2007, “Cessations and reversals of the large-scale circulation in turbulent thermal convection,” *Phys. Rev. E* **75**, 066307.
- Xi, H.-D., Q. Zhou, and K.-Q. Xia, 2006, “Azimuthal motion of the mean wind in turbulent thermal convection,” *Phys. Rev. E* **73**, 056312.
- Xia, K.-Q., 2013, “Current trends and future directions in turbulent thermal convection,” *Theor. Appl. Mech. Lett.* **3**, 052001.
- Xia, K.-Q., S. Lam, and S. Q. Zhou, 2002, “Heat-Flux Measurement in High-Prandtl-Number Turbulent Rayleigh-Bénard Convection,” *Phys. Rev. Lett.* **88**, 064501.
- Xie, Y.-C., and K.-Q. Xia, 2017, “Turbulent thermal convection over rough plates with varying roughness geometries,” *J. Fluid Mech.* **825**, 573–599.
- Xu, B.-L., Q. Wang, Z.-H. Wan, R. Yan, and D.-J. Sun, 2018, “Heat transport enhancement and scaling law transition in two-dimensional Rayleigh-Bénard convection with rectangular-type roughness,” *Int. J. Heat Mass Transfer* **121**, 872–883.
- Yik, H., V. Valori, and S. Weiss, 2020, “Turbulent Rayleigh-Bénard convection under strong non-Oberbeck-Boussinesq conditions,” *Phys. Rev. Fluids* **5**, 103502.
- Zhang, L., and K.-Q. Xia, 2023, “Heat transfer in a quasi-one-dimensional Rayleigh-Bénard convection cell,” *J. Fluid Mech.* **973**, R5.
- Zhang, X., R. E. Ecke, and O. Shishkina, 2021, “Boundary zonal flows in rapidly rotating turbulent thermal convection,” *J. Fluid Mech.* **915**, A62.
- Zhang, X., D. P. M. van Gils, S. Horn, M. Wedi, L. Zwirner, G. Ahlers, R. E. Ecke, S. Weiss, E. Bodenschatz, and O. Shishkina, 2020, “Boundary Zonal Flow in Rotating Turbulent Rayleigh-Bénard Convection,” *Phys. Rev. Lett.* **124**, 084505.
- Zhang, Y.-Z., C. Sun, Y. Bao, and Q. Zhou, 2018, “How surface roughness reduces heat transport for small roughness heights in turbulent Rayleigh-Bénard convection,” *J. Fluid Mech.* **836**, R2.
- Zhong, J., D. Wang, and C. Sun, 2023, “From sheared annular centrifugal Rayleigh-Bénard convection to radially heated Taylor-Couette flow: Exploring the impact of buoyancy and shear on heat transfer and flow structure,” *J. Fluid Mech.* **972**, A29.
- Zhong, J.-Q., and G. Ahlers, 2010, “Heat transport and the large-scale circulation in rotating turbulent Rayleigh-Bénard convection,” *J. Fluid Mech.* **665**, 300–333.
- Zhou, Q., R. J. A. M. Stevens, K. Sugiyama, S. Grossmann, D. Lohse, and K.-Q. Xia, 2010, “Prandtl-Blasius temperature and velocity boundary-layer profiles in turbulent Rayleigh-Bénard convection,” *J. Fluid Mech.* **664**, 297–312.
- Zhou, Q., K. Sugiyama, R. J. A. M. Stevens, S. Grossmann, D. Lohse, and K.-Q. Xia, 2011, “Horizontal structures of velocity and temperature boundary-layers in twodimensional numerical turbulent Rayleigh-Bénard convection,” *Phys. Fluids* **23**, 125104.
- Zhou, Q., and K.-Q. Xia, 2010, “Measured Instantaneous Viscous Boundary Layer in Turbulent Rayleigh-Bénard Convection,” *Phys. Rev. Lett.* **104**, 104301.
- Zhu, X., V. Mathai, R. J. A. M. Stevens, R. Verzicco, and D. Lohse, 2018, “Transition to the Ultimate Regime in Two-Dimensional Rayleigh-Bénard Convection,” *Phys. Rev. Lett.* **120**, 144502.
- Zhu, X., V. Mathai, R. J. A. M. Stevens, R. Verzicco, and D. Lohse, 2019, “Zhu *et al.* Reply:,” *Phys. Rev. Lett.* **123**, 259402.
- Zhu, X., R. J. A. M. Stevens, O. Shishkina, R. Verzicco, and D. Lohse, 2019, “ $Nu \sim Ra^{1/2}$ scaling enabled by multiscale wall roughness in Rayleigh-Bénard turbulence,” *J. Fluid Mech.* **869**, R4.
- Zhu, X., R. Stevens, R. Verzicco, and D. Lohse, 2017, “Roughness-Facilitated Local 1/2 Scaling Does Not Imply the Onset of the

- Ultimate Regime of Thermal Convection,” *Phys. Rev. Lett.* **119**, 154501.
- Zhu, X., R. A. Verschoof, D. Bakhuis, S. G. Huisman, R. Verzicco, C. Sun, and D. Lohse, 2018, “Wall roughness induces asymptotic ultimate turbulence,” *Nat. Phys.* **14**, 417–423.
- Zwirner, L., M. Emran, F. Schindler, S. Singh, S. Eckert, T. Vogt, and O. Shishkina, 2022, “Dynamics and length scales in vertical convection of liquid metals,” *J. Fluid Mech.* **932**, A9.
- Zwirner, L., R. Khalilov, I. Kolesnichenko, A. Mamykin, S. Mandrykin, A. Pavlinov, A. Shestakov, A. Teimurazov, P. Frick, and O. Shishkina, 2020, “The influence of the cell inclination on the heat transport and large-scale circulation in liquid metal convection,” *J. Fluid Mech.* **884**, A18.
- Zwirner, L., and O. Shishkina, 2018, “Confined inclined thermal convection in low-Prandtl-number fluids,” *J. Fluid Mech.* **850**, 984–1008.
- Zwirner, L., A. Tilgner, and O. Shishkina, 2020, “Elliptical Instability and Multiple-Roll Flow Modes of the Large-Scale Circulation in Confined Turbulent Rayleigh-Bénard Convection,” *Phys. Rev. Lett.* **125**, 054502.